A

Computational Study of Vortex Dynamics in Type-II Superconductors Using Time-Dependent Ginzburg-Landau Equations

by

Yuri V. Artemov

A dissertation submitted to the Graduate Faculty in Physics in
partial fulfillment of the requirements for the degree of Doctor of
Philosophy, The City University of New York

2005

UMI Number: 3159194

ProQuest Information and Learning Company
300 North Zeeb Road
P.O. Box 1346
Ann Arbor, MI 48106-1346

This manuscript has been read and accepted for the Graduate Faculty in Physics in satisfaction of the dissertation requirement for the degree of Doctor of Philosophy.

Brian Schwartz

January 26, 2005 Brian Schwartz, The Graduate Center

Date Chair of Examining Committee

Sultan Catto

January 26, 2005 Sultan Catto, Physics Executive officer

Date Executive Officer

Joseph Birman, City College

Fred Cadieu, Queens College

Fred Pollak, Brooklyn College

Fred Smith, City College

Supervisory Committee

THE CITY UNIVERSITY OF NEW YORK

Abstract

Computational Study Of Vortex Dynamics In Type-II Superconductors Using Time-Dependent Ginzburg-Landau Equations

by

Yuri V. Artemov

Adviser: Professor Brian B. Schwartz

This thesis is a compilation of numerical studies into the behavior of magnetic vortices in the type-II superconductors, both without defects and in the presence of defects. A highly effective numerical method of solution of the time-dependent Ginzburg-Landau equations is developed. The numerical solution of the TDGL equations reveals the behavior and structure of the vortex state in fine detail. The results of the computational models agree well with experiment. A wide range of phenomena is studied: the Meissner effect, the entrance of vortices in the bulk of the superconductor, the equilibrium Abrikosov lattice, hysteresis, surface barrier, vortex-antivortex annihilation and magnetic field reversal, the effects of transport current, interaction with various defects, both natural and artificial – twin boundaries, lattices of point and finite-size defects, as well as more exotic phenomena: symmetry breaking, dimensional phase transitions in thin films, and single vortex generators. The developed technique and code base allows for a thorough and accurate modeling of the real-world phenomena in type-II superconductors, as well as design of exotic pinning structures to achieve the desired material characteristics for practical development of high-field superconductors.

Acknowledgements

I wish to express my sincere gratitude to my mentor Dr. Brian Schwartz, who supervised my work on the thesis from the beginning to the end, inspired and supported my work in the field of scientific computation and visualization. I am grateful to the staff of the Graduate Center New Media Lab, of which Brian is co-director, where I have been working for three years writing code and developing 3D visualizations.

Many thanks to Dr. Don Middleton and his team from the National Center of Atmospheric Research (NCAR) in Boulder, CO. The skills I learned from him were instrumental in the design and implementation of Model5D, a software program developed for this thesis to help solve Ginzburg-Landau equations and to visualize the data.

The work with Dr. Ivan Schuller at the University of California in San Diego and many useful discussions with him and his group inspired me to do numerical research of the dimensional phase transition in thin films, the phenomenon he discovered experimentally.

CONTENTS

Chapter 3: Vortex Dynamics in 2D with No Defects 54

List of Figures

Chapter 1: Introduction

The discovery of superconductivity by Onnes in 1911 forever changed physics and the world as we know it. The property of some materials to completely lose their resistance to electric current below a critical temperature was quite unexpected and for almost 50 years remained unexplained. The resistance-free motion of current has a quality of perpetual motion. Superconducting materials have found many useful applications in basic and applied research, metrology and medicine, and many exciting applications in energy storage and distribution. The use of superconductors in transportation and communication are in the early stages of development.

In the 1950s-60s a remarkably complete theoretical picture of a classical superconducting material emerged. The Bardeen-Cooper-Schrieffer theory was developed in 1957 for the microscopic description of the behavior of electrons when attracted through the electron-phonon interactions, condense into Cooper pairs. The wave function for the pairs was equivalent to the order parameter in the earlier 1950 Ginzburg-Landau theory for a phenomenological description. The interest in superconductivity and its applications was given an impulse in 1986 when Bednorz and Müller discovered a new class of superconductors, with critical temperatures higher than the temperature of liquid nitrogen. The explanation of the phenomenon of superconductivity in these new cuprate materials is still far from a complete understanding.

This thesis presents calculations of numerical solution of the Ginzburg-Landau theory in order to achieve a better understanding of the interaction and response of type-II superconductors in a magnetic field in terms of quantized flux vortices. The Ginzburg-Landau equations describe the state of a superconducting medium in terms of an order parameter and a vector potential. There are no assumptions about the number of vortices in the system or the vortex interaction laws. In this sense, the time-dependent Ginzburg-

Landau equations are more reliable than the equations of molecular dynamics, especially in cases where boundaries and nucleation processes are involved.

We begin with an overview of the basic phenomena in superconductors, and then proceed to a discussion of the Ginzburg-Landau theory and the derivation of the time-dependent Ginzburg-Landau equations, which form the basis for the computational model solutions presented in this thesis.

1.1 The Basic Phenomena of Superconductivity

The electrical resistance of a superconductor disappears completely below a critical temperature T_c, which is a characteristic of the material. Persistent current in a superconducting ring can flow without measurable decrease for periods at least 10^5 years! Perfect conductivity is the first and a most important property of superconductors, making them ideal for such applications in high-current lossless transmission lines and in the construction of compact high-field magnets.

The second and more remarkable property of superconductors is perfect diamagnetism (the Meissner effect). In addition to perfect conductivity, the superconductor completely excludes magnetic field from its interior, no matter whether the superconductor is first cooled below T_c and then introduced into magnetic field (which can be explained by perfect conductivity and Faraday's law) or the normal sample is cooled through T_c with the magnetic field already present (a manifestation of perfect diamagnetism). As a result of this reversable behavior, the laws of thermodynamics can be applied and various phenomenological theories of superconductivity were developed.

However, by increasing magnetic field on the superconductor one is able to destroy the superconductivity and the field enter the interior of the now normal sample. This defines a thermodynamic critical field H_c which is determined by equating the energy $H^2/8\pi$ per unit volume, associated with excluding the field from the interior against the magnetic pressure, with the so-called condensation energy, corresponding to the Helmholtz free energy difference between the normal and superconducting states in zero field:

$$\frac{H_c^2}{8\pi} = L_n(T) - L(T).$$

The temperature dependence of the critical field $H_c(T)$ is well approximated by a parabolic law

$$H_c(T) = H_c(0)\left[1 - \left(\frac{T}{T_c}\right)^2\right],$$

where $H_c(0)$ is a thermodynamic critical field at zero temperature.

This simple phase diagram (Figure 1a) is obeyed by so-called type-I superconductors, which are completely diamagnetic up until the critical field. A second class of superconductors, so-called type-II, also experience a normal and a Meissner phase, but they have a third phase (Figure 1b), the mixed or *vortex* state, in which the magnetic field penetrates the superconductor in the form of magnetic lines of quantized flux known as *vortices*, first described by Abrikosov. The details of a vortex in terms of its current, field and superconductor behavior is described in Section 1.2.3.

The vortex state in a type-II superconductor is characterized by two critical field strengths, H_{c1} and H_{c2} ($H_{c1} < H_c < H_{c2}$, where H_c is the thermodynamics critical field). Below H_{c1} the superconductor exhibits the full Meissner effect. Above H_{c1}, but still below H_{c2}, it is in the mixed state, in which there is partial penetration of magnetic field in terms of vortices. Finally, superconductivity vanishes altogether above H_{c2}.

The phase diagram for the newer high-T_c type-II superconductors (Figure 1c) is considerably more complicated than that of the conventional type-II superconductors. The complexity stems from the diverse behavior exhibited by the vortex phase. Depending on the temperature and externally applied field, the vortices will behave much like the ions on a lattice; they form a rigid, periodic lattice (the Abrikosov lattice) in some cases and a rigid amorphous glass-like state in another; sometimes the lattice will flow much as liquid as the field and/or temperature is increased, while it may undergo plastic motion if enough shear stress develops in neighboring regions. The vortices are three-dimensional elastic objects and may even become entangled with one another.

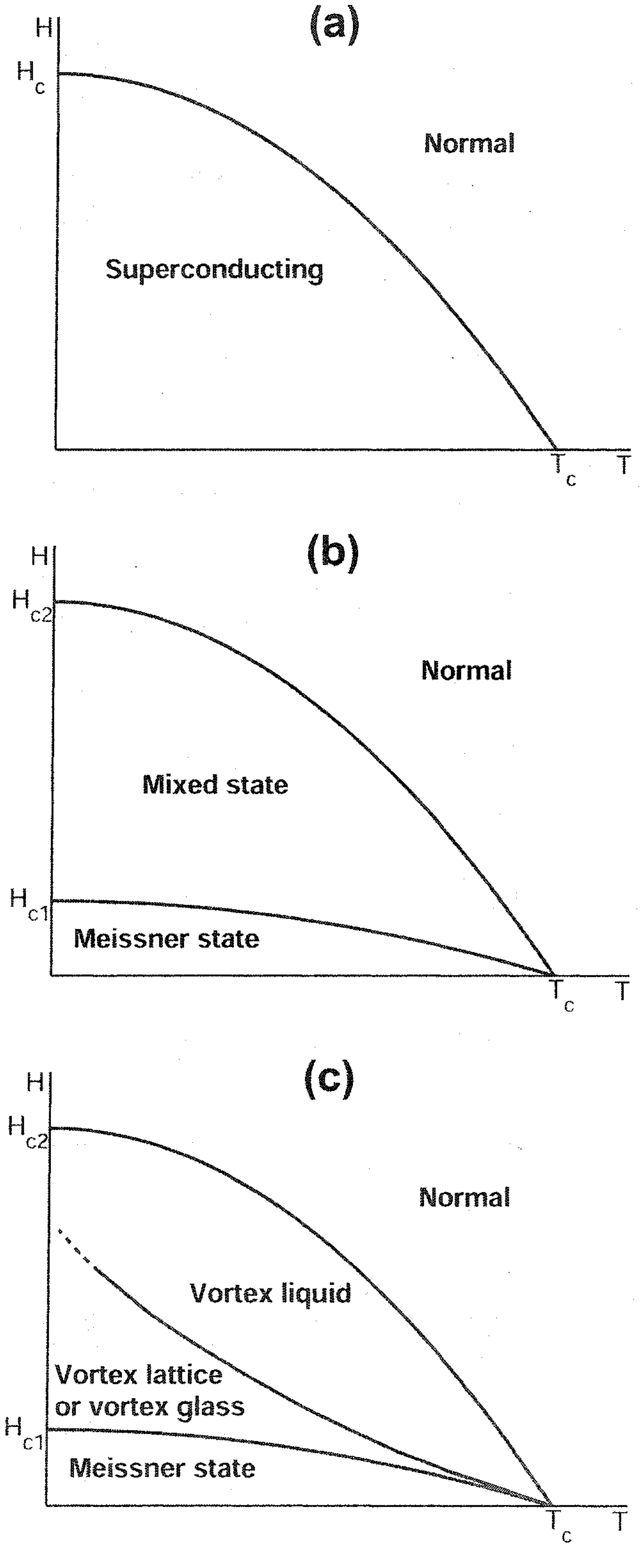

Figure 1. Phase diagram for a type-I (*a*), type-II (*b*), and high-T_c type-II (*c*) superconductor.

For more information on the various states attributed to the vortex phase of high-T_c materials, see a substantial review by G. Blatter et al. [1].

The construction of practical high-temperature superconducting devices-such as superconducting magnets and magnetic-energy storage devices necessitates high critical current densities. Due to the large amount of phase space occupied by the mixed state of type-II high-temperature superconductors, it is clear that within the superconducting material, vortex interactions and their motion are the primary influence on the current-carrying capabilities of these materials. It is the motion of these flux vortices that provides the primary dissipation mechanism which acts to limit critical current densities. Experimental evidence indicates that the ability of a high-T_c type-II superconducting material to conduct electricity without resistance, is essentially determined by the dynamics of the vortices as they are driven by external forces (currents) and move in the presence of material inhomogeneities (defects and impurities) and thermal fluctuations. These latter items provide pinning mechanisms which trap the vortices in position, thereby reducing vortex motion and resulting dissipation, and allows for increased critical current densities with essentially zero resistance.

A systematic examination of the interaction of vortices within these materials can determine possible designs of superconducting devices and can suggest better techniques for manufacturing processes of superconducting materials. In the research presented in this thesis, we determine design and processing data through direct numerical simulations of the time-dependent Ginzburg-Landau equations for model problems. The theory behind these equations is presented in the remainder of this chapter.

1.2 The Ginzburg-Landau Theory of Superconductivity

1.2.1 Ginzburg-Landau functional

The basic postulate of Ginzburg-Landau (GL) theory [3] is that the free energy density of the superconducting state can be written as a functional of a complex position dependent superconducting order parameter $\psi(\mathbf{r})$:

$$\boxed{L = L_n + a|\psi|^2 + \frac{b}{2}|\psi|^4 + \frac{1}{2m_s}\left|\left(\frac{\hbar}{i}\nabla - \frac{e_s}{c}\mathbf{A}\right)\psi\right|^2 + \frac{H^2}{8\pi}}, \tag{1.1}$$

where L_n is the free energy density of the normal phase in the absence of an external magnetic field, $e_s = -2e$ and m_s are the charge and effective mass associated with the Cooper pair, $\mathbf{A}$ is the vector potential, and $\mathbf{H} = \nabla \times \mathbf{A}$ is the magnetic field.

The quantities a and b are two phenomenological parameters; they are functions of external parameters, such as the temperature T, the concentration of impurities, etc. $b > 0$ for all T, and a changes sign at T_c ($a < 0$ for $T < T_c$, $a > 0$ for $T > T_c$). In the first approximation, a can be written as $a = \alpha(T - T_c)/T_c$, where α is a positive constant.

This functional first predicted by Ginzburg and Landau in 1950 has been derived from the microscopic BCS theory by Gorkov in 1959 [4].

The GL model takes its order parameter ψ to be the effective quantum mechanical wave function (hence complex valued) for the superconducting electrons: $n_s = |\psi|^2$.

The GL functional is the sum of three contributions: the condensation energy (terms with powers of ψ), the kinetic energy of the super-currents within the material, and the energy of the magnetic field. The behavior of the system is determined by finding the combination of ψ and $\mathbf{A}$ which minimizes L.

1.2.2 The Ginzburg-Landau equations

The minimization of the Ginzburg-Landau free-energy functional given in the previous section with respect to ψ and **A** (the explicit calculation is given in Appendix A) leads to the Ginzburg-Landau equations

$$\boxed{\frac{1}{2m_s}\left(\frac{\hbar}{i}\nabla-\frac{e_s}{c}\mathbf{A}\right)^2\psi+a\psi+b|\psi|^2\psi=0}, \tag{1.2}$$

$$\boxed{\frac{c}{4\pi}\nabla\times(\nabla\times\mathbf{A})+\frac{e_s^2}{m_s c}|\psi|^2\mathbf{A}+\frac{i\hbar e_s}{2m_s}\left(\psi^*\nabla\psi-\psi\nabla\psi^*\right)=0}. \tag{1.3}$$

The last two terms are the quantum mechanical expression for the current $\mathbf{J}_s$ of the charged particle; the first term is the magnetic flux. So this last expression is just the Maxwell equation relating the magnetic flux to the current:

$$\mathbf{J}_s\equiv\frac{c}{4\pi}\nabla\times\mathbf{B}=-\frac{i\hbar e_s}{2m_s}\left(\psi^*\nabla\psi-\psi\nabla\psi^*\right)-\frac{e_s^2}{m_s c}|\psi|^2\mathbf{A}. \tag{1.4}$$

1.2.3 Basic predictions of the Ginzburg-Landau theory

We begin with zero magnetic field and ignore spatial variations of the order parameter. For $T<T_c$ we find a minimum at

$$|\psi|^2=|\psi_\infty|^2\equiv\frac{|a|}{b}, \tag{1.5}$$

$$L_n-L=\frac{a^2}{2b},$$

so

$$H_c=2|a|\sqrt{\frac{\pi}{b}}. \tag{1.6}$$

The derivative of the free energy with respect to temperature is well behaved, and we have a continuous phase transition at T_c where $\psi(\mathbf{r})$ disappears.

Next consider a region still without fields but where ψ varies, such as along a normal-superconductor boundary. Specifically, let the right half-space $x \geq 0$ represent a superconductor below T_c. Then ψ will be real and given by the solution to the equation

$$\frac{\hbar^2}{2m_s}\frac{d^2\psi}{dx^2} + a\psi + b\psi^3 = 0 .$$

In the above equation we divide through by $a\psi_\infty$ and arrive at an equation in terms of a normalized function $f = \psi / \psi_\infty$

$$\xi^2 f'' + f - f^3 = 0 ,$$

where the primes denote differentiation and

$$\xi^2 = \frac{\hbar^2}{2m_s|a|} \propto \frac{1}{|1 - T/T_c|} . \tag{1.7}$$

The meaning of ξ is that it characterizes the spatial variations of ψ, i.e. it is a characteristic coherence length over which deviations in ψ fade out. To see this, note that $f = 1$ corresponds to the full SC state. Let $f(x) = 1 + g(x)$, with $|g(x)| << 1$, describe a small variation in f. The differential equation for f can be written in terms of the perturbation g, keeping only terms to first order, as

$$\xi^2 g'' + (1+g) - (1+3g+\ldots) = 0 ,$$

or

$$g'' = \frac{2}{\xi^2} g ,$$

which has a solution which decays exponentially with characteristic length ξ. Note that ξ diverges as $T \to T_c$. Hence fluctuations become significant in that limit and GL theory cannot be used.

Another characteristic length which is important in studying superconductors is the magnetic penetration length λ. This is the distance over which an applied field falls exponentially to zero upon encountering a superconducting region:

$$H(x) = H(0)e^{-x/\lambda}.$$

We can get a rough estimate of the value of λ by considering the superconductor to be in a very weak field such that ψ remains uniformly at the value ψ_∞. Then the expression for the supercurrent, Eq. (1.4), is given by

$$\mathbf{J} = -\frac{4e_s^2}{m_s c}\left|\psi_\infty\right|^2 \mathbf{A} = -\frac{4e_s^2}{m_s c}\frac{|a|}{b}\mathbf{A}, \tag{1.8}$$

which is of the London form $\mathbf{J} = -(c/4\pi)\mathbf{A}$. Therefore,

$$\lambda^2 = \frac{m_s c^2}{16\pi e_s^2}\frac{b}{|a|} \propto \frac{1}{\left|1 - T/T_c\right|}. \tag{1.9}$$

It has a similar temperature dependence as ξ and it, too, diverges in the limit $T \rightarrow T_C$. Thus as the temperature is increased, the field spreads into a larger area of the superconductor until the SC state is eventually destroyed.

The values of both ξ and λ help to determine the type category of a superconductor. Their ratio defines the temperature-independent Ginzburg-Landau parameter

$$\kappa = \frac{\lambda}{\xi}. \tag{1.10}$$

The GL theory was developed for the situation $\kappa << 1$ (so called type-I superconductors) which gave, correctly, a positive value of the surface energy between a normal and superconducting boundary.

Abrikosov [5] first demonstrated analytically that superconducting materials with $\kappa > 1/\sqrt{2}$ (type-II superconductors) allow for the penetration of magnetic fields in discrete units of flux – magnetic vortices. Each vortex has a total magnetic flux equal to the flux quantum

$$\Phi_0 = \frac{hc}{2e} \approx 2.07\times 10^{-7}\,\mathrm{G}\cdot\mathrm{cm}^2 \tag{1.11}$$

and a line energy ε_l, which approximately is (for $\kappa >> 1$)

$$\varepsilon_l \approx \varepsilon_0\left(\ln\kappa + \tfrac{1}{2}\right), \tag{1.12}$$

where we have introduced the energy per length

$$\varepsilon_0 = \left(\frac{\Phi_0}{4\pi\lambda}\right)^2. \tag{1.13}$$

This is the characteristic energy scale in vortex physics. The term ln κ originates from the supercurrents encircling the vortex, and the term ½ is the contribution from the suppression of the order parameter in the core of the vortex.

In Figure 2 we sketch the dependence of the order parameter ψ, magnetic field induction H, and current density J_s on the distance from the vortex center. At small distances $r \leq \xi$ (where ξ is the coherence length), the order parameter and current density increase linearly, while the magnetic field is almost constant. At large distances $r \geq \lambda$, the magnetic field and current density decrease exponentially, while the order parameter approaches its value ψ_∞ at infinity.

Combining Eqs. (1.6), (1.7) and (1.9), we obtain the following expression for the thermodynamic critical field

$$H_c = \frac{\Phi_0}{2\sqrt{2}\pi\lambda\xi}. \tag{1.14}$$

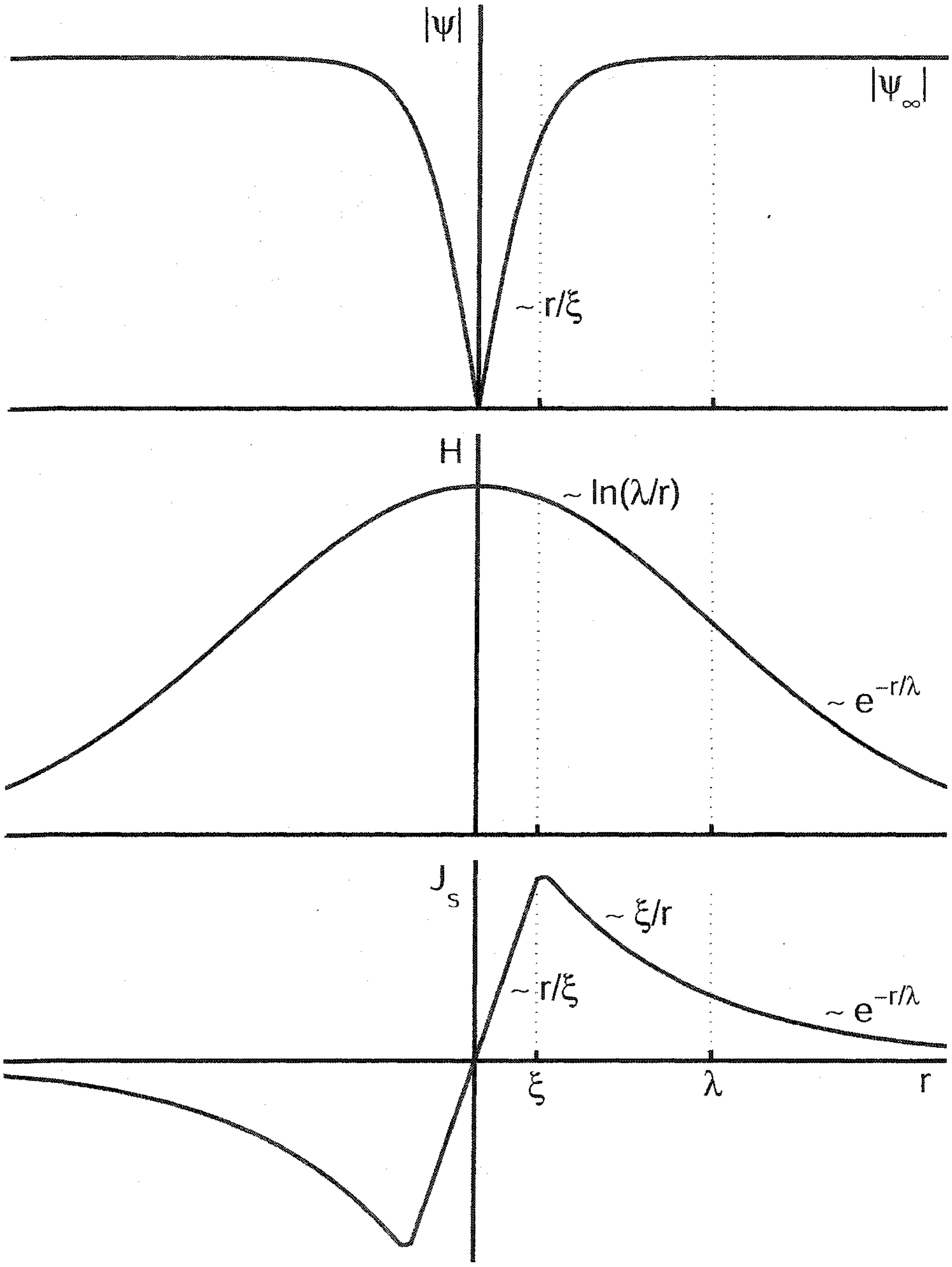

Figure 2. Structure of an isolated Abrikosov vortex.

The flux lines solution is energetically favorable when the external field reaches a value H_{c1} which is less than the thermodynamic critical field H_c. The reason is that the normal-SC surface energy for type-II materials is negative, so that an overall lowering of the energy occurs as more such surfaces are created. While it costs energy to create a vortex, there exists a field at which the surface energy gained overcomes the line energy of a vortex. Inserting the energy and flux of the vortex into the Gibbs energy, we obtain this *lower critical field*

$$H_{c1} = \frac{4\pi\varepsilon_l}{\Phi_0} = \frac{\Phi_0}{4\pi\lambda^2}, \tag{1.15}$$

defining the field at which vortices begin to enter the sample.

In equilibrium above H_{cl} these vortex lines form a hexagonal structure (vortex lattice) due to their mutual repulsion, which minimizes the free energy. For each applied field in the region between H_{cl} and H_{c2}, the solution is a balance among the vortex line energy, the negative surface energy, and the increase in energy due to the repulsive interactions between vortices. As the external field is raised, more vortices enter the superconductor until the field $H_{c2} > H_c$ is reached at which all superconductivity is destroyed. This H_{c2} is the point at which vortices are a approximately a coherence length ξ apart.

At high fields one uses the fact that the order parameter is small and the first GL-equation (1.2) can be linearized by dropping the $|\psi|^2\psi$ term. The resulting equation is identical to the Schrödinger equation for a charged particle with zero energy in an external magnetic field. Bound solutions only exist for a discrete set of magnetic fields, $H_n = \sqrt{2}\kappa H_c/(2n+1)$, and the largest of these fields defines the *upper critical field*

$$H_{c2} = \sqrt{2}\kappa H_c = \frac{\Phi_0}{2\pi\xi^2}. \tag{1.16}$$

Figure 3 gives a comparison of $B(H)$ curves for a type-I ($\kappa < 1/\sqrt{2}$) and type-II ($\kappa > 1/\sqrt{2}$) superconductor. Note that the transition to normal state is discontinuous (1st order phase transition) for a type-I superconductor, and continuous (2nd order phase transition) for a type-II superconductor.

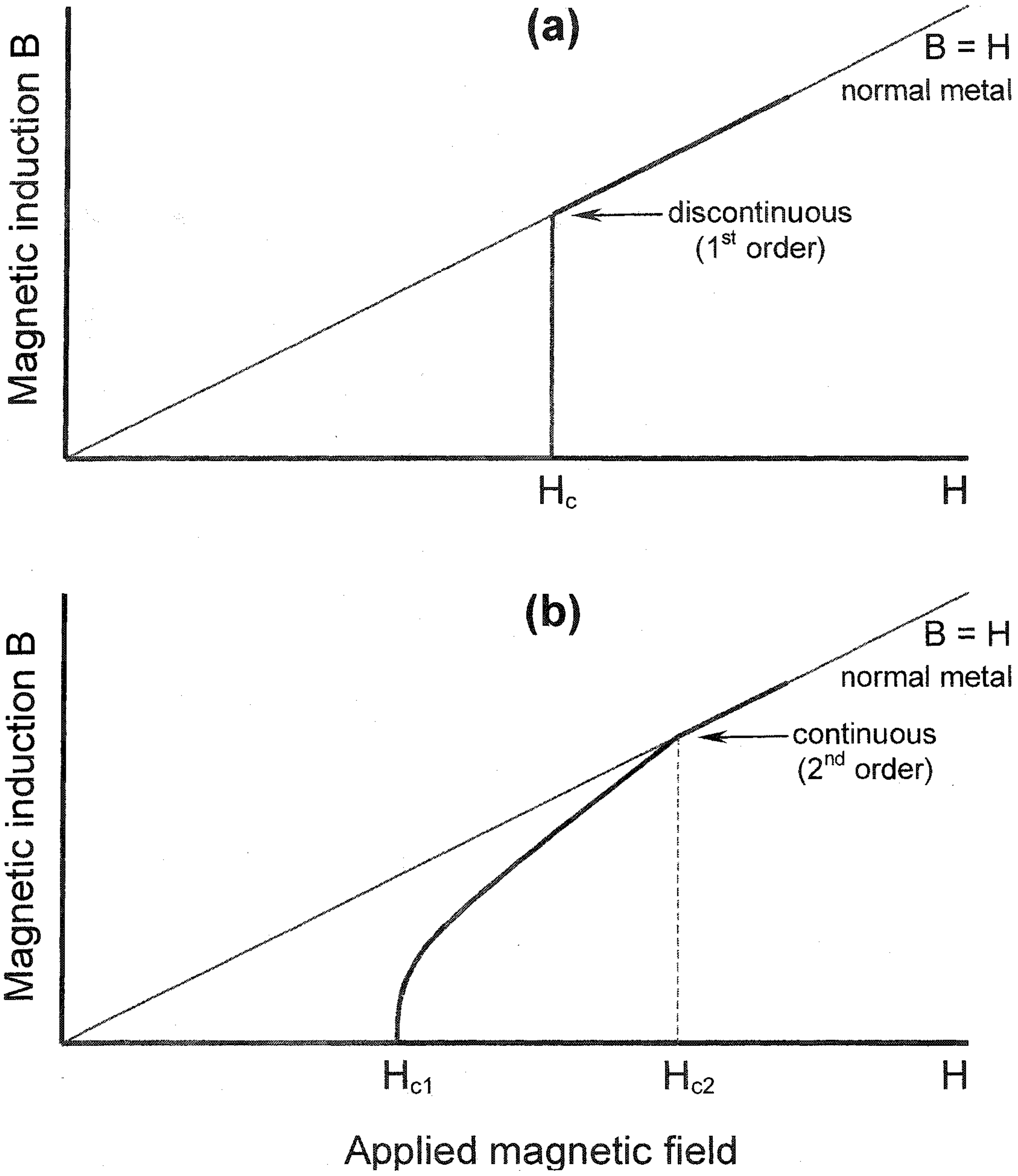

Figure 3. Magnetic field induction *B* vs. applied field *H* for a type-I (*a*) and type-II (*b*) superconductor.

1.3 The Time-Dependent Ginzburg-Landau Model

Many extensions of the GL theory to non-equilibrium situations exist in the literature. However, the most recent investigations into the dynamics of superconductors have dealt with the extreme type-II high-temperature superconductors where, strictly speaking, GL theory fails in the limit $T \to T_C$. Qualitative agreement with experimental observations is rather remarkable and so we expect that a set of time-dependent GL equations will give us similar qualitative insight into the dynamics of superconductors. Since we are after such a description one can put aside a rigorous derivation and postulates a time dependence based on thermodynamic reasoning.

It is assumed that a small fluctuation from equilibrium ψ will relax in a time τ. The simplest mechanism by which this may occur is via a diffusive process. Recall the standard heat flow equation [6]

$$C\frac{\partial T}{\partial t} = K\nabla^2 T + P\,,$$

where C is the specific heat and K is the thermal conductivity. In terms of the diffusivity $D = K/C$ this is

$$\frac{K}{D}\frac{\partial T}{\partial t} = K\nabla^2 T + P\,.$$

Hence, in analogy we write (1.2) as

$$\frac{\hbar^2}{2m_s D}\frac{\partial \psi}{\partial t} = -\left(\frac{1}{2m_s}\left(\frac{\hbar}{i}\nabla - \frac{e_s}{c}\mathbf{A}\right)^2 \psi + a\psi + b|\psi|^2\psi\right), \tag{1.17}$$

where D is a phenomenological diffusion coefficient; the minus sign on the right allows for a solution of the form $\exp(-t/\tau)$. A rigorous calculation gives

$$\tau = \frac{\hbar^2}{2m_s D|a|} = \frac{\hbar^2}{2m_s D\alpha}(1 - T/T_c)^{-1}. \tag{1.18}$$

Note that τ possesses the predicted divergence as $T \to T_c$.

Eq. (1.17) is not quite right. It is not invariant under a general gauge transform

$$\psi \to \psi e^{i\chi e_s/\hbar c},\ \mathbf{A} \to \mathbf{A} + \nabla\chi,\ \Phi \to \Phi - \frac{1}{c}\frac{\partial \chi}{\partial t}, \tag{1.19}$$

where Φ is the scalar electric potential. The correct gauge invariant formula is given as

$$\frac{\hbar^2}{2m_s D}\left(\frac{\partial}{\partial t} + i\frac{e_s}{\hbar}\Phi\right)\psi = -\frac{\delta L}{\delta \psi^*}, \tag{1.20}$$

where the right-hand side of (1.17) has been written in terms of the variational derivative.

The time dependence in the equation for the vector potential Eq. (1.3) is arrived at in a similar manner:

$$\frac{\sigma}{c}\left(\frac{1}{c}\frac{\partial \mathbf{A}}{\partial t} + \nabla\Phi\right) = -\frac{1}{2}\frac{\delta L}{\delta \mathbf{A}}. \tag{1.21}$$

1.3.1 The time-dependent Ginzburg-Landau equations

When the variational derivatives are written out, the time-dependent Ginzburg-Landau (TDGL) equations (1.20) and (1.21) take on the form

$$\boxed{\frac{\hbar^2}{2m_s D}\left(\frac{\partial}{\partial t} + i\frac{e_s}{\hbar}\Phi\right)\psi = -\left(\frac{1}{2m_s}\left(\frac{\hbar}{i}\nabla - \frac{e_s}{c}\mathbf{A}\right)^2 \psi + a\psi + b|\psi|^2\psi\right)}, \tag{1.22}$$

$$\boxed{\sigma\left(\frac{1}{c}\frac{\partial \mathbf{A}}{\partial t} + \nabla\Phi\right) = -\frac{c}{4\pi}\nabla\times(\nabla\times\mathbf{A}) - \frac{e_s^2}{m_s c}|\psi|^2\mathbf{A} - \frac{i\hbar e_s}{2m_s}\left(\psi^*\nabla\psi - \psi\nabla\psi^*\right)}. \tag{1.23}$$

The first of these equations has been derived by several authors [6], [8], [10]. The second equation is Ampere's law written out in terms of the vector and scalar potentials $\nabla \times \mathbf{B} = (4\pi/c)\mathbf{J}$.

Note that if **J** is viewed as the sum of a normal current (satisfying Ohm's law), and the supercurrent, then σ may be interpreted as the coefficient of normal conductivity. Thus $\mathbf{J} = \sigma\mathbf{E} + \mathbf{J}_s$, where $\mathbf{E} = -(1/c)\partial\mathbf{A}/\partial t - \nabla\Phi$ and $\mathbf{J}_s$ is the supercurrent density given by the time-independent equation,

$$\mathbf{J}_s = -\frac{i\hbar e_s}{2m_s c}\left(\psi^*\nabla\psi - \psi\nabla\psi^*\right) - \frac{e_s^2}{m_s c^2}|\psi|^2\mathbf{A}. \tag{1.24}$$

1.3.2 Boundary conditions

The configuration used for the simulations based on TDGL model is a superconducting core surrounded by a blanket of nonsuperconducting material (insulator or ordinary metal). Outside the superconductor, the order parameter is identically zero. No Cooper pair leaves the superconductor, so

$$\mathbf{J}_s \cdot \mathbf{n} = 0 \tag{1.25}$$

at the interface between the superconductor and the blanket, where **n** is the local unit normal vector. Strictly speaking, this condition is correct only for superconductor-insulator interfaces and needs to be generalized for superconductor-metal interfaces (see [11], Section 7-3). However, in this work we have used the condition (1.25) for the superconducting boundary.

On the outer surface, we may prescribe a surface current **K** to account for an applied magnetic field **H** in the exterior vacuum. The surface current causes a jump discontinuity in the tangential component of **B**, whose magnitude is $(4\pi/c)$ times the magnitude of **K** and whose direction is parallel to $\mathbf{K} \times \mathbf{n}$.

We use the gradient of magnetic field to create a transport current in the sample. We assume that the sample is infinite and periodic in the direction of the transport current, so that we always model a section of a current path, not a current loop. By specifying only the boundary fields, we put no restriction on the transport distribution in the sample.

1.3.3 Dimensionless form of the TDGL equations

In order to numerically solve the TDGL equations, a final step is to render them in dimensionless form.

We measure lengths in units of the London penetration depth λ (Eq. (1.9)); time in units of the relaxation time $\tau = \xi^2/D$, field in units of $H_c\sqrt{2}$ (Eq. (1.6)); and energy densities in units of $H_c^2/4\pi$. With $|\psi_\infty|^2 = |a|/b$, we have

$$\lambda = \left(\frac{m_s c^2}{4\pi |\psi_\infty|^2 e_s^2} \right)^{1/2}, \tag{1.26}$$

$$\xi = \left(\frac{\hbar^2}{2m_s |a|} \right)^{1/2}, \tag{1.27}$$

$$H_c = \left(4\pi |a| |\psi_\infty|^2 \right)^{1/2}. \tag{1.28}$$

We make the following substitutions:

$$\begin{aligned}
&\mathbf{r} \to \lambda \mathbf{r},\\
&t \to \tau t,\\
&\psi \to \psi_\infty \psi,\\
&\mathbf{A} \to \lambda H_c \sqrt{2}\mathbf{A},\\
&\Phi \to (\lambda/c\tau)\lambda H_c\sqrt{2}\Phi,\\
&L \to (H_c^2/4\pi)L,\\
&\mathbf{B} \to H_c\sqrt{2}\mathbf{B},\\
&\mathbf{E} \to (\lambda/c\tau)H_c\sqrt{2}\mathbf{E},\\
&\mathbf{J} \to (\psi_\infty^2 e_s\hbar/m_s\xi)\mathbf{J},\\
&\sigma \to (c^2\tau/4\pi\lambda^2)\sigma.
\end{aligned} \tag{1.29}$$

Here ψ, **A**, etc. are functions of **r** and t. Thus, we obtain the dimensionless form of the time-dependent Ginzburg-Landau equations:

$$\boxed{\left(\frac{\partial}{\partial t} + i\kappa\Phi\right)\psi = -\left(\frac{i}{\kappa}\nabla + \mathbf{A}\right)^2 \psi + \psi - |\psi|^2\psi}, \tag{1.30}$$

$$\boxed{\sigma\left(\frac{\partial \mathbf{A}}{\partial t} + \nabla\Phi\right) = -\nabla\times\nabla\times\mathbf{A} + \mathbf{J}_s}, \tag{1.31}$$

$$\boxed{\mathbf{J}_s = \frac{1}{2i\kappa}\left(\psi^*\nabla\psi - \psi\nabla\psi^*\right) - |\psi|^2\mathbf{A} = |\psi|^2\left(\frac{1}{\kappa}\nabla\phi - \mathbf{A}\right)}, \tag{1.32}$$

where ϕ is the phase of complex-valued order parameter $\psi = |\psi|e^{i\phi}$.

The constant κ is the Ginzburg-Landau parameter, $\kappa = \lambda/\xi$, where λ and ξ are given by Eqs. (1.9) and (1.7), respectively, and σ is a dimensionless normal conductivity parameter. The nondimensional TDGL equations are associated with the dimensionless energy functional

$$\boxed{L = -|\psi|^2 + \tfrac{1}{2}|\psi|^4 + \left|\left(\frac{i}{\kappa}\nabla - \mathbf{A}\right)\psi\right|^2 + |\nabla\times\mathbf{A}|^2}. \tag{1.33}$$

In the system of dimensionless variables, the thermodynamic, lower, and upper critical fields are, respectively,

$$H_c = \frac{1}{\sqrt{2}} \approx 0.707, \tag{1.34}$$

$$H_{c1} = \frac{\ln\kappa + \frac{1}{2}}{2\kappa}, \tag{1.35}$$

$$H_{c2} = \kappa. \tag{1.36}$$

The BCS depairing current is (see [12], Eq. 4.36)

$$J_{BCS} = \frac{2}{9}\sqrt{3} \approx 0.385. \tag{1.37}$$

1.3.4 Zero potential gauge

The TDGL model is invariant under the gauge transformation (in dimensionless variables)

$$\psi \to \psi e^{i\kappa\chi},\ \mathbf{A} \to \mathbf{A} + \nabla\chi,\ \Phi \to \Phi - \frac{\partial\chi}{\partial t}, \tag{1.38}$$

where the gauge χ is any function of space and time; see [13].

We choose the *zero-electric potential gauge*, so that $\Phi = 0$ at all times. Eqs. (1.30) and (1.31) are thus reduced to

$$\frac{\partial\psi}{\partial t} = -\left(\frac{i}{\kappa}\nabla + \mathbf{A}\right)^2 \psi + \psi - |\psi|^2 \psi, \tag{1.39}$$

$$\sigma\frac{\partial\mathbf{A}}{\partial t} = -\nabla\times\nabla\times\mathbf{A} + \mathbf{J}_s. \tag{1.40}$$

In variational form, we have

$$\frac{\partial\psi}{\partial t} = -\frac{\delta L}{\delta\psi^*}, \tag{1.41}$$

$$\sigma \frac{\partial \mathbf{A}}{\partial t} = -\frac{1}{2}\frac{\delta L}{\delta \mathbf{A}}. \tag{1.42}$$

1.3.5 Link variables

In order to further prepare TDGL equations for numerical solutions, we introduce the auxiliary link vector $\mathbf{U} = (U_x, U_y, U_z)$,

$$\mathbf{U} = e^{-i\kappa \int \mathbf{A} dr}. \tag{1.43}$$

This definition is axis dependent:

$$U_x = \exp\left(-i\kappa \int_{x_0}^{x} A_x(x', y, z)\, dx'\right), \tag{1.44}$$

and so forth (we omit the argument t). The point $\mathbf{r}_0 = (x_0, y_0, z_0)$ is an arbitrary reference point. Each U_μ ($\mu = x, y, z$) is complex valued and unimodular, $U_\mu^* = U_\mu^{-1}$.

The variables U_μ are related to the link variables of lattice gauge theory [5], [14]. Their introduction at this point facilitates the preservation of gauge invariance under discretization [6]. Borrowing the terminology, we refer to the vector $\mathbf{U}$ as the vector of *link variables*.

It follows from (1.44) that

$$A_\mu = -\frac{1}{2i\kappa}\left(U_\mu^* \frac{\partial U_\mu}{\partial \mu} - U_\mu \frac{\partial U_\mu^*}{\partial \mu}\right). \tag{1.45}$$

The energy density (1.33) can now be written in the form

$$L = -|\psi|^2 + \tfrac{1}{2}|\psi|^4 + \frac{1}{\kappa^2}\sum_{\mu=x,y,z}\left|\frac{\partial}{\partial \mu}(U_\mu \psi)\right|^2. \tag{1.46}$$

This expression shows that the presence of a nonzero field induces anisotropic diffusion of the order parameter. The diffusion coefficient depends locally on the link vector $\mathbf{U}$.

When the equations (1.41) and (1.42) are worked out, the differential equations to be solved are

$$\boxed{\frac{\partial \psi}{\partial t}=\frac{1}{\kappa^2}\sum_{\mu=x,y,z} U_\mu^* \frac{\partial^2}{\partial \mu^2}\left(U_\mu \psi\right)+\psi-|\psi|^2 \psi}, \tag{1.47}$$

$$\boxed{\sigma \frac{\partial \mathbf{A}}{\partial t}=-\nabla \times \nabla \times \mathbf{A}+\mathbf{J}_s}. \tag{1.48}$$

The supercurrent density $\mathbf{J}_s$ is given in terms of ψ and $\mathbf{A}$ by (1.32) or, alternatively, in terms of ψ and $\mathbf{U}$ by

$$\begin{aligned} J_{s,\mu} &= \frac{1}{2i\kappa}\left(U_\mu^* \psi^* \frac{\partial}{\partial \mu}\left(U_\mu \psi\right)-U_\mu \psi \frac{\partial}{\partial \mu}\left(U_\mu^* \psi^*\right)\right)= \\ &= \frac{1}{\kappa} \operatorname{Im}\left[\left(U_\mu \psi\right)^* \frac{\partial}{\partial \mu}\left(U_\mu \psi\right)\right], \quad \mu=x, y, z. \end{aligned} \tag{1.49}$$

The equation (1.47) must be solved subject to the boundary condition $\mathbf{J}_s \cdot \mathbf{n}=0$ (see Section 1.3.2). The TDGL model is completed by the specification of initial conditions for ψ and $\mathbf{B}$.

1.3.6 Material defects

The energy functional (1.46) assumes that there are no defects in the superconductor. Material defects can be naturally present or artificially induced and can be in the form of point, planar (twin boundaries), columnar (quenched disorder) or arbitrary geometry defects. A material defect weakens or eliminates the depression of the condensation energy. In the TDGL model, this depression is accomplished by replacing the term $-|\psi|^2$ in (1.46) and (1.47) by a term $-(1-\gamma)|\psi|^2$:

$$L=-(1-\gamma)|\psi|^2+\tfrac{1}{2}|\psi|^4+\frac{1}{\kappa^2}\sum_{\mu=x,y,z}\left|\frac{\partial}{\partial \mu}\left(U_\mu \psi\right)\right|^2, \tag{1.50}$$

$$\frac{\partial \psi}{\partial t} = \frac{1}{\kappa^2} \sum_{\mu = x,y,z} U_\mu^* \frac{\partial^2}{\partial \mu^2} \left(U_\mu \psi \right) + \psi - (1 - \gamma) |\psi|^2 \psi . \tag{1.51}$$

Parameter γ depends on position: $0 < \gamma(\mathbf{r}) \leq 1$ if $\mathbf{r}$ is in a defective region, $\gamma(\mathbf{r}) = 0$ otherwise.

In the next chapter, we focus on the computational aspects involved in solving the time-dependent Ginzburg-Landau equations for various conditions.

Chapter 2: Numerical Solutions of the TDGL Equations

In this chapter we present the final step needed for the solutions of the time-dependent Ginzburg-Landau equations. We transform the dimensionless TDGL equations (1.47)–(1.49) to discrete form, suitable for solutions using a computer, and implement the numerical solutions using an alternating-direction explicit method.

We perform the discretization in a 3D geometry, so that the formulas can easily be reduced to a 2D geometry by dropping the third dimension. For simplicity, the implementation, however, is discussed for 2D case only.

We consider rectangular configurations, where a brick-shaped region Ω_{sc} of superconducting material is imbedded in an insulator. The entire configuration has the shape of a rectangular box, which occupies a region Ω in space (Figure 4). The brick and the box are lined up in parallel. Outside Ω, the magnetic field is given and uniform.

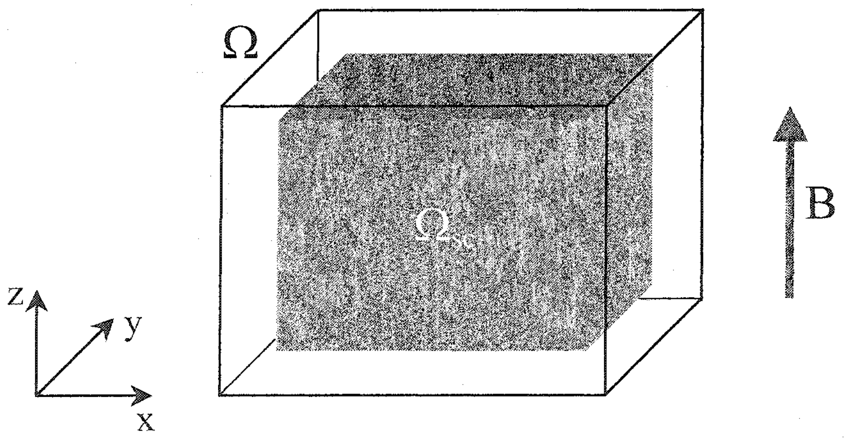

Figure 4. Superconducting region Ω_{sc} embedded in an insulating region Ω.

2.1 Discretization

2.1.1 Computational grid

All computations are done on a uniform grid with mesh widths h_x, h_y, and h_z. A typical grid cell is

$$\Omega_{i,j,k} = \{\mathbf{r} = (x,y,z) : x_i < x < x_{i+1},\ y_j < y < y_{j+1},\ z_k < z < z_{k+1}\}, \tag{2.1}$$

where

$$x_i = x_1 + (i-1)h_x,\ y_j = y_1 + (j-1)h_y,\ z_k = z_1 + (k-1)h_z .$$

The vertex $\mathbf{r}_{i,j,k} = (x_i, y_j, z_k)$ is the reference point for $\Omega_{i,j,k}$. Unless noted otherwise, the indices run through the values $i = 1,\ldots,n_x, j = 1,\ldots,n_y, k = 1,\ldots,n_z$.

Conceptually, the domain Ω lies inside the grid at a distance of one-half mesh width from the bounding faces in each coordinate direction,

$$\begin{aligned}\Omega = \{\mathbf{r} = (x,y,z) : {}& x_1 + \tfrac{1}{2}h_x < x < x_{n_x-1} + \tfrac{1}{2}h_x, \\ & y_1 + \tfrac{1}{2}h_y < y < y_{n_y-1} + \tfrac{1}{2}h_y,\ z_1 + \tfrac{1}{2}h_z < z < z_{n_z-1} + \tfrac{1}{2}h_z\}.\end{aligned} \tag{2.2}$$

The domain Ω_{sc} is located an integer number of mesh widths inside Ω, in such a way that there is always at least one layer of grid points between Ω_{sc} and Ω. That is,

$$\begin{aligned}\Omega_{\mathrm{sc}} = \{\mathbf{r} = (x,y,z) : {}& x_{n_{sx}} + \tfrac{1}{2}h_x < x < x_{n_{ex}-1} + \tfrac{1}{2}h_x, \\ & y_{n_{sy}} + \tfrac{1}{2}h_y < y < y_{n_{ey}-1} + \tfrac{1}{2}h_y,\ z_{n_{sz}} + \tfrac{1}{2}h_z < z < z_{n_{ez}-1} + \tfrac{1}{2}h_z\},\end{aligned} \tag{2.3}$$

for three pairs of integers (n_{sx}, n_{ex}), (n_{sy}, n_{ey}), and (n_{sz}, n_{ez}), which satisfy the inequalities $1 < n_{s\mu} < n_{e\mu} < n_\mu$ $(\mu = x, y, z)$. (The subscripts *sx*, *sy*, *sz* and *ex*, *ey*, *ez* stand for the "starting" and "ending" values in the *x*, *y*, *z* direction, respectively.)

We shall derive the discrete TDGL model from an approximation to the free-energy functional. The approximation is second-order accurate as the mesh width goes to zero, since all integrals are evaluated by means of the midpoint rule and derivatives approximated by central differences.

2.1.2 Discrete variables

We denote the discrete variables by the same symbols as their continuous counterparts. The index (i, j, k) is assigned to any quantity related to the grid cell $\Omega_{i,j,k}$. The primary variables are the order parameter and the vector of link variables; all other variables (vector potential, induced magnetic field, supercurrent) are expressed in terms of these primary variables. The primary variables are evaluated on staggered grids.

The order parameter ψ,

$$\psi = \left\{ \psi_{i,j,k} : i = n_{sx}, \ldots, n_{ex};\ j = n_{sy}, \ldots, n_{ey};\ k = n_{sz}, \ldots, n_{ez} \right\}, \tag{2.4}$$

where

$$\psi_{i,j,k} = \psi\left(x_i, y_j, z_k\right).$$

The vector of link variables $\mathbf{U} = (U_x, U_y, U_z)$,

$$U_x = \left\{ U_{x;i,j,k} : i, j, k \right\},\ U_y = \left\{ U_{y;i,j,k} : i, j, k \right\},\ U_z = \left\{ U_{z;i,j,k} : i, j, k \right\}, \tag{2.5}$$

where

$$U_{x;i,j,k} = \exp\left(-i\kappa \int_{x_i}^{x_{i+1}} A_x\left(\xi, y_j, z_k\right) d\xi \right), \tag{2.6}$$

$$U_{y;i,j,k} = \exp\left(-i\kappa \int_{y_j}^{y_{j+1}} A_y\left(x_i, \eta, z_k\right) d\eta \right), \tag{2.7}$$

$$U_{z;i,j,k} = \exp\left(-i\kappa \int_{z_k}^{z_{k+1}} A_z\left(x_i, y_j, \varsigma\right) d\varsigma \right). \tag{2.8}$$

The vector potential $\mathbf{A} = (A_x, A_y, A_z)$,

$$A_x = \left\{ A_{x;i,j,k} : i,j,k \right\},\ A_y = \left\{ A_{y;i,j,k} : i,j,k \right\},\ A_z = \left\{ A_{z;i,j,k} : i,j,k \right\}, \tag{2.9}$$

where

$$\begin{gathered} A_{x;i,j,k} = A_x\left(x_i + \tfrac{1}{2}h_x, y_j, z_k\right),\ A_{y;i,j,k} = A_y\left(x_i, y_j + \tfrac{1}{2}h_y, z_k\right), \\ A_{z;i,j,k} = A_z\left(x_i, y_j, z_k + \tfrac{1}{2}h_z\right). \end{gathered} \tag{2.10}$$

The magnetic field vector $\mathbf{B} = (B_x, B_y, B_z)$,

$$B_x = \left\{ B_{x;i,j,k} : i,j,k \right\},\ B_y = \left\{ B_{y;i,j,k} : i,j,k \right\},\ B_z = \left\{ B_{z;i,j,k} : i,j,k \right\}, \tag{2.11}$$

where

$$\begin{gathered} B_{x;i,j,k} = B_x\left(x_i, y_j + \tfrac{1}{2}h_y, z_k + \tfrac{1}{2}h_z\right),\ B_{y;i,j,k} = B_y\left(x_i + \tfrac{1}{2}h_x, y_j, z_k + \tfrac{1}{2}h_z\right), \\ B_{z;i,j,k} = B_z\left(x_i + \tfrac{1}{2}h_x, y_j + \tfrac{1}{2}h_y, z_k\right). \end{gathered} \tag{2.12}$$

The boundary conditions impose a constraint on the values of $B_{z;i,j,k}$ when either of the indices i and j is equal to its first or last value; see (2.41)–(2.46). Similarly for the other directions.

The supercurrent $\mathbf{J}_s = (J_{s,x}, J_{s,y}, J_{s,z})$,

$$J_{s,x} = \left\{ J_{s,x;i,j,k} : i = n_{sx},\ldots,n_{ex}-1;\ j = n_{sy},\ldots,n_{ey};\ k = n_{sz},\ldots,n_{ez} \right\}, \tag{2.13}$$

$$J_{s,y} = \left\{ J_{s,y;i,j,k} : i = n_{sx},\ldots,n_{ex};\ j = n_{sy},\ldots,n_{ey}-1;\ k = n_{sz},\ldots,n_{ez} \right\}, \tag{2.14}$$

$$J_{s,z} = \left\{ J_{s,z;i,j,k} : i = n_{sx},\ldots,n_{ex};\ j = n_{sy},\ldots,n_{ey};\ k = n_{sz},\ldots,n_{ez}-1 \right\}, \tag{2.15}$$

where

$$\begin{gathered} J_{s,x;i,j,k} = J_{s,x}\left(x_i + \tfrac{1}{2}h_x, y_j, z_k\right),\ J_{s,y;i,j,k} = J_{s,y}\left(x_i, y_j + \tfrac{1}{2}h_y, z_k\right), \\ J_{s,z;i,j,k} = J_{s,z}\left(x_i, y_j, z_k + \tfrac{1}{2}h_z\right). \end{gathered} \tag{2.16}$$

In Figure 5, we show a typical grid cell $\Omega_{i,j,k}$ in the interior of Ω_{sc} with the evaluation points for ψ and the components of $\mathbf{A}$, $\mathbf{J}_s$ and $\mathbf{B}$ in two and three dimensions.

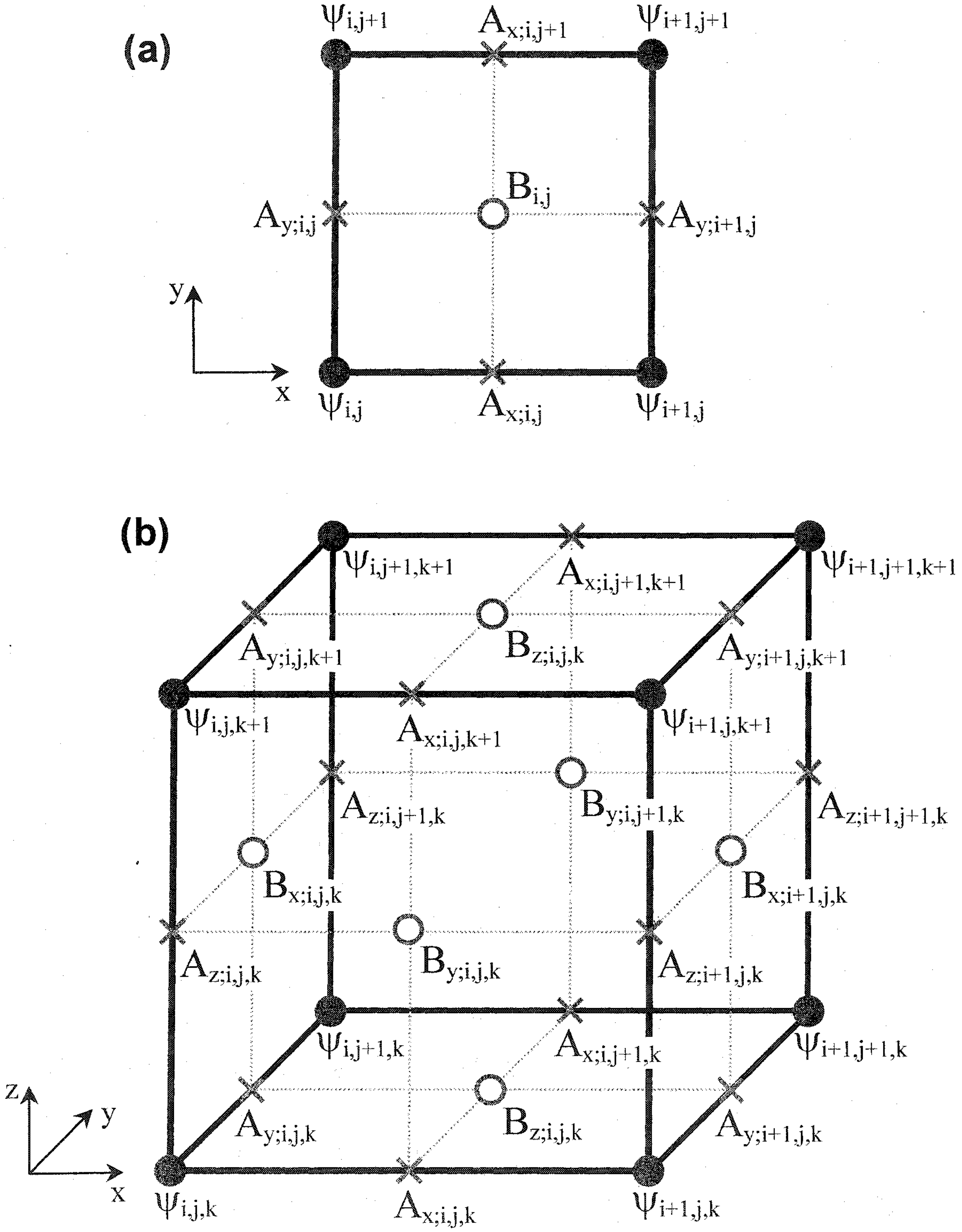

Figure 5. Evaluation points for ψ, **A**, and **B** in 2D (*a*) and 3D (*b*). Evaluation points for $\mathbf{J}_s$ coincide with the corresponding points for **A**.

Within the framework of a second-order accurate approximation, the definition (1.43) is equivalent with

$$U_{\mu;i,j,k}=\exp\left(-i\kappa h_{\mu}A_{\mu;i,j,k}\right),\ \mu=x,y,z\,. \tag{2.17}$$

The computation of the magnetic field is more complicated. We consider one component (B_z) in detail; the others are treated similarly.

Let D be any two-dimensional domain that is orthogonal to the z direction; let ∂D denote the (oriented) boundary of D, **t** the unit tangential vector along ∂D. According to Stokes's identity,

$$\exp\left(-i\kappa\iint_{D}B_{z}dxdy\right)=\exp\left(-i\kappa\oint_{\partial D}\mathbf{A}\cdot d\mathbf{t}\right). \tag{2.18}$$

Take $D=\{\mathbf{r}=(x,y,z)\in\Omega\colon x_i<x<x_{i+1},y_j<y<y_{j+1},z=z_k\}$. If we approximate the area integral in (2.18) by the midpoint rule and the resulting exponential by the first two terms of its Taylor expansion, we obtain the second-order accurate identity

$$\exp\left(-i\kappa\iint_{D}B_{z}dxdy\right)=1-i\kappa h_{x}h_{y}B_{z;i,j,k}\,. \tag{2.19}$$

The exponential of the contour integral in (2.18) is the product of four link variables (or their complex conjugates) associated with $\Omega_{i,j,k}$,

$$\exp\left(-i\kappa\oint_{\partial D}\mathbf{A}\cdot d\mathbf{t}\right)=U^{*}_{x;i,j+1,k}U^{*}_{y;i,j,k}U_{x;i,j,k}U_{y;i+1,j,k}\,. \tag{2.20}$$

Combining (2.18)–(2.20), we obtain $B_{z;i,j,k}$ in terms of the link variables,

$$B_{z;i,j,k}=\frac{1-U^{*}_{x;i,j+1,k}U^{*}_{y;i,j,k}U_{x;i,j,k}U_{y;i+1,j,k}}{i\kappa h_{x}h_{y}}\,. \tag{2.21}$$

In general, we have

$$B_{\mu;i,j,k}=h_{\mu}\frac{1-W_{\mu;i,j,k}}{i\kappa h_{x}h_{y}h_{z}},\ \mu=x,y,z\,, \tag{2.22}$$

where we have introduced the abbreviations

$$W_{x;i,j,k} = U^*_{y;i,j,k+1} U^*_{z;i,j,k} U_{y;i,j,k} U_{z;i,j+1,k}, \tag{2.23}$$

$$W_{y;i,j,k} = U^*_{z;i+1,j,k} U^*_{x;i,j,k} U_{z;i,j,k} U_{x;i,j,k+1}, \tag{2.24}$$

$$W_{z;i,j,k} = U^*_{x;i,j+1,k} U^*_{y;i,j,k} U_{x;i,j,k} U_{y;i+1,j,k}. \tag{2.25}$$

Observe that $W_{\mu;i,j,k}$, like $U_{\mu;i,j,k}$, is complex valued and unimodular: $W^*_{\mu;i,j,k} = W^{-1}_{\mu;i,j,k}$.

Lastly, we consider the supercurrent. The continuous variable is given in terms of the order parameter and link variables in (1.49). According to (2.16), we have

$$\begin{aligned} J_{s,x;i,j,k} = \frac{1}{2i\kappa}\Bigg(& \left(U^*_x\psi^*\right)\left(x_i + \tfrac{1}{2}h_x, y_j, z_k\right)\left(\frac{\partial\left(U_x\psi\right)}{\partial x}\right)\left(x_i + \tfrac{1}{2}h_x, y_j, z_k\right) \\ & -\left(U_x\psi\right)\left(x_i + \tfrac{1}{2}h_x, y_j, z_k\right)\left(\frac{\partial\left(U^*_x\psi^*\right)}{\partial x}\right)\left(x_i + \tfrac{1}{2}h_x, y_j, z_k\right)\Bigg). \end{aligned} \tag{2.26}$$

Here, we approximate the value of $U_x\psi$ at $\left(x_i + \tfrac{1}{2}h_x, y_j, z_k\right)$ by the average of its values at $\left(x_i, y_j, z_k\right)$ and $\left(x_{i+1}, y_j, z_k\right)$ and the value of its derivatives by the difference of its values at these points (central difference approximation),

$$\left(U_x\psi\right)\left(x_i + \tfrac{1}{2}h_x, y_j, z_k\right) = \tfrac{1}{2}\left(U_{x;i,j,k}\psi_{i+1,j,k} + \psi_{i,j,k}\right),$$

$$\left(\frac{\partial\left(U_x\psi\right)}{\partial x}\right)\left(x_i + \tfrac{1}{2}h_x, y_j, z_k\right) = \frac{U_{x;i,j,k}\psi_{i+1,j,k} - \psi_{i,j,k}}{h_x}.$$

Hence,

$$\begin{aligned} J_{s,x;i,j,k} &= \frac{1}{2i\kappa h_x}\left(U_{x;i,j,k}\psi^*_{i,j,k}\psi_{i+1,j,k} - U^*_{x;i,j,k}\psi_{i,j,k}\psi^*_{i+1,j,k}\right) \\ &= \frac{1}{\kappa h_x}\operatorname{Im}\left(U_{x;i,j,k}\psi^*_{i,j,k}\psi_{i+1,j,k}\right) \end{aligned}, \tag{2.27}$$

which expresses the x component of the supercurrent density in terms of the order parameter and link variables. The y and z components are treated similarly.

2.1.3 Discrete energy functional

We consider the various contributions to the free-energy functional. As before, we evaluate all integrals by means of the midpoint rule and approximate derivatives by central differences by central differences, so the resulting approximation is second-order accurate as the mesh width goes to zero. We omit the variable t (time is a parameter in the discretization) and use the symbol Σ_{cyclic} to indicate cyclic permutation according to the scheme

$$(x,y,z;i,j,k)\to(y,z,x;j,k,i)\to(z,x,y;k,i,j)\to(x,y,z;i,j,k).$$

The condensation energy is readily approximated,

$$L_{\text{cond}} \equiv \int_{\Omega_{sc}} \left(-(1-\gamma)|\psi|^2+\tfrac{1}{2}|\psi|^4\right)dxdydz$$
$$=\sum_{k=n_{sz}}^{n_{ez}}\sum_{j=n_{sy}}^{n_{ey}}\sum_{i=n_{sx}}^{n_{ex}}\int_{z_k-\frac{1}{2}h_z}^{z_k+\frac{1}{2}h_z}\int_{y_j-\frac{1}{2}h_y}^{y_j+\frac{1}{2}h_y}\int_{x_i-\frac{1}{2}h_x}^{x_i+\frac{1}{2}h_x}\left(-(1-\gamma)|\psi|^2+\tfrac{1}{2}|\psi|^4\right)dxdydz,$$

or

$$L_{\text{cond}}=\sum_{k=n_{sz}}^{n_{ez}}\sum_{j=n_{sy}}^{n_{ey}}\sum_{i=n_{sx}}^{n_{ex}}\left(-(1-\gamma_{i,j,k})|\psi_{i,j,k}|^2+\tfrac{1}{2}|\psi_{i,j,k}|^4\right)h_xh_yh_z. \tag{2.28}$$

Here γ is the material defect parameter (see section 1.3.6).

For the kinetic energy, we have

$$L_{\text{kin}}\equiv\frac{1}{k^2}\sum_{\mu=x,y,z}\int_{\Omega_{sc}}\left|\frac{\partial}{\partial\mu}(U_\mu\psi)\right|^2 dxdydz$$
$$=\frac{1}{k^2}\sum_{\text{cyclic}}\sum_{k=n}^{n_{ez}}\sum_{j=n}^{n_{ey}}\sum_{i=n}^{n_{ex}-1}\int_{z_k-\frac{1}{2}h_z}^{z_k+\frac{1}{2}h_z}\int_{y_j-\frac{1}{2}h_y}^{y_j+\frac{1}{2}h_y}\int_{x_i}^{x_{i+1}}\left|\frac{\partial}{\partial x}(U_x\psi)\right|^2 dxdydz,$$

or

$$\frac{1}{k^2}\sum_{\text{cyclic}}\sum_{k=n_{sz}}^{n_{ez}}\sum_{j=n_{sy}}^{n_{ey}}\sum_{i=n_{sx}}^{n_{ex}-1}\int_{z_k-\frac{1}{2}h_z}^{z_k+\frac{1}{2}h_z}\int_{y_j-\frac{1}{2}h_y}^{y_j+\frac{1}{2}h_y}\int_{x_i}^{x_{i+1}}\left|\frac{\partial}{\partial x}(U_x\psi)\right|^2 dxdydz,$$

$$L_{\text{kin}}=\frac{1}{k^2}\sum_{\text{cyclic}}\sum_{k=n_{sz}}^{n_{ez}}\sum_{j=n_{sy}}^{n_{ey}}\sum_{i=n_{sx}}^{n_{ex}-1}\left|\frac{U_{x;i,j,k}\psi_{i+1,j,k}-\psi_{i,j,k}}{h_x}\right|^2 h_xh_yh_z. \tag{2.29}$$

Lastly, we have the magnetic field energy,

$$L_{\text{magn}} \equiv \int_{\Omega} \left|\nabla \times \mathbf{A}\right|^2 dxdydz = \sum_{i,j,k} \sum_{\text{cyclic}} \int_{z_k-\frac{1}{2}h_z}^{z_k+\frac{1}{2}h_z} \int_{y_j}^{y_{j+1}} \int_{x_i}^{x_{i+1}} \left|B_z\right|^2 dxdydz\,,$$

or

$$L_{\text{magn}} = \sum_{i,j,k} \sum_{\text{cyclic}} \left|B_{z;i,j,k}\right|^2 h_x h_y h_z = \sum_{\text{cyclic}} \sum_{i,j,k} \frac{\left|1-W_{z;i,j,k}\right|^2}{\kappa^2 h_x^2 h_y^2} h_x h_y h_z\,. \tag{2.30}$$

The discrete energy functional is a sum of (2.28), (2.29) and (2.30):

$$\boxed{\begin{gathered} L[\psi,\mathbf{U}] = L_{\text{cond}} + L_{\text{kin}} + L_{\text{magn}} = \sum_{i,j,k} h_x h_y h_z \cdot \\ \left(-\left(1-\gamma_{i,j,k}\right)\left|\psi_{i,j,k}\right|^2 + \tfrac{1}{2}\left|\psi_{i,j,k}\right|^4 + \frac{1}{k^2} \sum_{\text{cyclic}} \left| \frac{U_{x;i,j,k}\psi_{i+1,j,k} - \psi_{i,j,k}}{h_x} \right|^2 + \sum_{\text{cyclic}} \frac{\left|1-W_{z;i,j,k}\right|^2}{\kappa^2 h_x^2 h_y^2} \right). \end{gathered}} \tag{2.31}$$

2.1.4 Equations of motion

It remains to take the derivatives of the discrete energy functional and derive the analog of (1.41) and (1.42). Because the TDGL model involves a diffusion effect that is nonlocal in terms of **A**, but local in terms of **U**, it is most convenient to formulate the discrete TDGL model in terms of the discrete vectors ψ and **U**. From (2.17) we obtain the relations

$$\frac{\partial U_{\mu;i,j,k}}{\partial A_{\mu;i,j,k}} = -i\kappa h_\mu U_{\mu;i,j,k}\,,\quad \mu = x, y, z\,. \tag{2.32}$$

The equation of motion for the order parameter is

$$\boxed{\frac{\partial \psi_{i,j,k}}{\partial t} = \left(F_\psi\left[\psi,\mathbf{U}\right]\right)_{i,j,k}}\,, \tag{2.33}$$

where

$$\boxed{\begin{aligned}\left(F_\psi[\psi,\mathbf{U}]\right)_{i,j,k} &= \left(\left(1-\gamma_{i,j,k}\right)-\left|\psi_{i,j,k}\right|^2\right)\psi_{i,j,k} \\ &+\frac{1}{\kappa^2}\sum_{\text{cyclic}}\frac{U_{x;i,j,k}\psi_{i+1,j,k}-2\psi_{i,j,k}+U^*_{x;i-1,j,k}\psi_{i-1,j,k}}{h_x^2}.\end{aligned}} \tag{2.34}$$

The cyclic sum in $F_\psi[\psi, \mathbf{U}]$ is a discretization of a *weighted Laplacian*; the weight at any point is determined by the values of the vector $\mathbf{U}$ at the point itself and its nearest neighbors.

The equation of motion for U_x is

$$\boxed{\frac{\partial U_{x;i,j,k}}{\partial t}=-\frac{i}{\sigma}U_{x;i,j,k}\left(F_\mathrm{U}\left[\psi,U_x\right]\right)_{i,j,k}}, \tag{2.35}$$

where

$$\boxed{\left(F_\mathrm{U}\left[\psi,U_x\right]\right)_{i,j,k}=\operatorname{Im}\left(\frac{W_{z;i,j,k}-W_{z;i,j-1,k}}{h_y^2}-\frac{W_{y;i,j,k}-W_{y;i,j,k-1}}{h_z^2}+U_{x;i,j,k}\psi^*_{i,j,k}\psi_{i+1,j,k}\right)}. \tag{2.36}$$

The equations for U_y and U_z are obtained by cyclic permutation.

A simple first-order approximation is used to evaluate the time-derivatives in (2.33) and (2.35):

$$\frac{\partial\psi_{i,j,k}}{\partial t}\approx\frac{\psi^{(n+1)}_{i,j,k}-\psi^{(n)}_{i,j,k}}{\Delta t}, \tag{2.37}$$

$$\frac{\partial U_{x;i,j,k}}{\partial t}\approx\frac{U^{(n+1)}_{x;i,j,k}-U^{(n)}_{x;i,j,k}}{\Delta t}. \tag{2.38}$$

In section 2.2 we will describe in detail how equations of motion (2.33)–(2.38) are solved numerically.

2.1.5 Boundary conditions

The boundary $\partial\Omega_{sc}$ consists of six two-dimensional planar surfaces, orthogonal to the coordinate axes and located at $x = x_{n_{sx}} + \frac{1}{2}h_x$ ("left") and $x = x_{n_{ex}-1} + \frac{1}{2}h_x$ ("right"), $y = y_{n_{sy}} + \frac{1}{2}h_y$ ("front") and $y = y_{n_{ey}-1} + \frac{1}{2}h_y$ ("back"), and $z = z_{n_{sz}} + \frac{1}{2}h_z$ ("bottom") and $z = z_{n_{ez}-1} + \frac{1}{2}h_z$ ("top"); see (2.3). They are surfaces of continuity for the magnetic field. Our definition of the discrete variables accomplishes this continuity to second-order accuracy in the mesh size, because the magnetic field is evaluated at points on the surfaces. We incorporate the boundary condition $\mathbf{J}_s \cdot \mathbf{n} = 0$ by imposing constraints on the discrete variables. For example, on the left face we impose the constraint

$$\psi_{n_{sx},j,k} = U_{x;n_{sx},j,k}\psi_{n_{sx}+1,j,k}, \quad j = n_{sy},\ldots,n_{ey}, \quad k = n_{sz},\ldots,n_{ez}, \tag{2.39}$$

and on the right face,

$$\psi_{n_{ex},j,k} = U^*_{x;n_{ex}-1,j,k}\psi_{n_{ex}-1,j,k}, \quad j = n_{sy},\ldots,n_{ey}, \quad k = n_{sz},\ldots,n_{ez}, \tag{2.40}$$

and similarly in the other directions.

The outer boundary $\partial\Omega$ consists of six two-dimensional planar surfaces, orthogonal to the coordinate axes and located at $x = x_1 + \frac{1}{2}h_x$ ("left") and $x = x_{n_x} + \frac{1}{2}h_x$ ("right"), $y = y_1 + \frac{1}{2}h_y$ ("front") and $y = y_{n_y} + \frac{1}{2}h_y$ ("back"), and $z = z_1 + \frac{1}{2}h_z$ ("bottom") and $z = z_{n_z} + \frac{1}{2}h_z$ ("top"); see (2.2). Here, the induced magnetic field **B** must be matched to the applied magnetic field $\mathbf{H} = (H_x, H_y, H_z)$, which is uniform. If there is no surface current, the matching is continuous; otherwise, there is a jump discontinuity in the tangential components. We assume that the surface current density on $\partial\Omega$ is **K**. We accomplish the matching by imposing constraints on the discrete variables. For example, on the left and right face we impose the constraints

$$B_{z;1,j,k} = H_z - K_y\left(x_1 + \tfrac{1}{2}h_x, y_j + \tfrac{1}{2}h_y, z_k\right), \tag{2.41}$$

$$B_{z;n_x,j,k} = H_z + K_y\left(x_{n_x} + \tfrac{1}{2}h_x, y_j + \tfrac{1}{2}h_y, z_k\right), \tag{2.42}$$

on the front and back face,

$$B_{z;i,1,k} = H_z + K_x\left(x_i + \tfrac{1}{2}h_x, y_1 + \tfrac{1}{2}h_y, z_k\right), \tag{2.43}$$

$$B_{z;i,n_y,k} = H_z - K_x\left(x_i + \tfrac{1}{2}h_x, y_{n_y} + \tfrac{1}{2}h_y, z_k\right), \tag{2.44}$$

and on the bottom and top face,

$$B_{z;i,j,1} = H_z, \tag{2.45}$$

$$B_{z;i,j,n_z} = H_z, \tag{2.46}$$

Similar constraints hold for the x and y components of magnetic field.

2.2 The Numerical Methods

Discretized TDGL equations (2.33)–(2.38) can be solved numerically by various methods, which depend on which terms in the final equation are to be evaluated for the new time step $(n + 1)$ or used to compute the new values from the previous time step (n). We will consider two such methods: the simplest, a forward-Euler explicit scheme, and more complicated, but much more efficient, alternating-direction implicit method (ADI), described in Section 2.2.2.

Integrating the TDGL equations to a steady state is a time-consuming process requiring considerable computing resources. In the simulations of vortex dynamics using the simple one-step Euler integration procedure, some authors routinely experienced computational times on the order of one hundred hours [15], [16]. Incremental changes would gradually drive the system to lower energy levels. These very long equilibration times arise, of course, because we are dealing with large physical systems undergoing a phase transition. The energy landscape for such systems is a broad gently undulating plain with many shallow local minima. It is therefore important to develop efficient integration techniques that remain accurate and stable as the time step increases.

Due to shear efficiency of the ADI method compared to Euler scheme, it was used in all numerical simulations presented in this thesis.

2.2.1 Explicit Euler method

With the *explicit* Euler method, the right part of the equations (2.33) and (2.35) are evaluated at time step (n), which leaves the single unknown variable at time step ($n + 1$) in the left part. This leads to simple integration scheme

$$\psi^{(n+1)}_{i,j,k} = \psi^{(n)}_{i,j,k} + \left(F_\psi\left[\psi^{(n)}, \mathbf{U}^{(n)}\right]\right)_{i,j,k} \Delta t, \tag{2.47}$$

$$U^{(n+1)}_{x;i,j,k} = U^{(n)}_{x;i,j,k} - \frac{i}{\sigma} U^{(n)}_{x;i,j,k} \left(F_{\mathrm{U}}\left[\psi^{(n)}, U^{(n)}_x\right]\right)_{i,j,k} \Delta t, \tag{2.48}$$

and similarly for the other components.

The advantage of the Euler one-step procedure is that the storage of only one generation of data (which can take a lot of memory in large-scale tree-dimensional simulations) is required, and the programming of the algorithm is simple. Also, the Euler method lends itself to data structures that are easily parallelized for use in multiprocessor or cluster environment. The disadvantage is that the time step suffers a severe limitation due to the stability limits imposed by explicit forward-integration method. In the scaled time units used in the dimensionless equations, $\Delta t = 0.0025$ is just below this limit. Euler algorithm provides highly accurate solutions, but requires a significant number (of the order of millions) of time steps for equilibration. The implicit scheme presented in the next section allows for a dramatic increase (e.g., 40-fold) in the time step size.

2.2.2 Alternating-direction implicit method

With the *implicit* method, the right parts of the equations (2.33) and (2.35) are evaluated at time step ($n + 1$). These future values are implicitly determined by the past values. This creates a system of equations, which can be inverted to determine the future values through the past ones. We call this the alternating-direction implicit method (ADI). The greater stability of ADI compared to the explicit Euler method follows because looking into the future in this way helps move information through the solution more quickly.

The implicit method solves for the vector potential **A** directly, instead of for the link variable **U**. So we follow the dynamics of ψ and **A** in this formulation. This is done using the zero-potential gauge so that the equations retain their gauge invariance. The link variables are used only for computing the individual terms in the ψ equation, where they are calculated in terms of **A** and not solved-for directly.

For the sake of simplicity, we will describe the use of the implicit method in two dimensions only; in 3D, the logic is the basically the same.

We will consider two cases in 2D, with normal-superconductor boundary in y-direction (in which case there is no transport current in y-direction) – we will refer to this configuration as '*non-periodic boundary*' (Figure 6a); and with a periodic superconductor structure in y-direction (the transport current can be put in y-direction by specifying different values for the magnetic field on the left and on the right side) – '*periodic boundary*' (Figure 6b). The period in y-direction is equal to the length of the superconductor in this direction, that is, $y_{n_y} - y_1$.

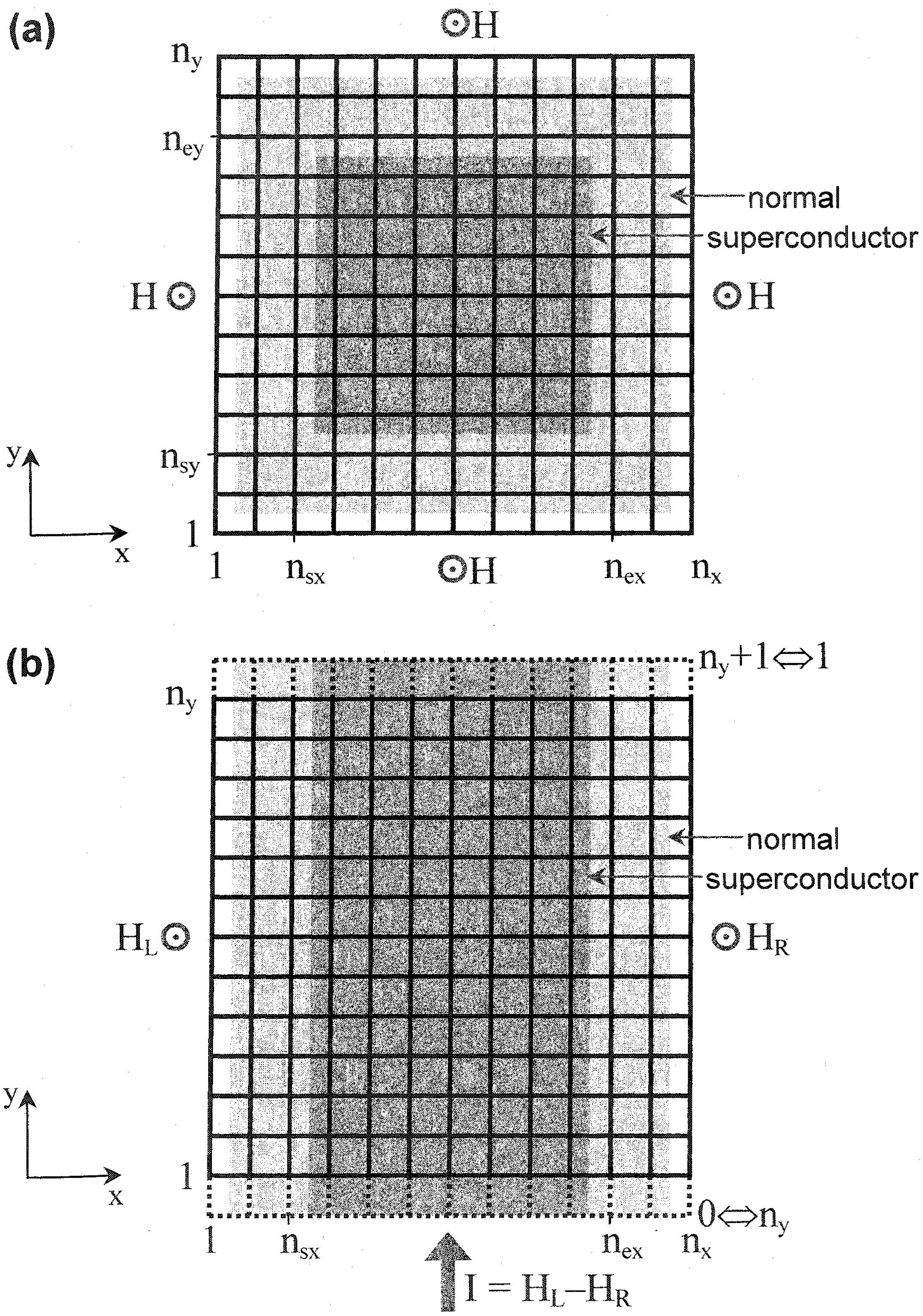

Figure 6. 2D configurations with non-periodic (*a*) and periodic (*b*) boundary in *y*-direction.

Let us begin with the ψ equation first. From (2.33), (2.34) and (2.37), we have in two dimensions

$$\boxed{\begin{aligned} \frac{\psi_{i,j}^{(n+1)}-\psi_{i,j}^{(n)}}{\Delta t} = & \left(\left(1-\gamma_{i,j}\right)-\left|\psi_{i,j}^{(n)}\right|^2\right)\psi_{i,j}^{(n+1)} \\ & +\frac{U_{x;i,j}^{(n)}\psi_{i+1,j}^{(n+1)}-2\psi_{i,j}^{(n+1)}+U_{x;i-1,j}^{*(n)}\psi_{i-1,j}^{(n+1)}}{\kappa^2 h_x^2} \\ & +\frac{U_{y;i,j}^{(n)}\psi_{i,j+1}^{(n+1)}-2\psi_{i,j}^{(n+1)}+U_{y;i,j-1}^{*(n)}\psi_{i,j-1}^{(n+1)}}{\kappa^2 h_y^2}. \end{aligned}} \tag{2.49}$$

Strictly speaking, this is a *semi-implicit*, rather than an implicit equation, since not all terms in the derivative can be evaluated at time step (n + 1); here, we have terms with link variables, which are evaluated at time step (n), and also a nonlinear term, which is also evaluated at time step (n) to avoid nonlinearity in the system of equations.

Equation (2.49) is implicit in both x and y directions, and can be solved using methods of matrix algebra; however, such a solution requires a lot of computational effort: for the matrix of size N, a number $O(N^2)$ of operations is required. The *alternating-direction implicit* method (ADI) [6] dramatically reduces the number of operations to $O(N)$ by using the principle of operator splitting. In 2D, instead of advancing both coordinates in one step, the x coordinates are advanced in a first implicit step of $\Delta t/2$ (time step (n + ½)):

$$\begin{aligned} \frac{\psi_{i,j}^{(n+\frac{1}{2})}-\psi_{i,j}^{(n)}}{\Delta t/2} = & \left(\left(1-\gamma_{i,j}\right)-\left|\psi_{i,j}^{(n)}\right|^2\right)\psi_{i,j}^{(n+\frac{1}{2})} \\ & +\frac{U_{x;i,j}^{(n)}\psi_{i+1,j}^{(n+\frac{1}{2})}-2\psi_{i,j}^{(n+\frac{1}{2})}+U_{x;i-1,j}^{*(n)}\psi_{i-1,j}^{(n+\frac{1}{2})}}{\kappa^2 h_x^2} \\ & +\frac{U_{y;i,j}^{(n)}\psi_{i,j+1}^{(n)}-2\psi_{i,j}^{(n)}+U_{y;i,j-1}^{*(n)}\psi_{i,j-1}^{(n)}}{\kappa^2 h_y^2}, \end{aligned} \tag{2.50}$$

and then in a second implicit step of $\Delta t/2$ (time step (n + 1)) the y coordinates are advanced:

$$\begin{aligned}\frac{\psi_{i,j}^{(n+1)}-\psi_{i,j}^{(n+\frac{1}{2})}}{\Delta t/2} = &\left(\left(1-\gamma_{i,j}\right)-\left|\psi_{i,j}^{(n+\frac{1}{2})}\right|^2\right)\psi_{i,j}^{(n+1)} \\ &+\frac{U_{x;i,j}^{(n+\frac{1}{2})}\psi_{i+1,j}^{(n+\frac{1}{2})}-2\psi_{i,j}^{(n+\frac{1}{2})}+U_{x;i-1,j}^{*(n+\frac{1}{2})}\psi_{i-1,j}^{(n+\frac{1}{2})}}{\kappa^2 h_x^2} \\ &+\frac{U_{y;i,j}^{(n+\frac{1}{2})}\psi_{i,j+1}^{(n+1)}-2\psi_{i,j}^{(n+1)}+U_{y;i,j-1}^{*(n+\frac{1}{2})}\psi_{i,j-1}^{(n+1)}}{\kappa^2 h_y^2}\end{aligned} \tag{2.51}$$

(see Figure 7).

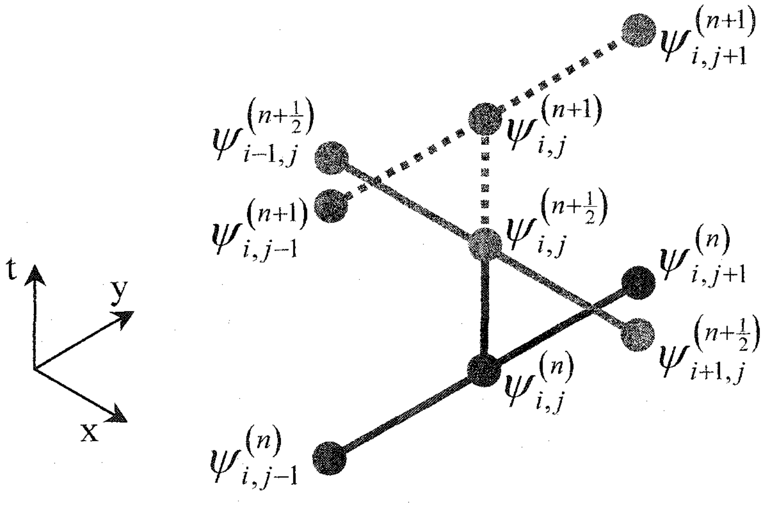

Figure 7. Computational clusters for alternating implicit steps for the x (solid) and y (dashed) coordinates.

Let us show how the x-equation (2.50) is solved. For given index j, we make the following notations:

$$m=i-n_{sx}+1, \quad i=n_{sx},\ldots,n_{ex}, \quad m=1,\ldots,N, \quad N=n_{ex}-n_{sx}+1 \tag{2.52}$$

$$u_{m-1}\equiv\psi_{i-1,j}^{(n+\frac{1}{2})},\ u_m\equiv\psi_{i,j}^{(n+\frac{1}{2})},\ u_{m+1}\equiv\psi_{i+1,j}^{(n+\frac{1}{2})}, \tag{2.53}$$

$$a_m=-\frac{\Delta t}{2\kappa^2 h_x^2}U_{x;i-1,j}^{*(n)}, \tag{2.54}$$

$$b_m = 1 - \frac{\Delta t}{2}\left(\left(1-\gamma_{i,j}\right) - \left|\psi_{i,j}^{(n)}\right|^2\right) + \frac{\Delta t}{\kappa^2 h_x^2}, \tag{2.55}$$

$$c_m = -\frac{\Delta t}{2\kappa^2 h_x^2} U_{x;i,j}^{(n)}, \tag{2.56}$$

$$d_m = \psi_{i,j}^{(n)} + \frac{\Delta t}{2\kappa^2 h_y^2}\left(U_{y;i,j}^{(n)}\psi_{i,j+1}^{(n)} - 2\psi_{i,j}^{(n)} + U_{y;i,j-1}^{*(n)}\psi_{i,j-1}^{(n)}\right). \tag{2.57}$$

Then we have a set of linear equations

$$\boxed{a_m u_{m-1} + b_m u_m + c_m u_{m+1} = d_m}, \tag{2.58}$$

which can be written in matrix form as

$$\begin{pmatrix} b_1 & c_1 & & & & & \\ a_2 & b_2 & c_2 & & & & \\ & a_3 & b_3 & c_3 & & & \\ & & \cdot & \cdot & \cdot & & \\ & & & \cdot & \cdot & \cdot & \\ & & & & a_{N-1} & b_{N-1} & c_{N-1} \\ & & & & & a_N & b_N \end{pmatrix} \begin{pmatrix} u_1 \\ u_2 \\ u_3 \\ \cdot \\ \cdot \\ u_{N-1} \\ u_N \end{pmatrix} = \begin{pmatrix} d_1 \\ d_2 \\ d_3 \\ \cdot \\ \cdot \\ d_{N-1} \\ d_N \end{pmatrix}, \tag{2.59}$$

or

$$\mathbf{Mu} = \mathbf{d}, \tag{2.60}$$

where **M**, **u**, and **d** are the corresponding matrix and column vectors. Note that **M** is a *tridiagonal* matrix (all the elements are zero, except for the diagonal and the adjacent elements), and it can easily be inverted to find unknown **u** without doing all the work needed to invert an arbitrary matrix.

We split **M** into a product of a lower-diagonal and an upper-diagonal matrix: $\mathbf{M} = \mathbf{M}_l\mathbf{M}_u$, and let $\mathbf{d}' = \mathbf{M}_u\mathbf{u}$. We then have two equations to solve:

$$\mathbf{M}_l\mathbf{d}' = \mathbf{d}, \quad \text{for } \mathbf{d}' \text{ (forward solution)}, \tag{2.61}$$

$$\mathbf{M}_u\mathbf{u} = \mathbf{d}', \quad \text{for } \mathbf{u} \text{ (backward solution)}. \tag{2.62}$$

The solutions are trivial because of the use of the upper and lower diagonal matrices. All that is left to be done is to produce the decomposition **M** = $\mathbf{M}_l\mathbf{M}_u$. We begin by writing

$$\begin{pmatrix} b_1 & c_1 & & & \\ a_2 & b_2 & c_2 & & \\ & a_3 & b_3 & c_3 & \\ & & . & . & . \end{pmatrix} = \begin{pmatrix} b_1' & & & \\ a_2 & b_2' & & \\ & a_3 & b_3' & \\ & & . & . \end{pmatrix} \begin{pmatrix} 1 & c_1' & & & \\ & 1 & c_2' & & \\ & & 1 & c_3' & \\ & & & & . \end{pmatrix}, \tag{2.63}$$

which gives the following formulae for the coefficients b_m' and c_m':

$$\begin{aligned} &b_1' = b_1, \quad c_1' = \frac{c_1}{b_1}, \\ &b_m' = b_m - a_m c_{m-1}', \quad c_m' = \frac{c_m}{b_m'}, \quad m = 2,\ldots,N. \end{aligned} \tag{2.64}$$

The solution for **d**′ is then taken from

$$\begin{pmatrix} b_1' & & & \\ a_2 & b_2' & & \\ & a_3 & b_3' & \\ & & . & . \end{pmatrix} \begin{pmatrix} d_1' \\ d_2' \\ d_3' \\ . \end{pmatrix} = \begin{pmatrix} d_1 \\ d_2 \\ d_3 \\ . \end{pmatrix}, \tag{2.65}$$

which gives us the algorithm for the *forward pass*:

$$\boxed{\begin{aligned} &c_1' = \frac{c_1}{b_1}, \quad d_1' = \frac{d_1}{b_1}, \\ &c_m' = \frac{c_m}{b_m - a_m c_{m-1}'}, \quad d_m' = \frac{d_m - a_m d_{m-1}'}{b_m - a_m c_{m-1}'}, \quad m = 2,\ldots,N. \end{aligned}} \tag{2.66}$$

Finally, we get the solution to **u** from

$$\begin{pmatrix} 1 & c_1' & & \\ & 1 & c_2' & \\ & & 1 & c_3' \\ & & & . \end{pmatrix} \begin{pmatrix} u_1 \\ u_2 \\ u_3 \\ . \end{pmatrix} = \begin{pmatrix} d_1' \\ d_2' \\ d_3' \\ . \end{pmatrix}, \tag{2.67}$$

giving us the *reverse pass*

$$\boxed{\begin{aligned} &u_N = d'_N, \\ &u_m = d'_m - c'_m u_{m+1}, \quad m = N-1,\dots,1. \end{aligned}} \tag{2.68}$$

This is an $O(N)$ steps algorithm, and so there is little performance penalty for using an implicit discretization instead of an explicit one. Moreover, due to the much greater stability of the implicit method, we can use a much larger time step than with the explicit method and thus integrate the solution much more quickly.

At this point we should mention the boundary conditions. For $m = 1$ ($i = n_{sx}$) we have the boundary condition

$$\psi_{n_{sx},j} = U_{x;n_{sx},j}\psi_{n_{sx}+1,j}, \tag{2.69}$$

which is of the form $b_1 u_1 + c_1 u_2 = d_1$ with coefficients b_1, c_1, and d_1, different from what is given by (2.55), (2.56), and (2.57):

$$b_1 = 1, \quad c_1 = -U^{(n)}_{x;n_{sx},j}, \quad d_1 = 0. \tag{2.70}$$

Similarly, for $m = N$ ($i = n_{ex} - 1$) we have the boundary condition

$$\psi_{n_{ex},j} = U^*_{x;n_{ex}-1,j}\psi_{n_{ex}-1,j}, \tag{2.71}$$

which is of the form $a_N u_{N-1} + b_N u_N = d_N$ with coefficients a_N, b_N, and d_N, different from what is given by (2.54), (2.55), and (2.57):

$$a_N = -U^{*(n)}_{x;n_{ex},j}, \quad b_N = 1, \quad d_N = 0. \tag{2.72}$$

Special consideration should be paid to the bottom and top boundaries in y-direction.

In non-periodic boundary case, index j in equations (2.49)–(2.72) can take values $j = n_{sy+1},\dots,n_{ey-1}$, and to determine ψ at $j = n_{sy}$ and $j = n_{ey}$, we use boundary conditions

$$\psi_{i,n_{sy}} = U_{y;i,n_{sy}}\psi_{i,n_{sy}+1}, \tag{2.73}$$

$$\psi_{i,n_{ey}} = U^{*}_{y;i,n_{ey}-1}\psi_{i,n_{ey}-1} \tag{2.74}$$

for all $i = n_{sx},\ldots,n_{ex}$.

In the periodic boundary case, j can take on values $j = 1,\ldots,n_y$. For $j = 2,\ldots,n_y-1$ we use coefficients (2.54)–(2.57) and (2.70), (2.72), as usual. However, for $j = 1$ we have a term $U^{*(n)}_{y;i,0}\psi^{(n)}_{i,0}$ in (2.57), which we replace with $U^{*(n)}_{y;i,n_y}\psi^{(n)}_{i,n_y}$ due to periodicity in y-direction (index 0 wraps to n_y). Therefore,

$$d_m = \psi^{(n)}_{i,1} + \frac{\Delta t}{2\kappa^2 h_y^2}\left(U^{(n)}_{y;i,1}\psi^{(n)}_{i,2} - 2\psi^{(n)}_{i,1} + U^{*(n)}_{y;i,n_y}\psi^{(n)}_{i,n_y}\right) \quad \text{for } j = 1. \tag{2.75}$$

For $j = n_y$ we have a term $U^{(n)}_{y;i,n_y}\psi^{(n)}_{i,n_y+1}$ in (2.57), which we replace with $U^{(n)}_{y;i,n_y}\psi^{(n)}_{i,1}$ (index n_y+1 wraps to 1). Therefore,

$$d_m = \psi^{(n)}_{i,n_y} + \frac{\Delta t}{2\kappa^2 h_y^2}\left(U^{(n)}_{y;i,n_y}\psi^{(n)}_{i,1} - 2\psi^{(n)}_{i,n_y} + U^{*(n)}_{y;i,n_y-1}\psi^{(n)}_{i,n_y-1}\right) \quad \text{for } j = n_y. \tag{2.76}$$

After we find $\psi^{(n+\frac{1}{2})}_{i,j}$ for all possible i and j, we turn to solving the y-step equation (2.51). We notice that it contains unknown link variables $U^{(n+\frac{1}{2})}_x$ and $U^{(n+\frac{1}{2})}_y$, which we must calculate from corresponding values $A^{(n+\frac{1}{2})}_x$ and $A^{(n+\frac{1}{2})}_y$ using equation (2.17). So now we should make the first half-step in A_x- and A_y-equations.

In 2D and with a zero potential gauge, the equation (1.48) can be written as a pair of equations

$$\boxed{\sigma\frac{\partial A_x}{\partial t} = J_{s,x} - \frac{\partial B}{\partial y}}, \tag{2.77}$$

$$\boxed{\sigma\frac{\partial A_y}{\partial t} = J_{s,y} + \frac{\partial B}{\partial x}}, \tag{2.78}$$

where the superconducting current J_s is given by (2.27). As for the magnetic field B, we express it in terms of A_x, A_y using Stokes' identity

$$\iint_D B\,dxdy = \oint_{\partial D} \mathbf{A}\cdot d\mathbf{t}\,,$$

integrated over one mesh cell:

$$h_x h_y B_{i,j} = h_x A_{x;i,j} + h_y A_{y;i+1,j} - h_x A_{x;i,j+1} - h_y A_{y;i,j}\,,$$

giving us

$$B_{i,j} = \frac{A_{y;i+1,j} - A_{y;i,j}}{h_x} - \frac{A_{x;i,j+1} - A_{x;i,j}}{h_y}\,. \tag{2.79}$$

The derivatives of B are calculated using the first order approximation, e.g.

$$\frac{\partial B}{\partial x} \approx \frac{B_{i,j} - B_{i-1,j}}{h_x}\,.$$

Let us make the following notations:

$$\beta_x = \frac{\Delta t}{h_x^2},\quad \beta_y = \frac{\Delta t}{h_y^2},\quad \beta_{xy} = \frac{\Delta t}{h_x h_y},\quad \alpha_x = \sigma + \beta_x,\quad \alpha_y = \sigma + \beta_y\,. \tag{2.80}$$

Then we have implicit equations for A_x and A_y:

$$\boxed{\begin{aligned}\sigma\left(A_{x;i,j}^{(n+1)} - A_{x;i,j}^{(n)}\right) &= J_{s,x;i,j}^{(n)}\Delta t + \beta_y\left(A_{x;i,j+1}^{(n+1)} - 2A_{x;i,j}^{(n+1)} + A_{x;i,j-1}^{(n+1)}\right)\\ &\quad -\beta_{xy}\left(A_{y;i+1,j}^{(n+1)} - A_{y;i,j}^{(n+1)} - A_{y;i+1,j-1}^{(n+1)} + A_{y;i,j-1}^{(n+1)}\right),\end{aligned}} \tag{2.81}$$

$$\boxed{\begin{aligned}\sigma\left(A_{y;i,j}^{(n+1)} - A_{y;i,j}^{(n)}\right) &= J_{s,y;i,j}^{(n)}\Delta t + \beta_x\left(A_{y;i+1,j}^{(n+1)} - 2A_{y;i,j}^{(n+1)} + A_{y;i-1,j}^{(n+1)}\right)\\ &\quad -\beta_{xy}\left(A_{x;i,j+1}^{(n+1)} - A_{x;i,j}^{(n+1)} - A_{x;i-1,j+1}^{(n+1)} + A_{x;i-1,j}^{(n+1)}\right).\end{aligned}} \tag{2.82}$$

Applying the ADI method to these equations, we have two semi-implicit equations to solve for the first half time step:

$$\begin{aligned}\sigma\left(A_{x;i,j}^{(n+\frac{1}{2})} - A_{x;i,j}^{(n)}\right) &= J_{s,x;i,j}^{(n)}\frac{\Delta t}{2} + \frac{\beta_y}{2}\left(A_{x;i,j+1}^{(n+\frac{1}{2})} - 2A_{x;i,j}^{(n+\frac{1}{2})} + A_{x;i,j-1}^{(n+\frac{1}{2})}\right)\\ &\quad -\frac{\beta_{xy}}{2}\left(A_{y;i+1,j}^{(n)} - A_{y;i,j}^{(n)} - A_{y;i+1,j-1}^{(n)} + A_{y;i,j-1}^{(n)}\right),\end{aligned} \tag{2.83}$$

$$\sigma\left(A_{y;i,j}^{\left(n+\frac{1}{2}\right)}-A_{y;i,j}^{(n)}\right)=J_{s,y;i,j}^{(n)}\frac{\Delta t}{2}+\frac{\beta_x}{2}\left(A_{y;i+1,j}^{\left(n+\frac{1}{2}\right)}-2A_{y;i,j}^{\left(n+\frac{1}{2}\right)}+A_{y;i-1,j}^{\left(n+\frac{1}{2}\right)}\right)$$
$$-\frac{\beta_{xy}}{2}\left(A_{x;i,j+1}^{(n)}-A_{x;i,j}^{(n)}-A_{x;i-1,j+1}^{(n)}+A_{x;i-1,j}^{(n)}\right). \tag{2.84}$$

Note that in the A_x-equation indices can take values $i = 1,\dots,n_x - 1$, $j = 1,\dots,n_y$, while in the A_y-equation $i = 1,\dots,n_x$, $j = 1,\dots,n_y - 1$ for non-periodic boundary and $i = 1,\dots,n_x$, $j = 1,\dots,n_y$ for periodic boundary.

Let us consider the A_x-equation first. The solution is obtained using the forward/backward matrix method described above, in the y-direction, with the following coefficients:

$$m=j,\quad j=1,\dots,n_y,\quad m=1,\dots,N,\quad N=n_y,$$

$$u_{m-1}\equiv A_{x;i,j-1}^{\left(n+\frac{1}{2}\right)},\ u_m\equiv A_{x;i,j}^{\left(n+\frac{1}{2}\right)},\ u_{m+1}\equiv A_{x;i,j+1}^{\left(n+\frac{1}{2}\right)},$$

$$a_m=-\frac{\beta_y}{2}, \tag{2.85}$$

$$b_m=\alpha_y, \tag{2.86}$$

$$c_m=-\frac{\beta_y}{2}, \tag{2.87}$$

$$d_m=\sigma A_{x;i,j}^{(n)}+J_{s,x;i,j}^{(n)}\frac{\Delta t}{2}-\frac{\beta_{xy}}{2}\left(A_{y;i+1,j}^{(n)}-A_{y;i,j}^{(n)}-A_{y;i+1,j-1}^{(n)}+A_{y;i,j-1}^{(n)}\right). \tag{2.88}$$

In non-periodic boundary case, the boundary condition to be satisfied is the equations giving the values of the external field at the bottom and top interfaces:

$$A_{x;i,1}=A_{x;i,2}+h_yH, \tag{2.89}$$

$$A_{x;i,n_y}=A_{x;i,n_y-1}-h_yH, \tag{2.90}$$

where H is the applied magnetic field. Therefore, we have the 'boundary' coefficients

$$b_1=1,\quad c_1=-1,\quad d_1=h_yH, \tag{2.91}$$

$$a_N = -1, \quad b_N = 1, \quad d_N = -h_y H \,. \tag{2.92}$$

In the periodic boundary case, for $j = 1$ we have terms $A^{(n+\frac{1}{2})}_{x;i,0}$, $A^{(n)}_{y;i+1,0}$, $A^{(n)}_{y;i,0}$ in (2.83), which we replace with $A^{(n)}_{x;i,n_y}$, $A^{(n)}_{y;i+1,n_y}$, $A^{(n)}_{y;i,n_y}$, respectively (since the index 0 wraps to n_y). Note that we use the value of A_x at time step (n) rather than (n + ½) in order to have a tridiagonal matrix (otherwise, we will have a tridiagonal matrix with two additional elements at the upper-right and lower-left corners, and inverting such a matrix will take $O(N^2)$ operations). Therefore,

$$\begin{aligned} d_m = \sigma A^{(n)}_{x;i,1} + J^{(n)}_{s,x;i,1}\frac{\Delta t}{2} - \frac{\beta_{xy}}{2}\left(A^{(n)}_{y;i+1,1} - A^{(n)}_{y;i,1} - A^{(n)}_{y;i+1,n_y} + A^{(n)}_{y;i,n_y}\right) \\ + \frac{\beta_y}{2}A^{(n)}_{x;i,n_y} \quad \text{for } j = 1. \end{aligned} \tag{2.93}$$

For $j = n_y$ we have a term $A^{(n+\frac{1}{2})}_{x;i,n_y+1}$ in (2.83), which we replace with $A^{(n)}_{x;i,1}$ (since the index $n_y + 1$ wraps to 1; note again, that we evaluated A_x at time step (n) rather than (n + ½) to keep the matrix tridiagonal). Thus,

$$\begin{aligned} d_m = \sigma A^{(n)}_{x;i,n_y} + J^{(n)}_{s,x;i,n_y}\frac{\Delta t}{2} - \frac{\beta_{xy}}{2}\left(A^{(n)}_{y;i+1,n_y} - A^{(n)}_{y;i,n_y} - A^{(n)}_{y;i+1,n_y-1} + A^{(n)}_{y;i,n_y-1}\right) \\ + \frac{\beta_y}{2}A^{(n)}_{x;i,1} \quad \text{for } j = n_y. \end{aligned} \tag{2.94}$$

After the A_x-equation is solved, the A_y-equation (2.84) is solved analogously in the x-direction. Then we recalculate the link variables U_x, U_y at time step (n + ½) and in sequence solve the ψ-equation for time step (n + 1) in the y-direction (2.51), recalculate the current J_s at time step (n + ½), and solve the A_x-equation for time step (n + 1) in the y-direction:

$$\begin{aligned} \sigma\left(A^{(n+1)}_{x;i,j} - A^{(n+\frac{1}{2})}_{x;i,j}\right) = J^{(n+\frac{1}{2})}_{s,x;i,j}\frac{\Delta t}{2} + \frac{\beta_y}{2}\left(A^{(n+1)}_{x;i,j+1} - 2A^{(n+1)}_{x;i,j} + A^{(n+1)}_{x;i,j-1}\right) \\ - \frac{\beta_{xy}}{2}\left(A^{(n+\frac{1}{2})}_{y;i+1,j} - A^{(n+\frac{1}{2})}_{y;i,j} - A^{(n+\frac{1}{2})}_{y;i+1,j-1} + A^{(n+\frac{1}{2})}_{y;i,j-1}\right), \end{aligned} \tag{2.95}$$

and finally, solve the A_y-equation for time step $(n + 1)$ in the x-direction:

$$\begin{aligned}\sigma\left(A_{y;i,j}^{(n+1)}-A_{y;i,j}^{(n+\frac{1}{2})}\right)=&J_{s,y;i,j}^{(n+\frac{1}{2})}\frac{\Delta t}{2}+\frac{\beta_x}{2}\left(A_{y;i+1,j}^{(n+1)}-2A_{y;i,j}^{(n+1)}+A_{y;i-1,j}^{(n+1)}\right)\\&-\frac{\beta_{xy}}{2}\left(A_{x;i,j+1}^{(n+\frac{1}{2})}-A_{x;i,j}^{(n+\frac{1}{2})}-A_{x;i-1,j+1}^{(n+\frac{1}{2})}+A_{x;i-1,j}^{(n+\frac{1}{2})}\right).\end{aligned} \tag{2.96}$$

2.2.3 Fully implicit method

In fully implicit integration procedure, the nonlinear term is implicitly evaluated at time step $(n + 1)$:

$$\begin{aligned}\frac{\psi_{i,j}^{(n+1)}-\psi_{i,j}^{(n)}}{\Delta t}=&\left(\tau_{i,j}-\left|\psi_{i,j}^{(n+1)}\right|^2\right)\psi_{i,j}^{(n+1)}\\&+\frac{U_{x;i,j}^{(n)}\psi_{i+1,j}^{(n+1)}-2\psi_{i,j}^{(n+1)}+U_{x;i-1,j}^{*(n)}\psi_{i-1,j}^{(n+1)}}{\kappa^2h_x^2}\\&+\frac{U_{y;i,j}^{(n)}\psi_{i,j+1}^{(n+1)}-2\psi_{i,j}^{(n+1)}+U_{y;i,j-1}^{*(n)}\psi_{i,j-1}^{(n+1)}}{\kappa^2h_y^2},\end{aligned} \tag{2.97}$$

where we denoted $\tau_{i,j}=1-\gamma_{i,j}$ for clarity.

This equation is solved by a clever modification of the semi-implicit method. This modification is brought about by the approximation

$$N\left(\psi^{n+1}\right)=\tau\psi^{n+1}-\left|\psi^{n+1}\right|^2\psi^{n+1}\approx\frac{1}{\Delta t}\left(S\left(\psi^n\right)-\psi^n\right), \tag{2.98}$$

where S is a nonlinear map,

$$S(\psi)=\frac{\tau^{1/2}\psi}{\left[|\psi|^2+\left(\tau-|\psi|^2\right)\exp(-2\tau\,\Delta t)\right]^{1/2}}. \tag{2.99}$$

(This approximation is explained in Appendix B.) Equation (2.97) now becomes usual semi-implicit equation, the only difference is that coefficients b_m (2.55) now assume more complicated form

$$\boxed{b_m = 1 - \frac{1}{2}\left(\frac{\tau_{i,j}^{1/2}}{\left[\left|\psi_{i,j}^{(n)}\right|^2 + \left(\tau_{i,j} - \left|\psi_{i,j}^{(n)}\right|^2 \right) \exp\left(-2\tau_{i,j}\Delta t\right) \right]^{1/2}} - 1 \right) + \frac{\Delta t}{\kappa^2 h_x^2}} \tag{2.100}$$

The equations for A_x and A_y ((2.81) and (2.82)) are solved again as in the semi-implicit algorithm described in section 2.2.2.

2.2.4 Calculating other variables

Once we complete the timestep using one of the above methods and have new values for ψ and **A**, we can calculate the magnetic field B using (2.79). The magnetization M is obtained from

$$\boxed{M = \frac{\langle B\rangle - H}{4\pi} = \frac{1}{4\pi}\left(\frac{1}{n_x n_y}\sum_{i,j} B_{i,j} - H \right)}, \tag{2.101}$$

where brackets denote averaging over the area of the sample. The electric field **E**

$$\mathbf{E} = -\frac{\partial \mathbf{A}}{\partial t} - \nabla\Phi \tag{2.102}$$

in zero-potential gauge has the following components, according to (2.77) and (2.78):

$$\boxed{E_{x;i,j} = -\frac{1}{\sigma}\left(J_{s,x;i,j} - \frac{B_{i,j} - B_{i,j-1}}{h_y} \right)}, \tag{2.103}$$

$$\boxed{E_{y;i,j} = -\frac{1}{\sigma}\left(J_{s,y;i,j} + \frac{B_{i,j} - B_{i-1,j}}{h_x} \right)}. \tag{2.104}$$

E_y can be integrated along the length of the sample in the y-direction (in the periodic boundary case, when a transport current can be put in the sample) and averaged in the x-direction in order to calculate voltage V and resistance $R = V/I$:

$$\boxed{V = \frac{1}{n_x}\sum_{i=1}^{n_x}\sum_{j=1}^{n_y} E_{y;i,j} h_y}\,. \tag{2.105}$$

The energy functional L is calculated as a sum of condensation, kinetic, and magnetic contributions:

$$L = L_{\text{cond}} + L_{\text{kin}} + L_{\text{magn}}\,, \tag{2.106}$$

$$\boxed{L_{\text{cond}} = \sum_{i,j}\left(-\left(1-\gamma_{i,j}\right)\left|\psi_{i,j}\right|^2 + \frac{1}{2}\left|\psi_{i,j}\right|^4\right) h_x h_y}\,, \tag{2.107}$$

$$\boxed{L_{\text{kin}} = \sum_{i,j}\frac{1}{k^2}\left(\frac{\left|U_{x;i,j}\psi_{i+1,j} - \psi_{i,j}\right|^2}{h_x^2} + \frac{\left|U_{y;i,j}\psi_{i,j+1} - \psi_{i,j}\right|^2}{h_y^2}\right) h_x h_y}\,, \tag{2.108}$$

$$\boxed{L_{\text{magn}} = \sum_{i,j} B_{i,j}^2\, h_x h_y}\,. \tag{2.109}$$

The complete algorithm of the numerical solutions of the TDGL equations in 2D can be found in Appendix C.

2.3 Implementation and Visualization

The algorithm of the numerical solutions of the TDGL equations was coded in C++ programming language on a Windows platform. The code can be found in Appendix C. The code was implemented as a dynamic-link library (DLL) containing the function, which is called by another program, *Model5D* (Figure 8), created by the author to help with the process of data calculation, formatting, saving and visualization. With Model5D, the data (5-dimensional block – 3 dimensions in space, one dimension for multiple variables, and time) is computed by the specific DLL (so-called '*engine*'). The engine is responsible for filling the matrix with values of multiple variables (e.g. Re(ψ), Im(ψ), A_x,

A_y, B, J_x, J_y) at a given time step. This block of data is transferred to Model5D, where it is visualized for controlling the process of calculation, and can be (optionally) saved as a file in one of the predefined file formats. The saved file can later be imported to some advanced scientific visualization software, such as *MATLAB*, to render data as a still picture or an animation.

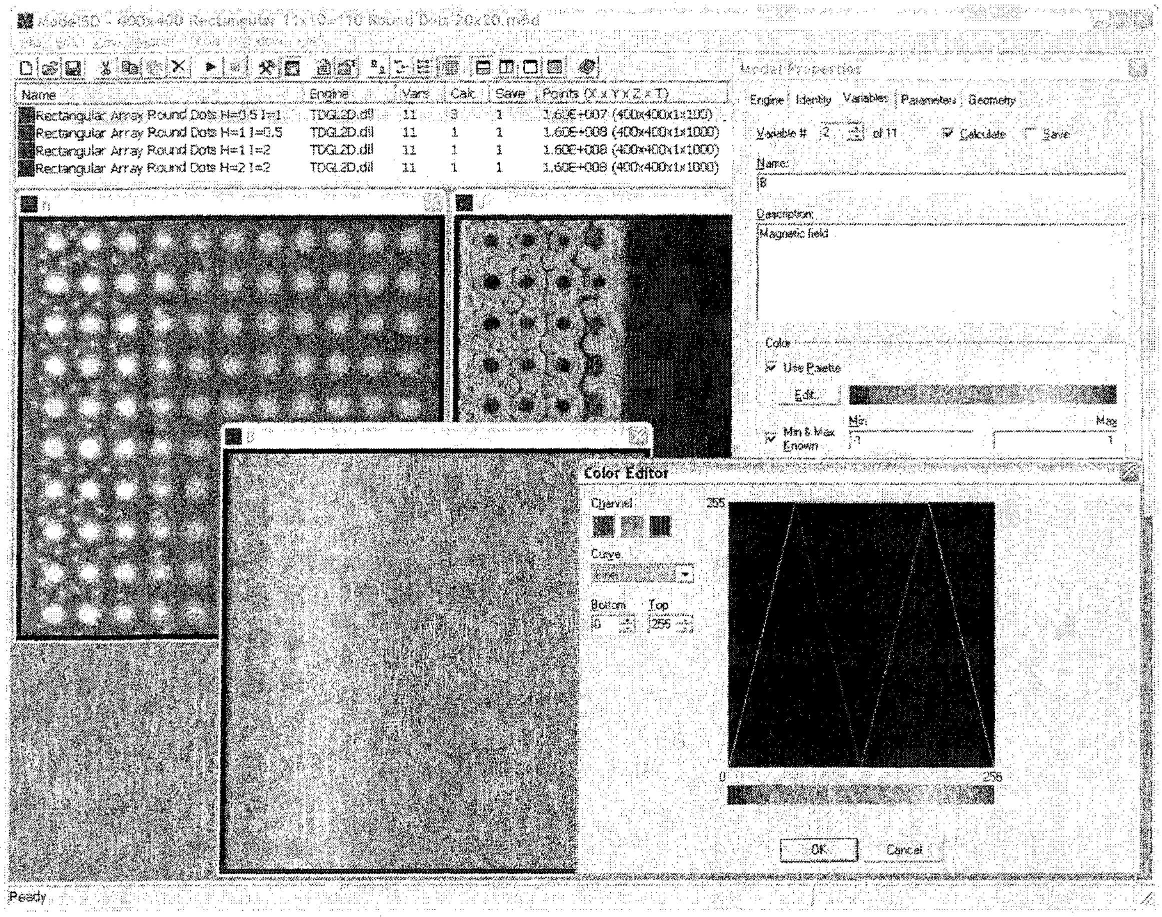

Name	Engine	Vars	Calc	Save	Points (X x Y x Z x T)
Rectangular Array Round Dots H=0.5 I=1	TDGL2D.dll	11	3	1	1.60E+007 (400x400x1x100)
Rectangular Array Round Dots H=1 I=0.5	TDGL2D.dll	11	1	1	1.60E+008 (400x400x1x1000)
Rectangular Array Round Dots H=1 I=2	TDGL2D.dll	11	1	1	1.60E+008 (400x400x1x1000)
Rectangular Array Round Dots H=2 I=2	TDGL2D.dll	11	1	1	1.60E+008 (400x400x1x1000)

Variable # 2 of 11 ☑ Calculate ☐ Save

Name: B

Description: Magnetic field

☑ Use Palette

☑ Min & Max Known Min: -1 Max: 1

Bottom: 0 Top: 255

Figure 8. Model5D screenshot.

The values of parameters of a numerical model and other relevant information, such as descriptions of the parameters and variables, palettes, and dimensions are stored in a *model file*. This information can be viewed and edited through an intuitive graphical user interface. The default values for the parameters are stored in the engine. The engines and models are typically small files (under 100KB) and can easily be exchanged over the Internet.

Typical times of calculation for TDGL model on a 400×400 grid for the time period t = 1,000÷10,000 on a Pentium IV 2.2GHz ranged from several hours to several days. Several PCs were used to perform different calculations simultaneously.

The data was visualized using MATLAB 6.0 software using its scripting programming language. The two-dimensional data resulting from numerical solution of TDGL equations in 2D was visualized as a colored 3D surface, with the value being represented by color and height of the surface above the plane.

The rendered images were saved and later enhanced in Adobe Photoshop or imported to Adobe Premiere to produce animations. These animations can be found on the included CD-ROM.

Chapter 3: Vortex Dynamics in 2D with No Defects

In this chapter we apply the numerical solution of the TDGL equations to study the vortex dynamics in a defect-free sample. We will make a few numerical experiments, starting from very small applied magnetic field and establishing the Meissner state, then gradually increasing the field until vortices begin to enter the sample, observing the transition to equilibrium, and further increasing the magnitude of the field to critical values to observe the destruction of the superconductivity. Furthermore, we will observe the hysteresis in sweeping magnetic field, the effects of the surface barrier, the structure of an isolated vortex, the interaction between vortices, the annihilation of vortices and antivortices, the magnetic field reversal, and the effect of the transport current on vortices.

3.1 Meissner State

When the applied magnetic field is lower that the first critical field H_{c1} (1.35), the Meissner state is established in the superconductor, with the field and currents penetrating the sample only to the penetration depth λ. The purpose of the numerical simulations in this section was to study the distribution of the magnetic field and supercurrent in the sample.

We studied two configurations. The first configuration ('small sample') had the dimensions 4×3 (in units of λ) with the grid 200×150 points. The second configuration ('large sample') had the dimensions 40×30 with the grid 400×300 points. The Ginzburg-Landau parameter was $\kappa = 4$ in both configurations. The applied magnetic field was $H = 0.1 < H_{c1} \approx 0.236$. We integrated the TDGL equations using the semi-implicit method described in Section 2.2.2, with a time step $\Delta t = 0.008$ to the time $t = 8.0$ for the small sample, and $\Delta t = 0.2$, $t = 100.0$ for the large sample. At the final step, both configurations reached the equilibrium Meissner state.

Figure 9 shows the distribution of the magnetic field and supercurrent in the samples. As we see, the magnetic field is shielded only to one half in the center of the small sample, because its size is of the same order as the penetration depth. In contrast, in the large sample, the size of which is much greater than the penetration depth, the magnetic field penetrates the sample only near the edges, to the depth of the order of several penetration depths. The magnetic field in the center of the large sample is millions of times lower than outside the sample. The fallout of the magnetic field inside the sample is exponential, as can be seen from the equidistant powers of 10 contour lines. The streamlines of the supercurrent experience hard turns near 45 degree diagonal lines, which leads to almost rectangular contour lines of the magnetic field. In contrast, in the small sample the streamlines, as well as magnetic field contours, are rounded.

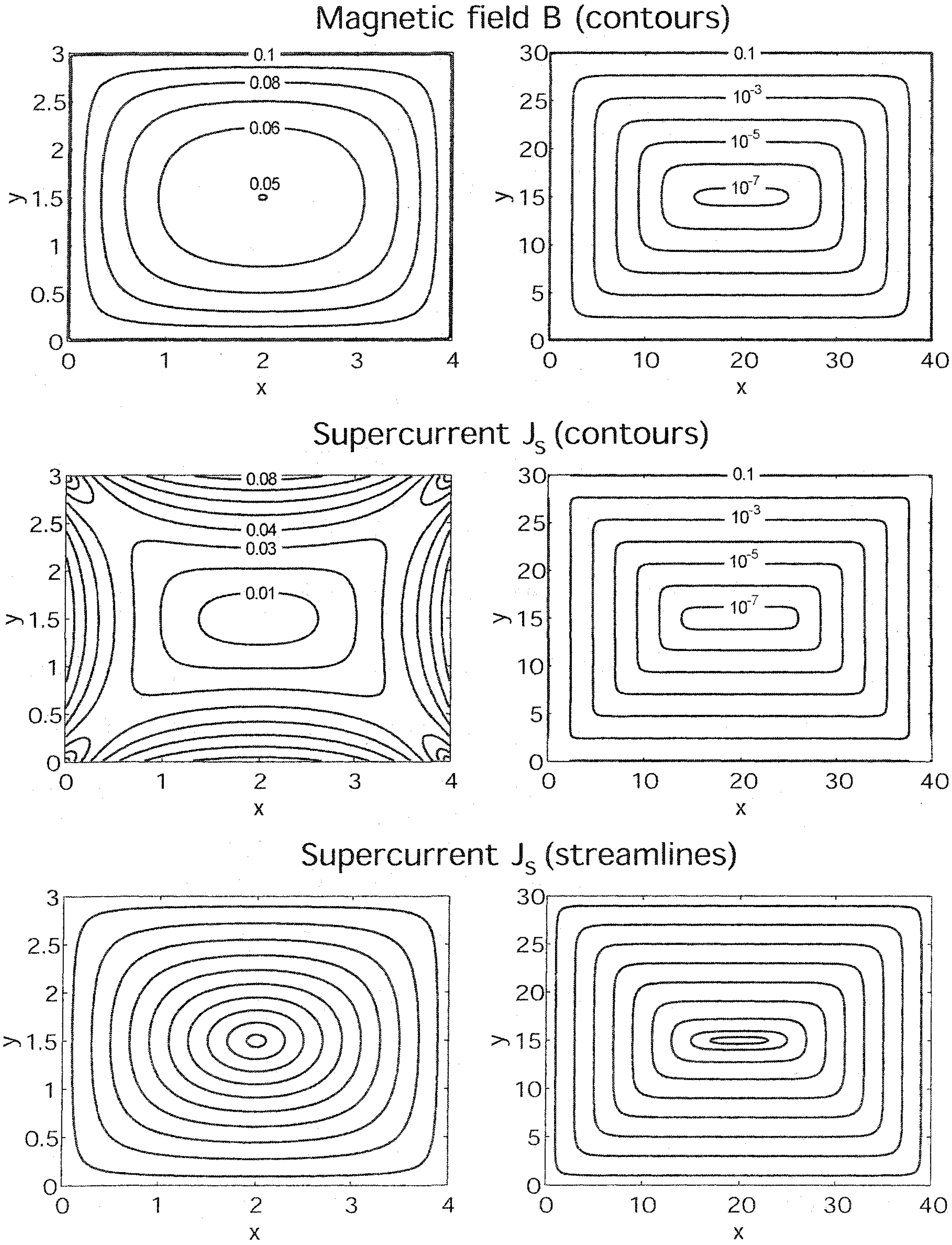

Figure 9. Meissner state in the small (4λ x 3λ, left) and large (40λ x 30λ, right) sample.

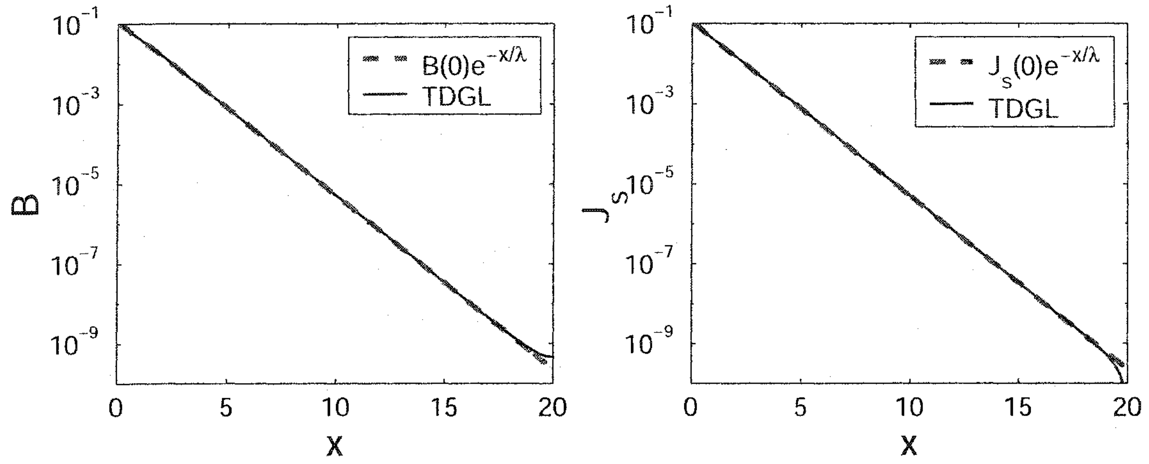

Figure 10. Fallout of the magnetic field (left) and supercurrent (right) in the depth of the large (40λ x 30λ) sample. The solid blue line is the result of the TDGL numerical simulation, while the dashed red line is the London model's result ($B(x) = B(0)e^{-x/\lambda}$). The vertical scale is logarithmic.

To compare the fallout of the magnetic field and supercurrent with the exponential law

$$B(x) = B(0)e^{-x/\lambda},$$

$$J_s(x) = J_s(0)e^{-x/\lambda},$$

additional numerical experiment was carried out. We used the same 'large sample' configuration, as above, but with the periodic boundary in the y-direction, in order to remove the influence of the bottom and top boundaries on the magnetic field distribution in the x-direction. The profiles of the magnetic field and supercurrent along the horizontal line starting at $x = 0$, $y = 15$ and ending at $x = 20$, $y = 15$, are shown in Figure 10. This figure shows an excellent agreement between the result of the Meissner state simulation using TDGL equations with the exponential London law. Only at the center of the sample ($x = 20$) we see the influence of the other side of the sample. The excellent agreement between the theoretical result and numerical simulation is evidence that our numerical model is working well.

3.2 Entrance Patterns

Magneto-optic experiments show a pillow-like pattern for the magnetic field penetrating a pure superconducting sample [18], [19], [20]. The avoidance of the corners by the field has been shown to be primarily an electromagnetic effect [21]. The goal of our numerical simulations was to show that pillow-like patterns are indeed generated by our TDGL model and, furthermore, to analyze the early penetration patterns in more detail.

We studied two samples. A 'small' sample had the dimensions 5×5 (in units of λ), the computational grid had the dimensions 200x200, the Ginzburg-Landau parameter was $\kappa = 10$, the applied magnetic field was $H = 3$ ($\approx 4.243 H_c$), and the TDGL equations were integrated with a time step $\Delta t = 0.01$ to the time $t = 30$. A 'large' sample had the dimensions $40\times 30\lambda$, $\kappa = 4$, 400×300 points, $H = 2$ ($\approx 2.828 H_c$), $\Delta t = 0.2$, $t = 100$. The initial state of both samples was the superconducting state with zero applied magnetic field.

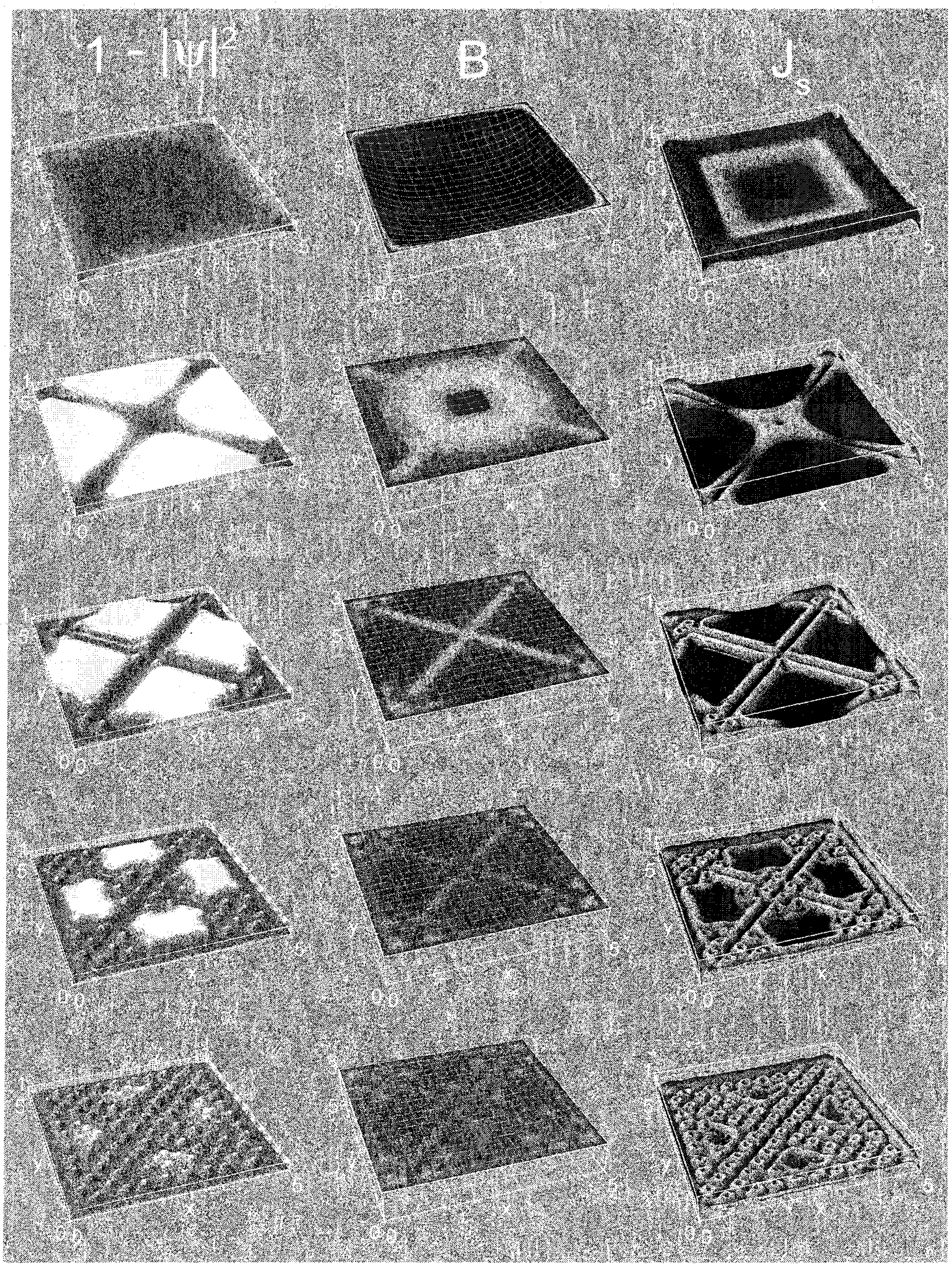

Figure 11. Deposition in the small ($5\lambda\times5\lambda$) sample. Top to bottom: $t = 0.5, 5, 10, 15, 20$.

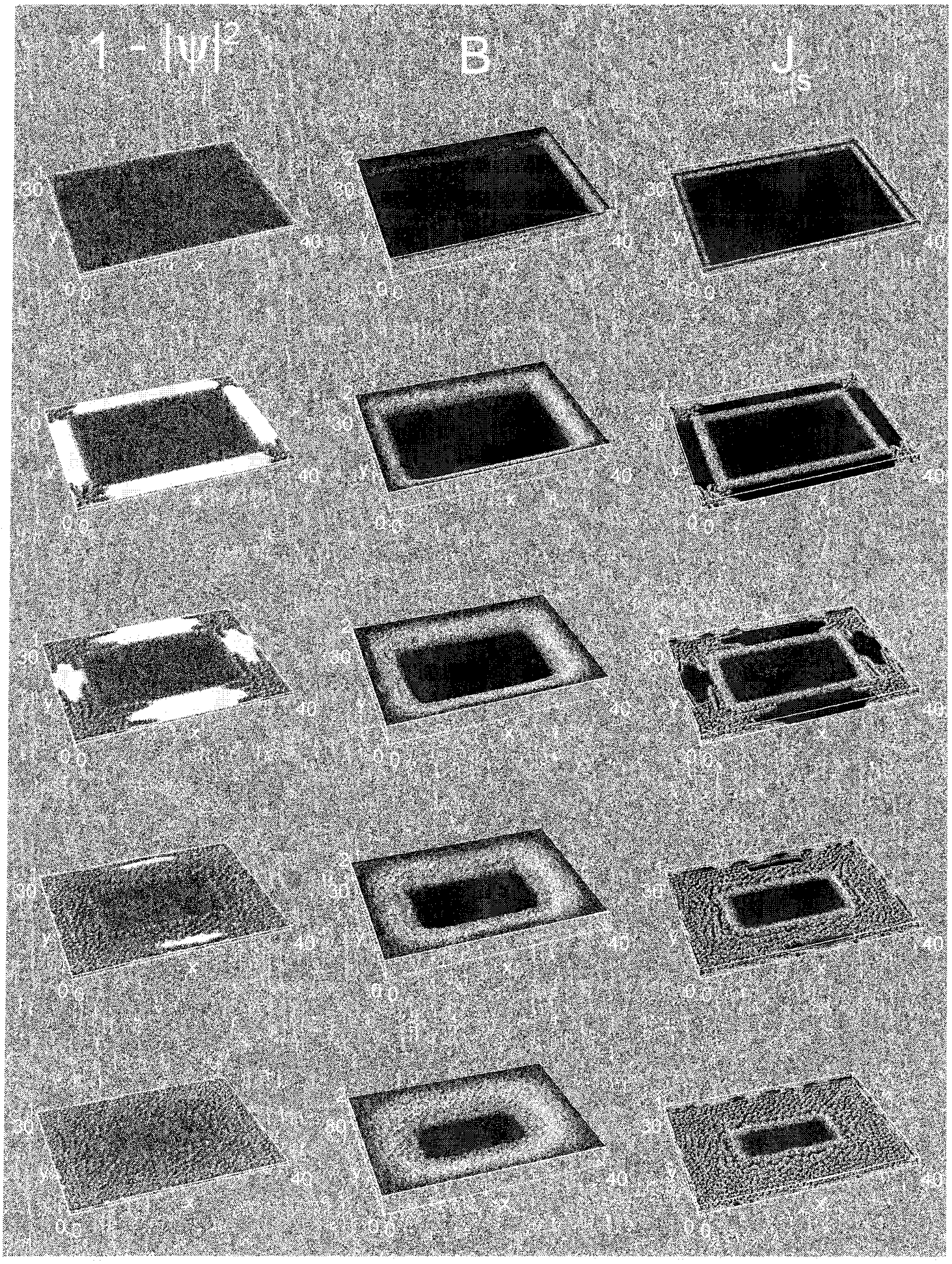

Figure 12. Deposition in the large ($40\lambda\times30\lambda$) sample. Top to bottom: t = 1, 10, 20, 30, 40.

In the small sample, the magnetic field quickly penetrates the whole sample, then goes to equilibrium while the vortices are nucleating in the occupied areas. The characteristic speed of the moving front is of the order λ per unit of time.

In the large sample, there is initially a similar deposition to the distance of several penetration depths into the superconductor. Once the vortices nucleate in this area, they are driven into the bulk of the superconductor by the gradient force, and more vortices are injected from the boundary.

We observe that the phenomenon of deposition occurs in the area of large gradient of magnetic field, where the current density reaches the critical level and triggers the temporary transition from the superconducting to normal state.

The flux entry patterns generated by our TDGL model are in agreement with the data from magneto-optic experiments, which show a pillow-like pattern for the magnetic field penetrating a superconducting sample (Figure 13). The avoidance of the corners by the field has been shown to be primarily an electromagnetic effect. The formation of the pillow pattern is not simply due to the field penetrating only on the sides. The field first penetrates everywhere in small samples and is subsequently excluded from the diagonals. Large samples exhibit similar phenomenon during the same period of several units of time in dimensionless units.

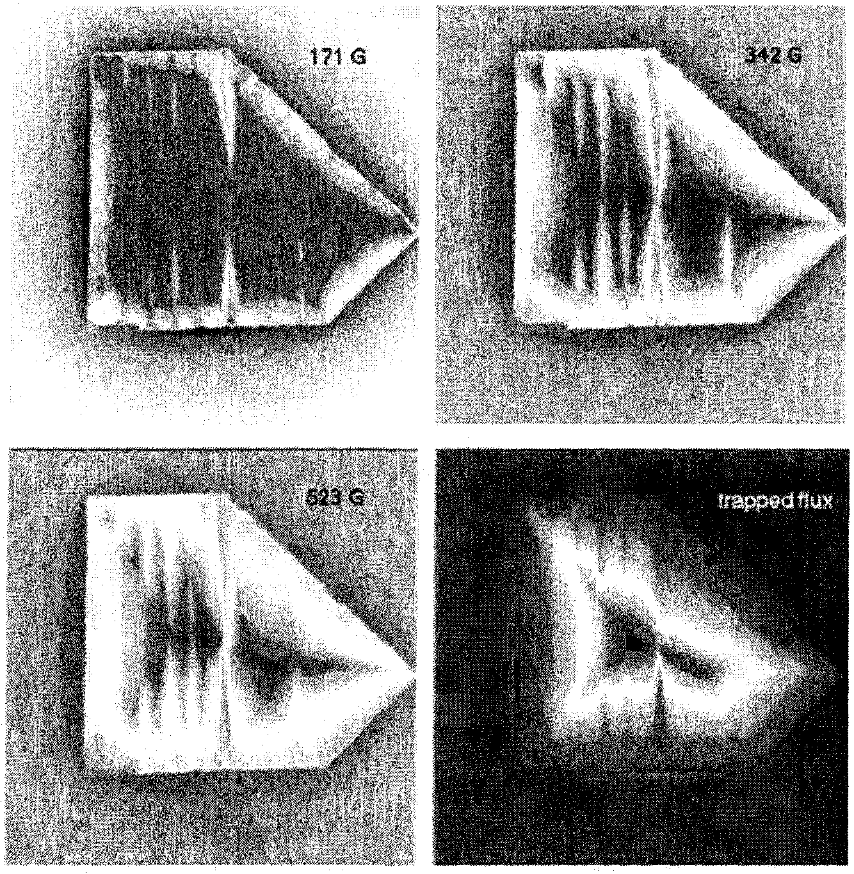

Figure 13. Patterns of the magnetic flux at 40 K for various increasing fields and trapped flux following application of 855 G in a crystal of YBaCuO.

3.3 Equilibrium Lattice

When there is no transport current in the system and the applied field is constant, the solution of the Ginzburg-Landau equations tends to be an equilibrium state. We examine two equilibrium configurations – ideal triangular lattice, and a lattice with stable defects. We also observe the sudden transitions from one symmetry to another when the geometry of the sample strongly influences the symmetry of the vortex lattice.

3.3.1 Ideal triangular lattice

The sample used in this simulation measures 128ξ in the transverse (x) direction and is periodical in (y) direction with the period 192ξ. The Ginzburg-Landau parameter $\kappa = 16$. The computational grid has a mesh width $h = 1/2\xi$, for a total of 256×384 vertices. The timestep is $dt = 0.1$. The applied field is uniform, $H_L = H_R = H = 0.5$. For the initial period of time of $t = 100$ units, a stronger field $H = 2$ is applied so that to overcome the surface barrier (see Section 3.5) and pump the vortices into the bulk of the sample. After $t = 100$, the field is lowered to $H = 0.5$ and the configuration is let to relax to equilibrium.

Equilibrium was reached after $t = 100000$, when the number of vortices remained constant and the vortex positions varied less than 10^{-6} in units of ξ. The equilibrium vortex configuration had 117 (=9×13) vortices arranged in a hexagonal pattern; see Figure 14.

It is worth noting that according to (1.16) and (1.36), the flux quantum in dimensionless units (when length is measured in units of ξ) is equal to $\Phi_0 = 2\pi\kappa$. The number of vortices in equilibrium is such as to make the magnetic flux per vortex equal to the flux quantum. In this particular example, the theoretical number of vortices based on a simple estimate [total flux]/[flux quantum] is equal to 122, vs. 117 observed. The difference is due to areas near the boundaries which trap some additional flux, but fail to form vortices due to the surface barrier.

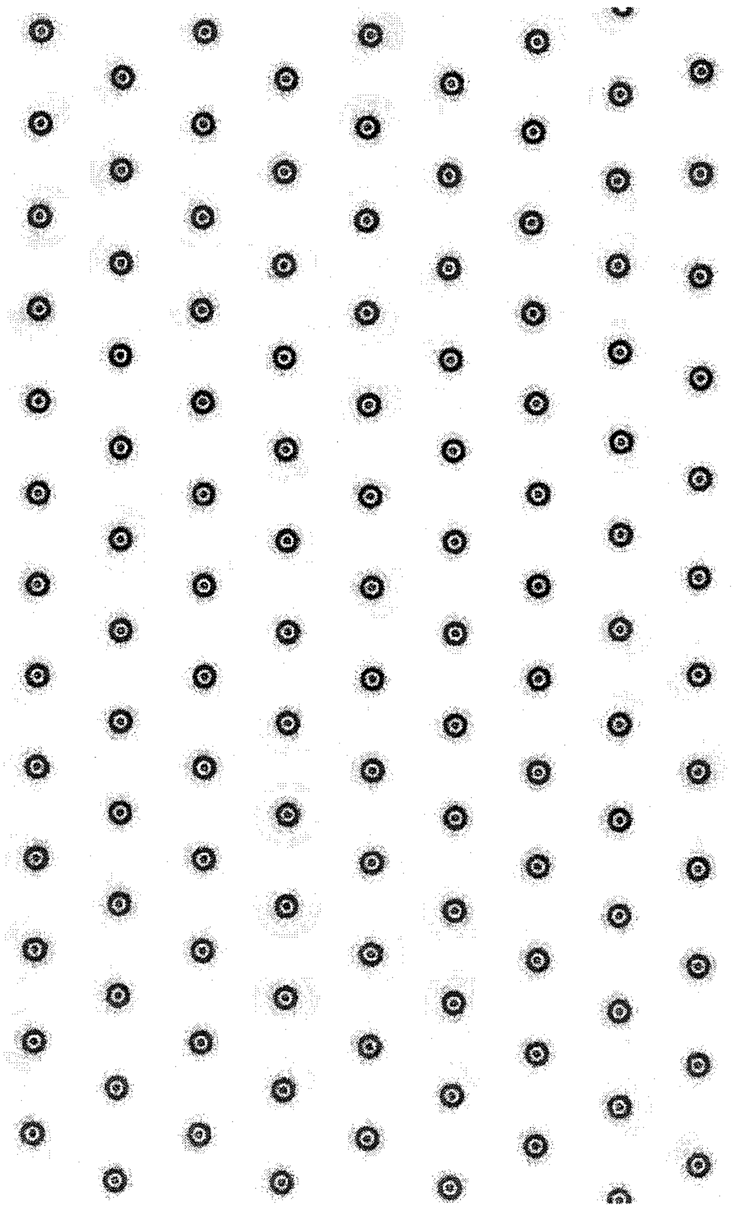

Figure 14. Ideal triangular vortex lattice.

3.3.2 Triangular lattice with defects

Given the dimensions and the Ginzburg-Landau parameter κ, there are only a few discrete values of the applied magnetic field (or rather, a few discrete ranges – due to the effects of the surface barrier) which give rise to ideal triangular vortex lattices. Most of the time, the magnitude of the magnetic field is somewhere in between these discrete values (or ranges). When the magnetic field is higher than what the previous stable ideal lattice configuration can bear, some vortices have to find their home inside the close-packed lattice, pushing the neighbors away, thus creating lattice defects – vacancies, interstitials, and dislocations.

We locate the vortex core positions by finding the local minima of the order parameter. Having found the position of each vortex, we use a Delaunay triangulation [25] to analyze the structure of the vortex lattice. Each vortex in the bulk with fewer or more than six neighbors identifies a defect in the lattice.

Figure 15 shows an evolution of lattice defects with time. A superconductor with dimensions 160x160ξ is periodic in y-direction and has $\kappa = 4$. The applied magnetic field $H = 2$ and the computation grid has 200x200 points. The system was integrated to $t = 10^6$ – to stable configuration – with the timestep $t = 0.3$, which took about 5 days to finish on a Pentium IV 1.13GHz computer. The triangles are colored according to maximum difference of its angles from 60 degrees: the more the triangle is distorted compared to equilatteral triangle, the denser the color is.

As one would expect, the lattice has most defects at early stages of the transition to equilibrium, although the equilibrium number of vortices is already present in the superconductor (about 2000). The large number of defects creates gradient forces in the bulk, which drive vortices into configurations with ever lower and lower total energy. When a configuration with the local minimum of energy is formed, the lattice becomes static, with the defects frozen in it. Another run of the same initial configuration would lead to a different stable pattern of defects, due to many degrees of freedom of the system and small rounding errors.

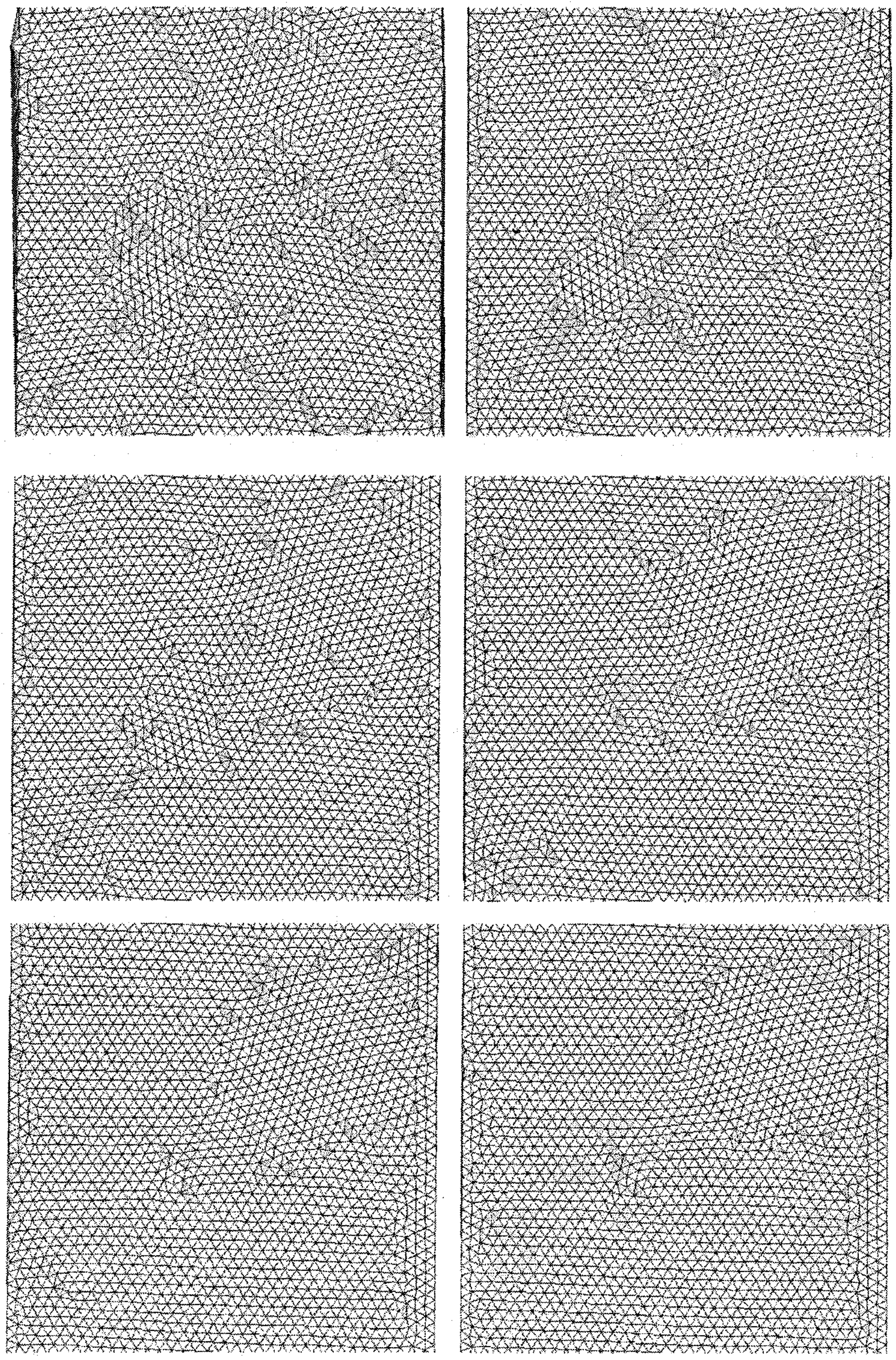

Figure 15. Evolution of the vortex lattice with defects. t = 1000, 2000, 5000, 10000, 50000, 1000000 left to right, top to bottom.

3.3.3 Symmetry breaking

When only a small number of vortices is induced in the superconductor due to its small size, an interesting phenomenon of "symmetry breaking" may occur. In the process of flux entry, a metastable state may initially be reached, whose symmetry properties are different from those of the final equilibrium state. Therefore, a certain caution should be exercised when judging whether or not the system reached the equilibrium.

Figure 16 shows such an example. A seemingly stable configuration with 16 vortices is reached at $t = 100$ in a superconductor with dimensions 32x32ξ, $k = 4$ and $H = 1$. This configuration has 180-degree rotational symmetry. However, at $t = 150$ it suddenly "changes mind" and starts to reconfigure itself, until it settles on a perfect 4x4 square lattice, dictated by the sample's symmetry.

Figure 17 shows an opposite transition at $H = 0.87$. At $t = 50$, a quasi-equilibrium 90-degree rotational symmetry is achieved, with 12 vortices in the sample. However, at $t = 200$ vortices start to move and rearrange themselves into 180-degree symmetry.

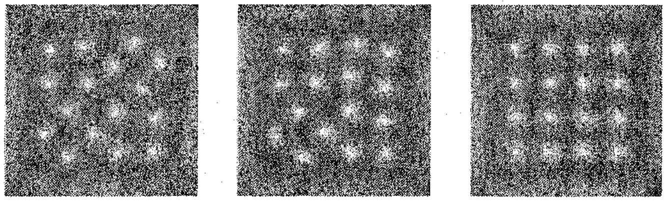

Figure 16. 180-degree to 90-degree symmetry breaking.

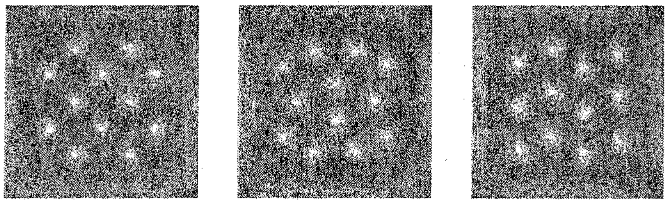

Figure 17. 90-degree to 180-degree symmetry breaking.

3.4 Field Sweep

Now that we observed the entrance of vortices and the equilibrium lattice, we will study the effects of ever increasing magnetic field. We will gradually increase the magnetic field from 0 until the superconductivity is destroyed completely throughout the sample. At each value of the magnetic field, we let the vortices enter and the lattice reach an equilibrium. We will plot the magnetization and number of vortices as a function of applied magnetic field. The sample is infinite in z and bounded in x and y, with the dimensions of 100ξx100ξ and computational mesh of 400x400 points. The Ginzburg-Landau parameter is $\kappa = 10$.

3.4.1 From 0 to H_{c1} to H_{c2} to H_{c3} to H_{c4}

In this simulation, the magnetic field has been linearly increasing from $H = 0$ to $H = 20$ during 5000 units of time.

According to (1.35), the vortices should enter the superconductor at $H_{c1} = 0.14$. However, this happens much later, at about $H_c = 0.707$ (1.34). This is due to the free surface, which creates a potential barrier for vortices entering or leaving the superconductor. Bean and Livingston [26] (see also Abrikosov's book [13]) estimated that the barrier vanishes only at

$$H_{c1\,\mathrm{surf}} \approx H_c, \tag{3.1}$$

which is in excellent agreement with our numerical simulation. We discuss surface barrier in more detail in Section 3.5 below.

At $H_{c2} = 10$ the superconductivity is destroyed completely in the bulk of the sample. However, there still remains a sheath of supercurrent near the surface. The thickness of this sheath is roughly one coherence length ξ. The field at which the sheath is suppressed is [27]

$$H_{c3} = 1.7H_{c2}, \tag{3.2}$$

which is again in excellent agreement with our numerical simulation.

For the superconductor periodic in one direction, H_{c3} destroys the superconductivity completely throughout the sample. As a peculiar, but obviously not very practical phenomenon, we observe that in non-periodic sample there remain pockets of superconductivity of size $\sim\xi$ at the corners even at fields higher than H_{c3}. One can call the field at which the superconductivity is destroyed even in the corners, H_{c4}. From our simulation, we estimate that

$$H_{c4} \approx 2H_{c2}. \tag{3.3}$$

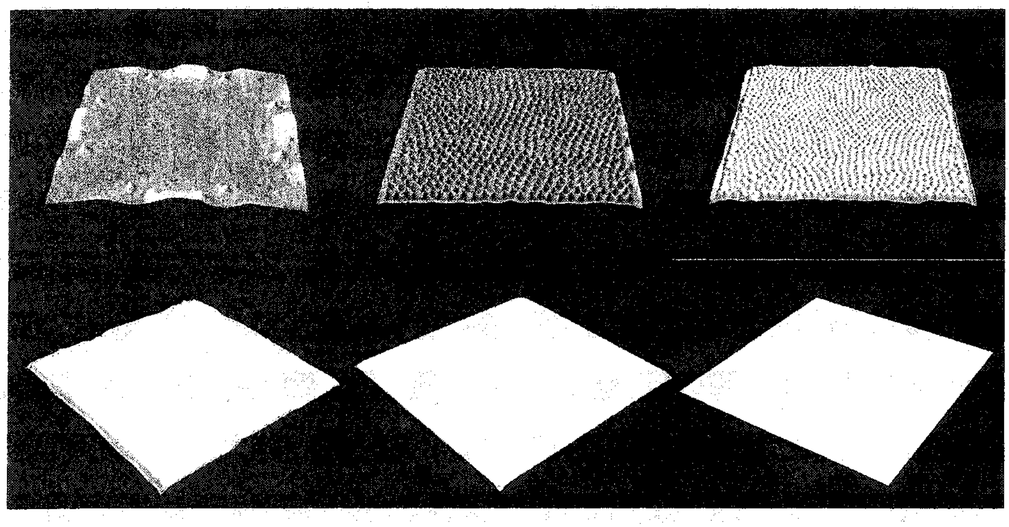

$1-|\psi|^2$

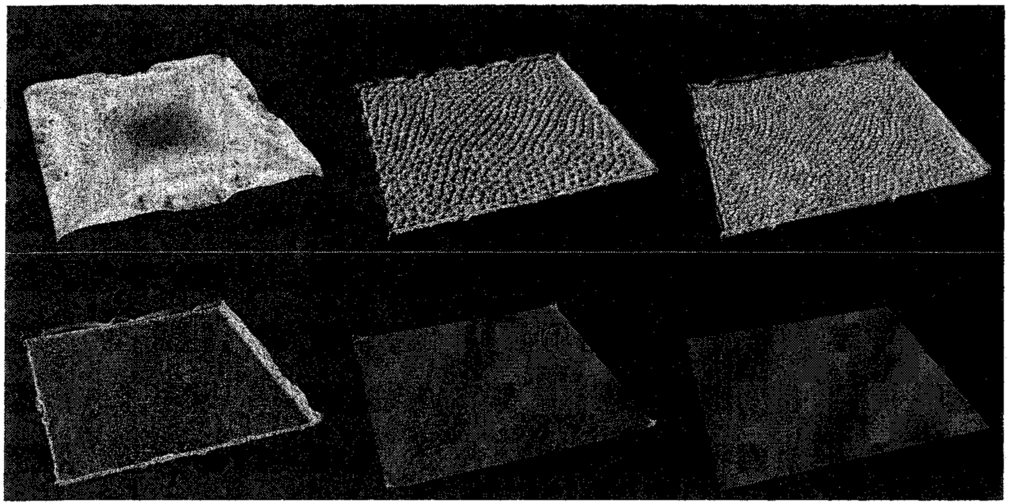

J_s

Figure 18. Profiles of the order parameter (top) and supercurrent (bottom) in increasing magnetic field. H=0.71 (=$H_{c1\mathrm{surf}}$), 5, 8, 10 (=H_{c2}), 17 (=H_{c3}), 20 (=H_{c4}) (left to right, top to bottom).

3.4.2 Hysteresis

The sample studied in this section is a $160\xi\times160\xi$ square with $\kappa=4$. The magnetic field is swept linearly from 0 to 8.5, then from 8.5 to –8.5, and finally from –8.5 to 8.5. This sweep is done either slowly (in 20000 units of time for the whole cycle), or rapidly (in 5000 units of time). The magnetization ***M*** (2.101) of the sample is measured. The results are shown in Figure 19.

When a magnetic field is applied to a superconductor in the Meissner state, its magnetization increases linearly, as the superconductor expels the field from the bulk completely. A small deviation from the linear law is due to the fact that the screening currents flow within the London penetration depth λ of the surface. When the surface barrier is overcome, vortices enter the bulk and magnetization is decreased. When the magnetic field is swept back, not all vortices manage to escape the sample synchronously with the field, so that even in zero applied field there are some vortices remaining trapped within the sample. As the magnetic field becomes negative, antivortices enter the sample and annihilate with the trapped vortices, finally overpower them and turning the magnetization negative.

As can be seen from hysteresis curves, the faster the changes in applied field are, the greater the dissipation of energy (the area inside the hysteresis curve) is.

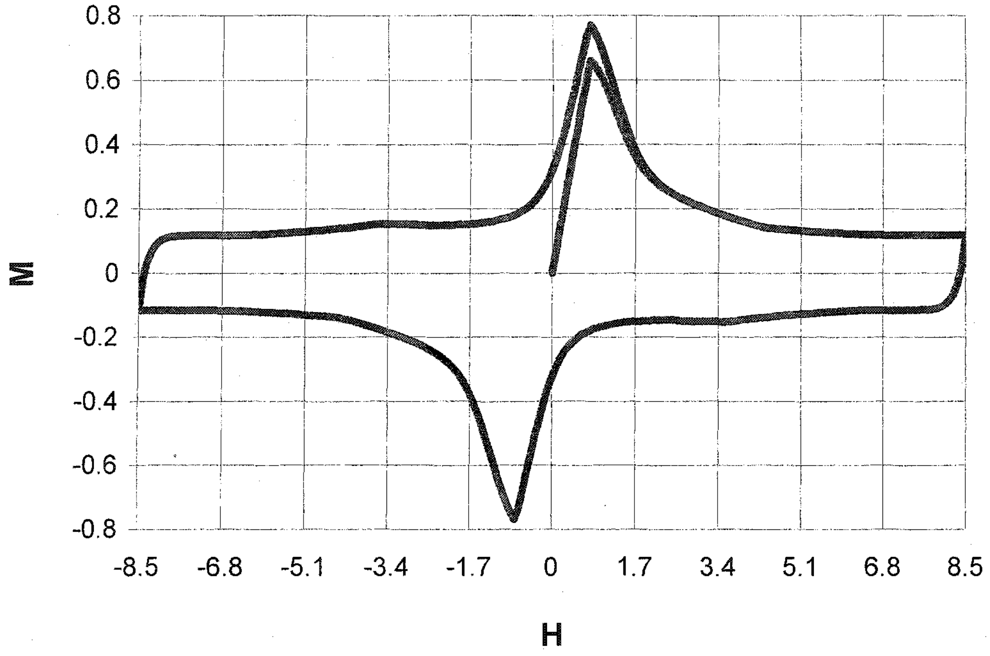

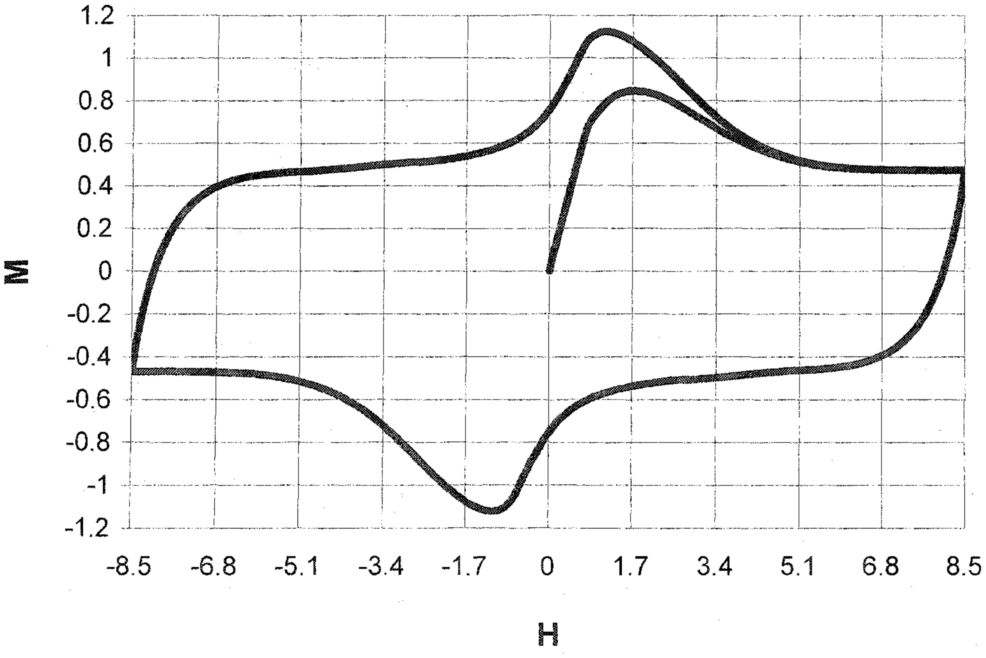

Figure 19. Magnetization *M* as a function of applied magnetic field *H*. Top: slowly changing field ($dH/dt = 0.0021$). Bottom: rapidly changing field ($dH/dt = 0.0085$).

3.5 Surface Barrier

As we have seen, the surface barrier plays a significant role in both vortex dynamics and equilibrium configurations. While the surface barrier is quite an obstacle in numerical simulations, which does not allow one to study the behavior of the superconductor between H_{c1} and H_c, in real life the surface barrier is significantly lowered by the imperfections of the sample's surface. These imperfections serve as nucleation spots for vortices, making the entrance into the bulk easier. For example, if there is a crack on the surface, the vortices are first formed on the edge of the crack so that they are far enough from their mirror-like antivortex "images", which attract real vortices and give rise to surface barrier.

3.5.1 Lowering the surface barrier

We can imitate the surface imperfections to lower the barrier by making use of the "defect strength" parameter γ in modified Ginzburg-Landau equation (see Section 1.3.6). By making a region of $\gamma = 1$ in the needle-like region of the sample, we give vortices a "back door" for easy entrance, thus making possible for vortices to enter the bulk at H_{c1}, not H_c as in a defect-free superconductor. Figure 20 shows an example of a single-vortex initiator.

3.5.2 Single vortex generator

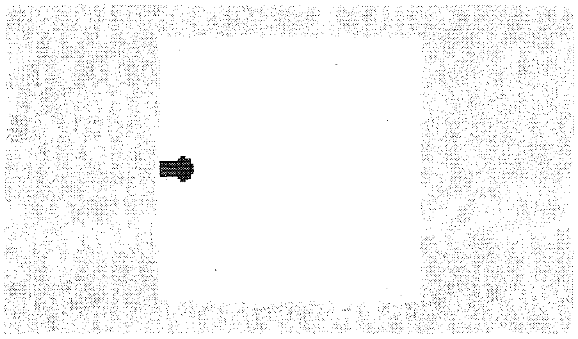

Figure 20. Single-vortex initiator.

Figure 21 shows the single vortex generator in action in the sample with dimensions 80×80ξ, $\kappa = 4$, $H = 0.5$, at times $t = 4$, 8, 12, and 5000.

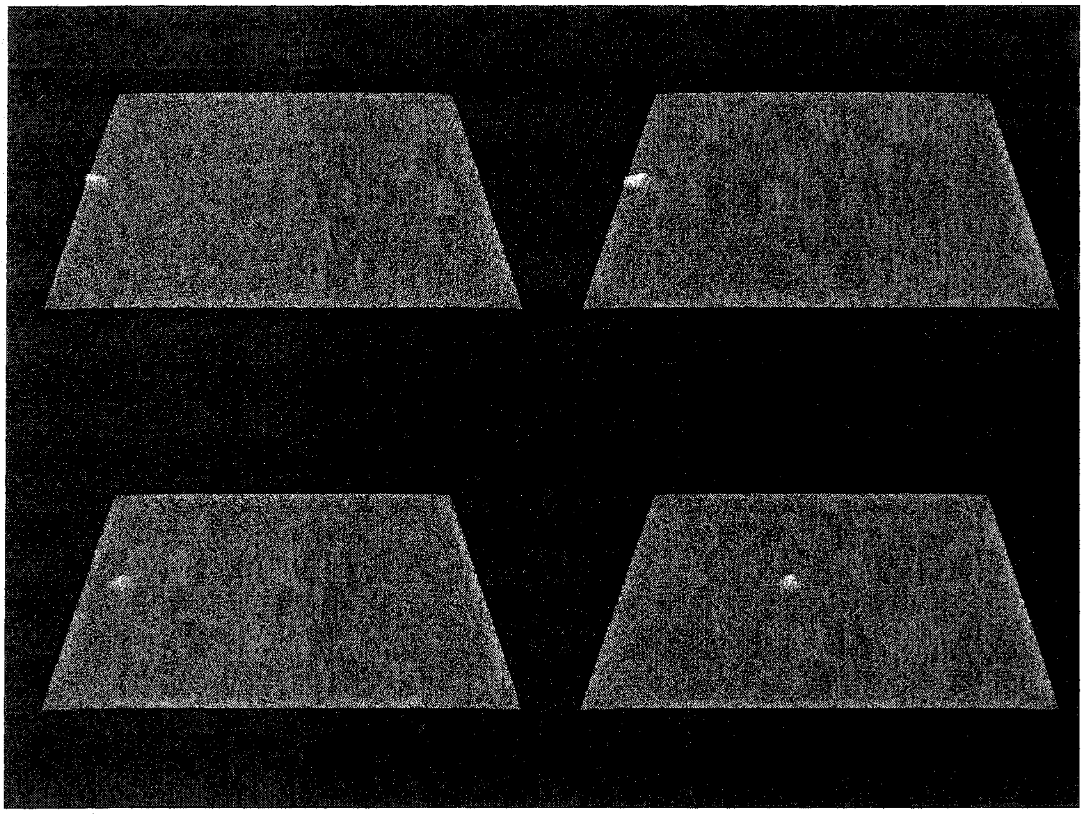

Figure 21. Single vortex generator in action.

3.6 Single Vortex

Using the vortex generator allows us to isolate a single vortex in the bulk of the sample and study its properties – something not currently possible to do in a real life experiment.

Figure 22 shows the magnetic field B and order parameter ψ as functions of radial distance r in a vortex. At first glance, we see that the coherence length ξ (one in our dimensionless units) is the characteristic distance for variations in the order parameter; whenever $|\psi|$ is varying in space its value changes significantly over distances of order ξ. On the other hand, the London penetration depth λ is the characteristic distance for variations in the magnetic field.

In his pioneering work, Abrikosov [5] showed that the exact solution for the magnetic field is given by

$$H(r)=\frac{1}{\kappa}K_0(r), \tag{3.4}$$

where K_0 is McDonald function, H and r are in dimensionless units. In the vortex center, the value of magnetic field is given by approximate formula

$$H(0)\approx\frac{1}{\kappa}(\ln\kappa-0.18), \tag{3.5}$$

which in our case gives H(0)=0.3 – a value very close to the one observed in the numerical calculation.

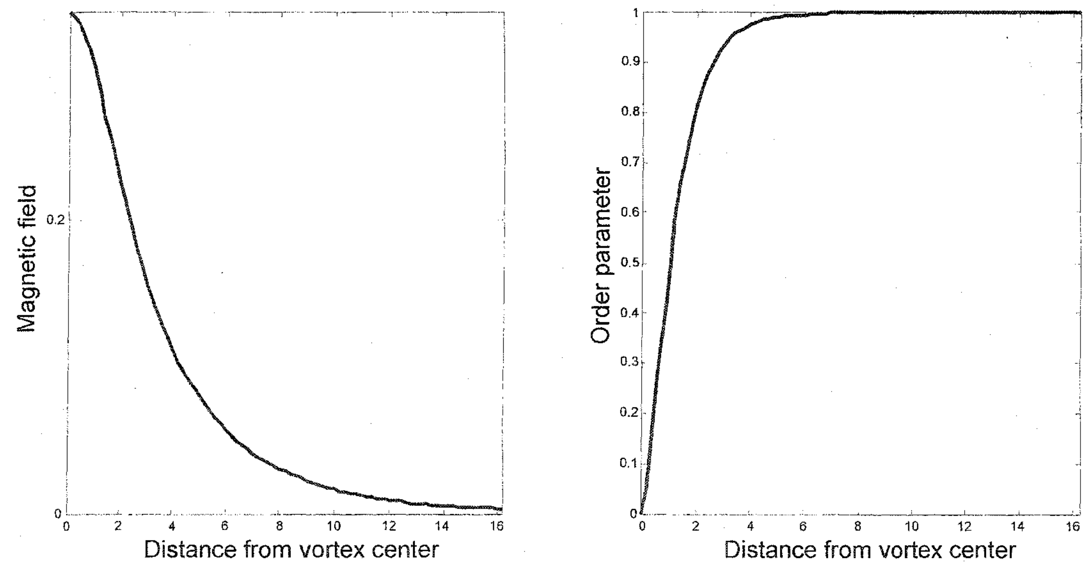

Figure 22. Magnetic field B and order parameter ψ as functions of radial distance r in an Abrikosov vortex. κ=4, H=0.5

3.7 Vortex-Antivortex Annihilation

An interesting phenomenon occurs when an opposite polarity magnetic field is applied to the sides of the periodic sample. Vortices and antivortices enter the superconductor and meet in the bulk, annihilating with each other. This is demonstrated in Figure 23 where the superconductor is periodic in y-direction and has dimensions of $40\times40\xi$, $\kappa = 4$, and magnetic field on the left surface is $H = 0.5$, while on the right surface it is $H = -0.5$. Vortices are generated one by one by initiators (defects on the surface).

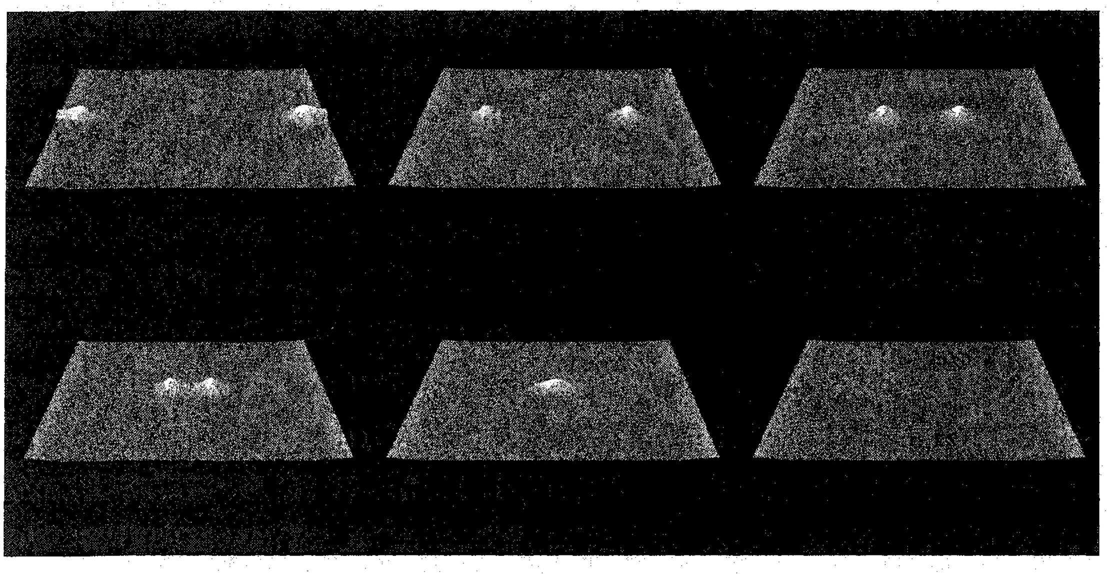

Figure 23. Vortex-antivortex annihilation. t=6.4, 18.4, 38.4, 46.4, 48, 48.4.

Note how quickly (in time of the order 1) the annihilation occurs. Since 1 is the characteristic diffusion time for distances of the order 1 (that is, ξ), this result seems quite natural.

3.8 Magnetic Field Reversal

The purpose of the next simulation was to study the interface between the regions of opposite magnetic polarity. Magnetic flux vortices of opposite polarity attract and annihilate each other, so when the direction of the applied field is reversed, vortices of opposite polarity enter the sample and annihilate existing vortices. Experiments indicate an irregular interface between the regions of opposite polarity [28]. The roughness is caused by a thermodynamic instability; since the domain interface has negative surface energy in type-II superconductor, it is unstable. As its surface increases, the interface tends to break up and spawn regions of one polarity enclosed by regions of the opposite polarity.

In our simulation, we used the superconductor of dimensions $160\times160\xi$, $\kappa = 4$. We first established an equilibrium number of vortices for the applied magnetic field $H = 2$. Subsequently, we reversed the orientation of the applied field to $H = -2$. Figure 24 gives a few snapshots of the order parameter at different moments of time as the vortices annihilate. We clearly observe that the rough and inclusive nature of the polarity interface is an intrinsic feature of the Ginzburg-Landau model. Consequently, it is not necessary to use specially designed fluid models to account for the rough interfaces observed in magneto-optical experiments.

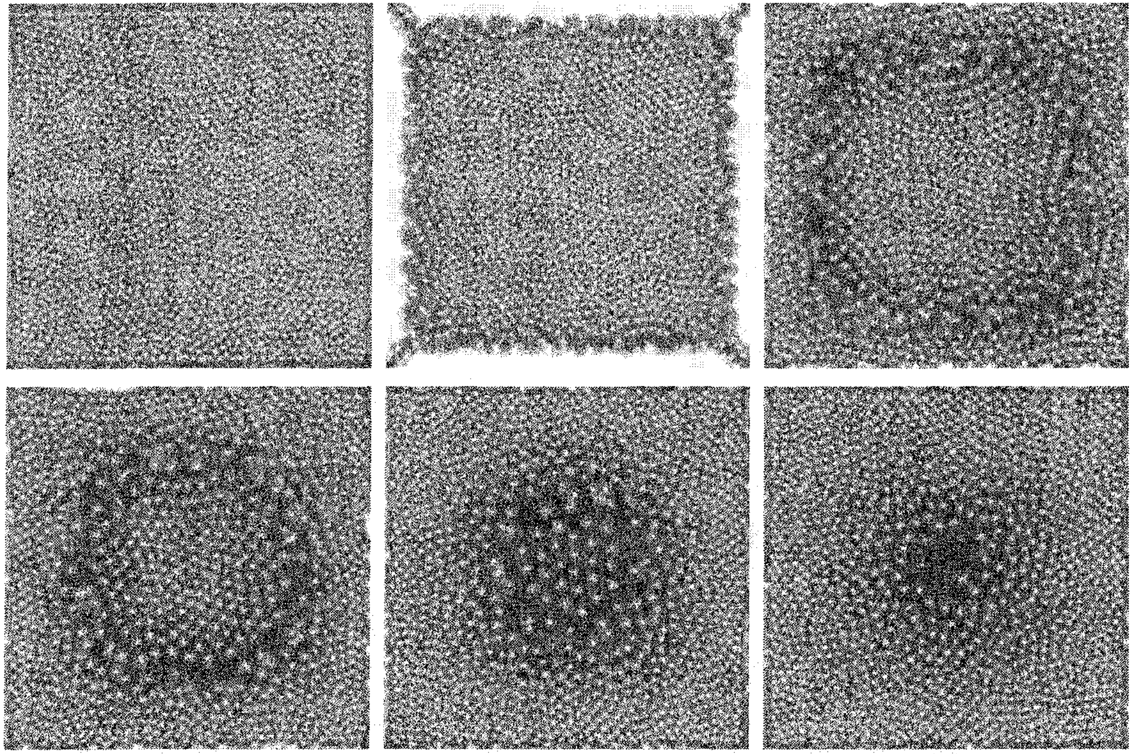

Figure 24. Order parameter in magnetic field reversal experiment at timesteps 0, 4, 21, 43, 72, 96 (with timestep equal to *dt*=2) after reversing the applied field from *H*=2 to *H*=-2.

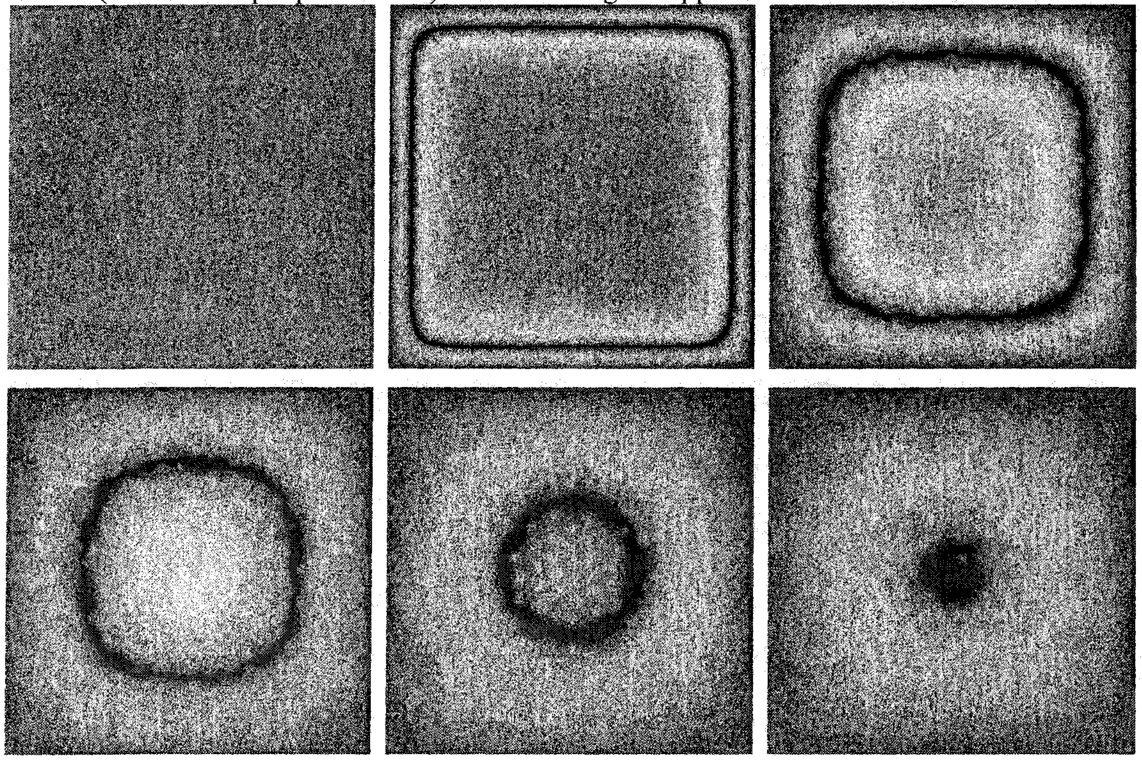

Figure 25. Magnetic field in the same conditions as in Figure 24. The black represents areas where the field is essentially zero.

3.9 Transport Current

In the last ten years, attention has focused increasingly on the dynamic states of a vortex system. Much of the interest concerns the type of motion a vortex lattice experiences under an applied current [29]-[31]. It has been observed that, in a significant region of the phase diagram below the vortex lattice melting line, vortex motion is predominantly plastic motion. The explanation given in [29], [30] relies heavily on the notion that the vortex interactions compete with a randomness in the driven vortex system [32], [33]. In this section, we present the results of a numerical study of the motion of a vortex lattice in a clean finite sample and find a different mechanism for plastic vortex motion. Past considerations excluded the effects of the current-induced magnetic field. We show that a current increases the vortex spacing in the direction of vortex motion and enforces the formation of fault lines to accommodate the resulting strains. The fault lines serve as a source of plastic deformations. The mechanism is the result of the intrinsic behavior of the vortex lattice and is independent of bulk pinning. It may be responsible for plastic motion in very clean superconductors.

The structure of a vortex lattice moving under the influence of a transport current in a homogeneous superconducting sample depends on the relative strengths of the Lorentz force and the barrier forces associated with the free surfaces [11]. Numerical solutions of the time-dependent Ginzburg-Landau equations [7], [8] show that the barrier forces dominate at weak currents. Vortex motion is confined to the interior of the sample, and the vortex lattice is essentially static. Its close-packed rows align with the free surfaces. The lattice structure may have defects, whose origin can be traced to the transient phase, but these defects disappear gradually, and a more or less uniform structure with isolated defects remains. When the Lorentz force dominates, vortices enter and leave through the free surfaces, and the entire vortex lattice moves steadily. The lattice structure changes in two ways. We see a change in the orientation of the lattice, where the close-packed rows align with the direction of the Lorentz force, and the development of a defect superstructure, where one or several distinct "fault lines" separate regions of approximately uniform structure. A fault line consists of several aligned dislocations and finite segments of a 30° boundary. The fault lines remain more or less stationary as the lattice moves. They provide the principal mechanism supporting the vortex density gradient induced by the self-field of the current and serve as a source of plastic deformations. Similar defect structures have been observed in decorations of static vortex lattices with density gradients [35].

The computations were done for a rectangular homogeneous pin-free superconducting sample, infinite in z, periodic in y, and bounded in x, with the cross section $32\xi\times48\xi$ in the (x, y) plane and Ginzburg-Landau parameter $\kappa=4$. A transport current J in the positive y direction is induced by a field differential between the free surfaces: $H_l = H_0 + \Delta H$, $H_r = \mathrm{H}_0 - \Delta H$, where $\Delta H = ½J$. The resulting Lorentz force acts in the positive x direction. The applied magnetic field is $\mathrm{H}_0 = 0.8$ and $\Delta H = 0$ (no current), 0.125 ("weak" current), 0.25 ("intermediate" current), or 0.5 ("strong" current). The corresponding current densities are approximately 0, 2, 4, and 8% of the BCS depairing-current density.

Starting from the Meissner state, we increase the applied field to $\mathrm{H}_0 = 0.8$, apply the transport current as appropriate, and let the system evolve through the transient phase before we begin recording data. The average number of vortices in the steady state varies from 230 (no current) to 660 (strong current). The structure and evolution of the vortex lattice are analyzed by means of a Delauney triangulation, which is constructed at each recorded time step. Each vortex in the bulk with fewer or more than six neighbors is identified with a defect in the lattice. The computational results are shown on Figure 26.

In the absence of a transport current, 230 vortices enter the sample to form a dilute vortex structure with an average lattice spacing $a_0 = 2.58\lambda$. The average magnetic induction in the sample is $B = 0.27$, considerably less than the applied field $H_0 = 0{:}8$. The lattice is static. Its structure remains defective; the major types of defects are isolated dislocations (pairs of defects – one with five, the other with seven neighbors) and finite segments of 30° boundaries (strings of three or more contiguous dislocations). The vortex region is separated from the free surfaces by a vortex-free region, 2.1λ wide. The Meissner current flows entirely within these vortex-free regions.

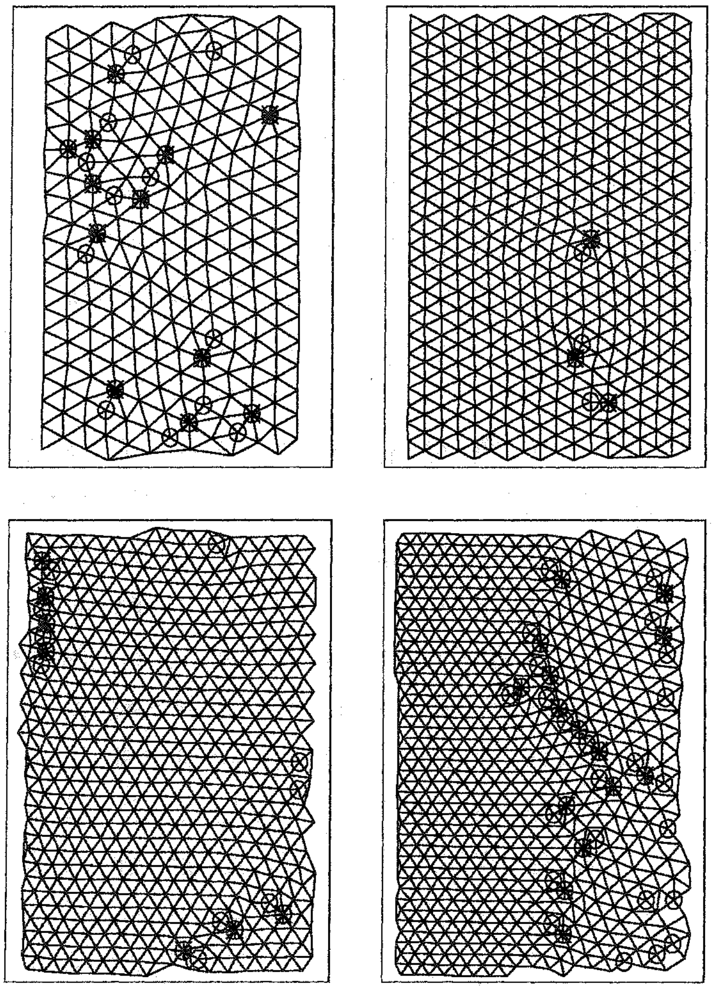

Figure 26. Lattice structure in $32\xi\times48\xi$ sample, $H_0 = 0.8$; lattice defects are marked. Top left: no current, top right: weak current ($\Delta H = 0.125$), bottom left: intermediate current ($\Delta H = 0.25$), bottom right: strong current ($\Delta H = 0.5$).

A weak current ($\Delta H = 0.125$) almost doubles the average number of vortices to 459. The vortices form an almost ideal crystal structure, with $a_0 = 1.88\lambda$. The lattice is again static, but slightly displaced to the right edge. The supercurrent density at the left edge of the sample is approximately equal to the BCS depairing-current density. The close-packed direction of the lattice is again aligned with the free surfaces. The remaining defects are the remnants of a misoriented grain in the center of the sample, whose origin goes back to the transient phase and which gradually heals during the recording period.

At the intermediate current ($\Delta H = 0.25$), the surface barrier at the right edge is broken, and the lattice moves steadily in the positive x direction. At the left edge, vortices penetrate into the sample in a highly organized manner: A penetrating vortex triggers successive nucleations, which propagate along the surface of the sample in the direction of the current ("zipper" penetration). Vortices exit through the right surface, where the vortex-free region has disappeared completely. The average number of vortices in the sample increases to approximately 565; this number oscillates in time, but the amplitude of the oscillation is always less than 1%. The close-packed direction of the moving lattice is oriented along the direction of motion. A reorientation of a moving vortex lattice was observed in early experiments [36] and, more recently, in YBCO [37]. A mechanism for the reorientation in the presence of bulk pinning was proposed in the context of collective pinning theory in [10]. Our investigation indicates that the reorientation also can be caused by the free surfaces of the sample. Approximately one third of the transport current now flows in the interior the sample, supporting the steady motion of the lattice. The resulting small gradient in the vortex density leads to an expansion of the lattice as x increases.

At the intermediate current ($\Delta H = 0.5$), the self-field of the current inside the sample induces a significant density gradient: The density near the left edge is approximately three times the density near the right edge. The lattice experiences a significant strain in the left part of the sample. Slightly beyond the center, it can no longer bear the strain, and plastic deformation occurs. A defect boundary ("fault line") appears, which consists of several aligned dislocations and finite segments of a 30° boundary. The fault line remains more or less stationary as the lattice moves across the sample.

The development of a stationary defect superstructure in a moving vortex lattice is one of the main findings of our computations. Further computations have shown that, in a wider sample, this superstructure is even more developed. The lattice structure at the final time step in a sample whose cross section in the (x, y) plane measured $48\xi\times32\xi$ in a strong current, (H_0 = 1.05, ΔH = 0.75) is shown in Figure 27. Several fault lines are necessary to support the large density differential across the sample. Note that the close-packed direction rotates each time a fault line is encountered.

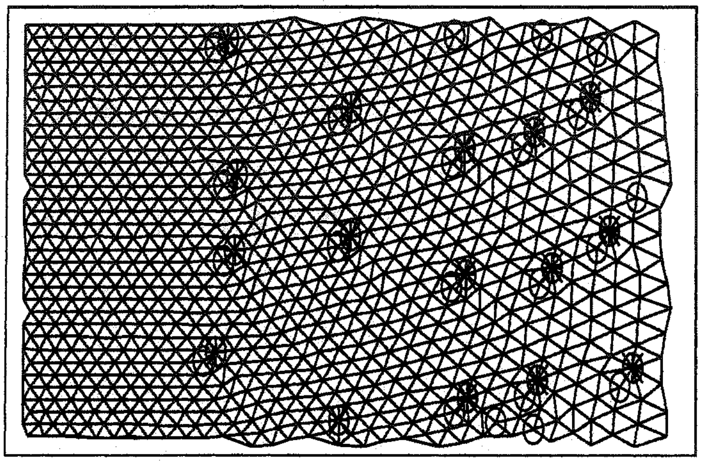

Figure 27. Lattice structure in $48\xi\times32\xi$ sample, $H_0 = 1.05$, $\Delta H = 0.75$; lattice defects are marked.

Summarizing, in this section we have shown a mechanism for plastic motion of a driven vortex lattice in a clean superconductor. The mechanism involves the creation of a superstructure of lattice defects, which supports the gradient in the vortex density induced by the self-field of the current. Although the lattice moves across the sample, the defect superstructure remains static. We have also shown a dynamic reorientation of the lattice. When the current is weak, the lattice is essentially static, and its close-packed direction is aligned with the free surfaces. When the current exceeds a critical value, the lattice moves, and its close-packed direction is aligned with the direction of motion. Finally, we have shown a gradual healing of the lattice defects under the influence of a transport current.

3.10 Dimensional phase transition

In thin films in a parallel applied field, it has been found [38] that the low-field dependence of the magnetization exhibits two maxima, which signal the transition from one to two dimensions (Figure 28). In one dimension the vortices line up along the film, and with increasing field their arrangement changes into a two-dimensional array due to the competition between vortex-surface and vortex-vortex repulsion. In this section we simulate this phenomena using TDGL and achieve a qualitative agreement with the experimental data.

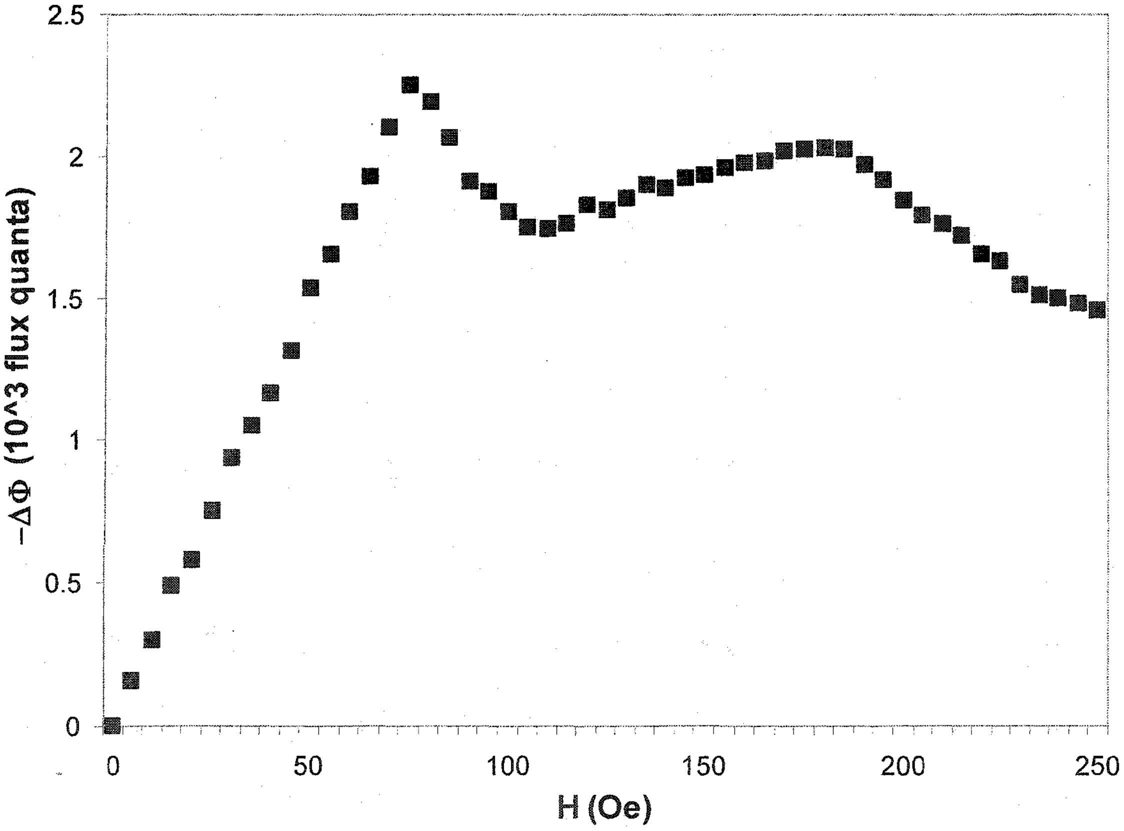

Figure 28. Flux expulsion $\Delta\phi$ as a function of magnetic field, H, at T=1.7K. Nb (16.5 Å)/Cu (16.5 Å) multilayer of total thickness d=0.825μm, T_c=2.61K, $\lambda(0)$=0.5μm.

In Schuller's experiments, the thickness of the films was of the order the penetration length λ. For our numeric experiment, we chose the thickness (in x-direction) of 10ξ for a film with $\kappa = 10$, that is, one penetration length. The sample was periodic in y-direction with the period of 100ξ. This configuration represents a thin film in a parallel field. The magnetic field was slowly increasing from H=0 to H=10 in 100 steps from t=0 to t=50000, so that at each step the system was at quasi-equilibrium at the field applied.

Figure 29 shows the transition from 1D to 2D vortex array, occurring at H=5. Since the penetration depth is comparable to sample thickness, the vortices interact strongly with the Meissner currents. This repulsive interaction tends to align the vortices along the center of the sample until the vortex-vortex repulsion induces a lateral displacement into a two-dimensional array.

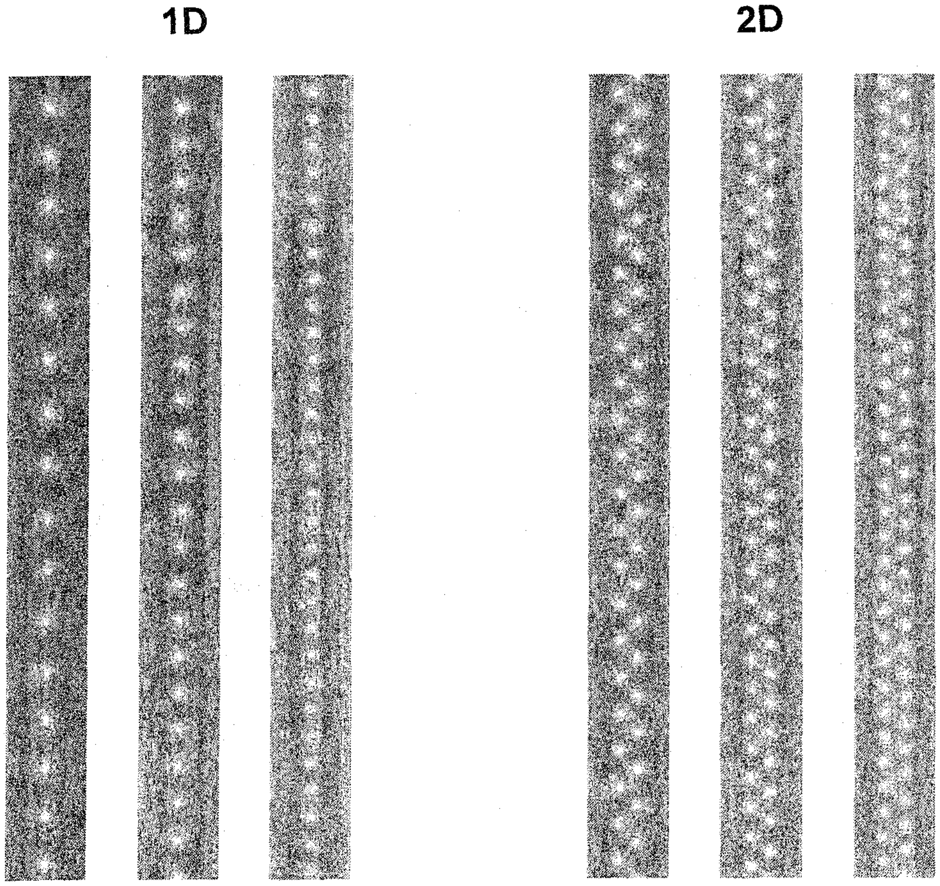

Figure 29. 1D and 2D vortex array in a thin film. H=2.4, 3.6, 4.9, 5.3, 6.6, and 7.3 (left to right).

Figure 30 shows the flux expulsion (magnetization) as a function of applied magnetic field. At low magnetic fields a Meissner effect, indicated by a constant M/H is evident. At higher fields the flux expulsion is not complete and the magnetization as a function of field shows local minima associated with the entrance of vortices. As field increases, the 1D vortex array becomes denser and denser, until at H=5 it transitions into a 2D array, which is observed as a change in the slope of the $M(H)$ curve. This change can be explained by the downplay of two factors: surface barrier (one-dimensional) and vortex-vortex repulsion (two-dimensional). At low fields the vortex array follows the dominant influence of the surface barrier and remains "compressible" only in the *y*-direction. 1D-to-2D transition occurs when the vortex-vortex interaction overcomes the surface barrier and becomes dominant, making the vortex array compressible in two dimensions. This sudden change in dimensionality is reflected in the change of slope and is in good qualitative agreement with the experiment.

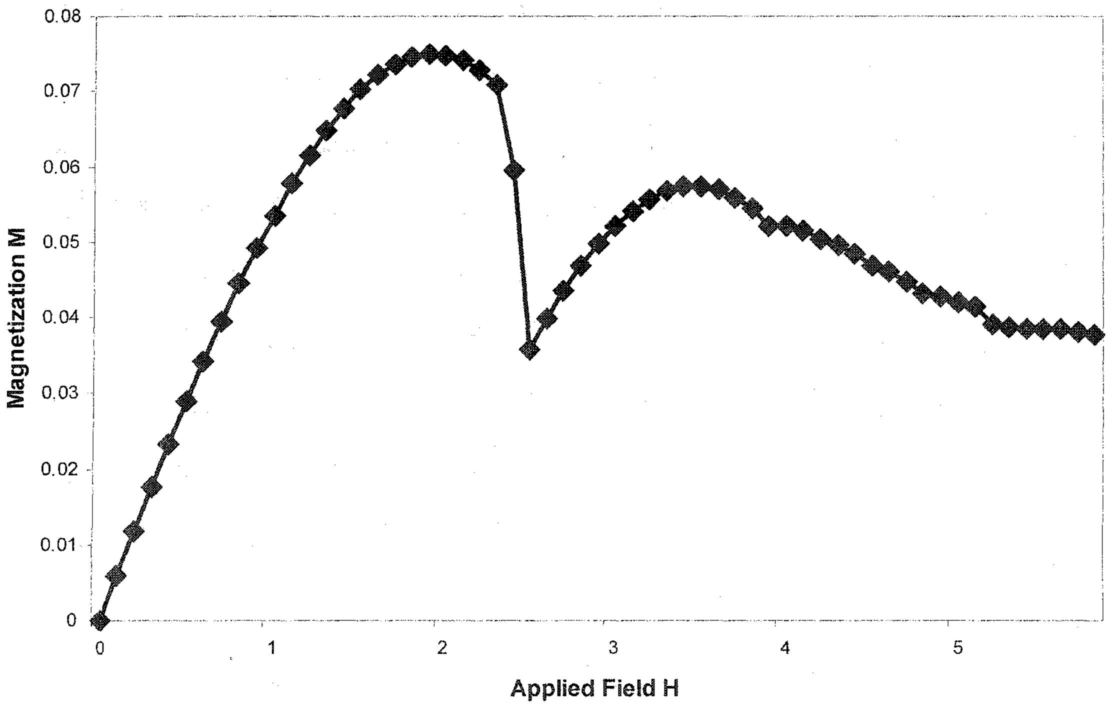

Figure 30. Magnetization *M* as a function of magnetic field *H*.

Chapter 4: Vortex Dynamics in 2D with Defects

The understanding of vortex pinning in high-Tc superconductors is of great interest for applications of superconductors which require strong pinning of vortices as well as the rich variety of behaviors that arise due to the competition of a static or driven elastic media with various forms of quenched disorder [40]. When a transport current passes through a superconductor threaded by vortices, a Lorenz force acts to move the vortices. Their movement leads to the development of a longitudinal potential gradient in the superconductor or, equivalently, the onset of resistance. However, the vortices may be pinned by defects in the material with sufficient force to prevent continuous motion below a certain critical current density. Resistanceless operation of type-II materials above H_{c1} therefore is achievable only in specially prepared so-called hard superconductors in which the pinning force is sufficiently large to prevent flux motion.

4.1 Twin Boundaries

Twin boundaries are a very common defect found in the high-temperature superconductor $YBa_2Cu_3O_7$ and their pinning properties have been extensively studied using Bitter decoration [41], torque magnetometry [43], magnetization [44]-[47], transport [48], magneto-optical imaging [49]-[54], and theoretical studies [55]-[57]. An example of twin boundaries in YBaCuO crystal in polarized light is shown in Figure 31. Many of the earlier experiments on twinned YBaCuO samples found conflicting evidence for the role of twin boundaries in vortex pinning. In particular, the magneto-optical measurements by Duran et al. [49] had shown that twin boundaries act as areas of reduced pinning that allow easy flux penetration, whereas studies by Vlasko-Vlasov et al. [50] found the twin boundaries to be barriers to flux motion. Further magneto-optical studies [51]-[54], systematic computer simulations [57], and transport measurements [48] have shown that these conflicting results can be resolved when the direction of the Lorentz force with respect to the twin boundary is considered. The twin boundary (TB) acts as an easy-flow channel when the Lorentz force is parallel to the twin, but acts as a strong barrier for forces perpendicular to the TB.

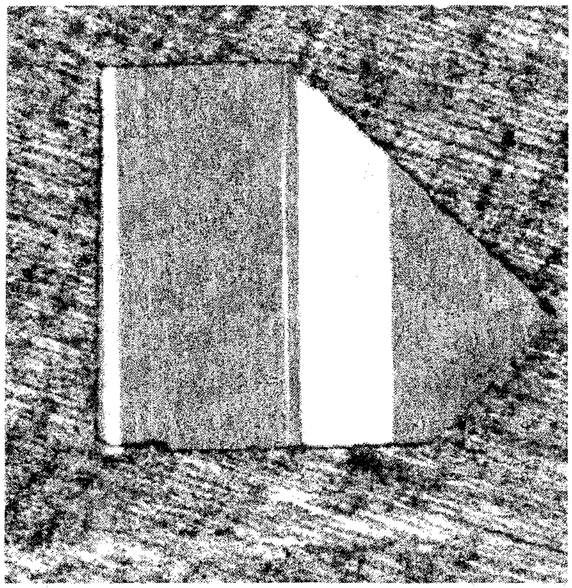

Figure 31. The twin pattern of the YBaCuO crystal as shown in the polarized light photograph.

A very systematic simulational study, using samples with of the order of a million pinning sites, by Groth et al. [57] of the angular dependence of the Lorentz force with respect to the twin boundary showed that, when the angle between the Lorentz force and the twin is large, a portion of the vortices get trapped inside the twin. This produces a pile-up effect leading to a higher density of vortices on one side of the twin in agreement with observations by several groups including, for example, Vlasko-Vlasov et al. [50], Welp et al. [52], and Wijngaarden et al. [54]. At lower angles between the Lorentz force and the twin, molecular dynamics simulations [57] show that the flux moves in channels along the twin boundary while some guided motion of vortices along the edge of the twin still occurs. At the lowest angles the flux flows most easily along the twin with a number of vortices escaping from the twin and forming a flame pattern flux profile in agreement with magneto-optical experiments.

The magneto-optical experiments suggested that guidance of vortices by a twin boundary occurs when the vortex velocity is at an intermediate angle to the boundary plane. Two mechanisms for such guidance can be imagined. In the first, vortices travel within the twin boundary, channeled by the deep pinning potential wells separating the interior of the boundary from the adjoining bulk superconductor. Here it is assumed that the boundary has a finite width and that one or more vortices can travel along its length. This "penetration effect" appears in the experiment as a channel of relatively deep flux penetration along the twin boundary. In the second mechanism, the vortices are imagined to be pinned and stationary on the twin boundary. Vortex-vortex repulsion prevents nearby vortices from crossing the twin boundary, which effectively forms a barrier to perpendicular motion. Parallel motion is allowed, so that driving forces at intermediate angles produce motion only along the boundary. This kind of "external guidance" is to be distinguished from internal guidance, as the motion takes place outside and adjacent to the boundary. To further explore the nature of pinning by twin boundaries and the mechanisms of planar guidance under dynamic conditions, we carried out simulations of vortex motion by solving the time-dependent Ginzburg-Landau equations with a driving force and in the presence of planar pinning defects. The results show both external and internal guidance occurring at different driving forces.

The simulated system consisted of a superconducting planar slab, with a mutually perpendicular current and applied magnetic field in the plane of the slab. Along the field direction the slab was infinite and homogeneous, so that the problem remained two-dimensional. Along the current direction a periodic boundary condition was used to insure continuity of the current without complicated end effects at the entrance and exit surfaces. The repeat distance of the periodic boundary condition was 48λ. The current and field produce a Lorentz force in the direction perpendicular to both. Along this direction the sample had a finite width of 32λ and a physical boundary represented by the condition $J_s \cdot n = 0$, where J_s is the supercurrent density inside the sample and n is normal to the surface.

A single twin boundary was inserted into the sample in the form of a planar slab of thickness 2ξ, oriented parallel to the field and 45° to the current direction. With this orientation, the plane of the boundary is 45° from the Lorentz force direction, a geometry common to the magnetooptical experiments mentioned above. The pinning of the twin boundary was modeled by a local reduction of the condensation energy in the interior of the slab. To provide the experimentally observed resistance to vortex motion within the twin boundary plane [52], the reduction was allowed to fluctuate randomly with a Gaussian distribution around a mean value of 56% and a standard deviation of 25% of the bulk value. Outside the twin boundary, there was no pinning in the bulk of the sample. This model provides an anisotropic pinning configuration with two pinning energy scales, and another for motion transverse to the twin boundary, determined by the reduction in condensation energy from the bulk value. The Ginzburg-Landau parameter $\kappa = 4$ for the simulation. No temperature fluctuations were included, so that the simulations reflect the solid rather than the liquid vortex state.

Each simulation was initiated by a sequence of steps. First a small magnetic field was applied to bring the superconductor into the Meissner state. Then a large field, equivalent to ≈1.13 times the thermodynamic critical field, was applied to bring the system into the vortex state. Simultaneously, a transport current was applied to the system by imposing an applied field $H_L = H+\Delta H$ at the left, $H_R = H-\Delta H$ at the right free surface, where $\Delta H > 0$. By Ampere's law, the field difference $2\Delta H$ causes a current $I = 2\Delta H$ (in dimensionless units) to flow in the sample. Because only the boundary fields are specified, no restriction is put on the transport current distribution within the sample. The transport current induces a Lorentz force on the vortices, which sets them in motion. The motion is allowed to evolve for 10^6 time steps, well after the system reaches steady state. Three currents in the ratio 1:2:4 were applied in separate simulations to probe the effect of an increased driving force on the dynamics. The largest current had a value 8% of the depairing current.

Figure 32 shows the results of the simulation at weak current. (In this and the following figures, the magnetic field direction is out of the page, the transport current direction is vertically up, and the Lorentz force direction is horizontal to the right.) To show the motion of the vortices, the positions of all the vortices sampled during the steady-state motion are plotted in the same frame. Stationary vortices appear as points, moving vortices as lines whose length indicates their average velocity. The position of the twin boundary is marked by the diagonal row of stationary vortices extending from the upper right corner. The Lorentz force induced by the weak current is insufficient to overcome the random pinning forces in the twin boundary, and it effectively forms an impenetrable barrier to vortex motion. The vortices on either side of the boundary move in the parallel direction, displaying the kind of external guidance expected for a barrier geometry.

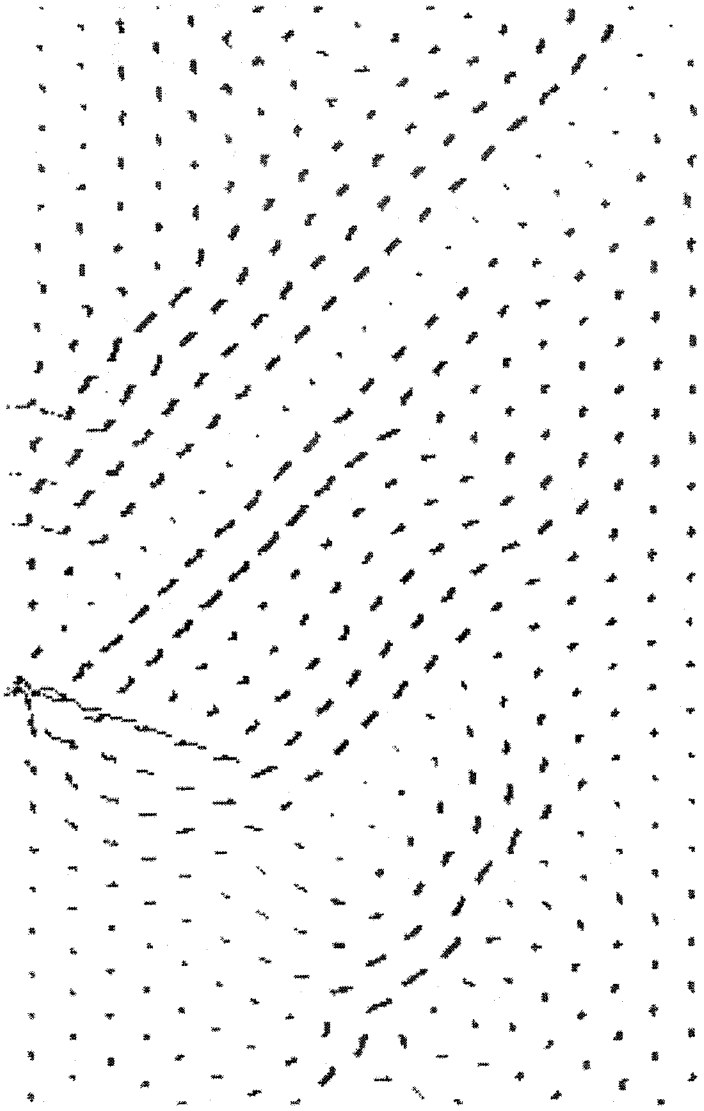

Figure 32. Vortex trajectories near a twin boundary at weak transport current.

There are interesting features about the guided motion that reflect the special dynamics of vortices in the solid rather than the liquid state. The velocity of the vortices changes abruptly from zero on the twin boundary to approximately the maximum value in one vortex spacing on either side of the twin boundary. At larger distances from the twin boundary, the vortex velocity remains approximately constant or decreases. This is different from what is expected for a liquid, where the velocity profile would be expected to grow slowly and monotonically from zero at the boundary to its largest value deep in the liquid. Furthermore, the velocities for several rows above the twin boundary are nearly equal, then fall suddenly almost to zero in one vortex spacing. Likewise, below the twin boundary, the velocities are nearly equal for two rows, then fall to zero. Further below the twin boundary, the velocity rises again, and again falls abruptly to zero.

Both the velocity discontinuities and the high correlation of neighboring velocities are characteristic of the motion of a solid. These two features arise from the shear elastic energy of the solid, which imposes an elastic energy cost on relative displacements of neighboring vortex positions away from their equilibrium values. Because of the shear elastic energy, neighboring vortices tend to maintain the relative positions of the perfect lattice. Thus, sections of the vortex system tend to move with approximately the same velocity. When velocity differences must be accommodated, they are compressed into one vortex spacing as discontinuous changes because this minimizes the elastic energy of the neighboring sections. In contrast, velocity changes in liquids are accommodated continuously, because there is no shear elastic energy cost discouraging relative displacements of neighboring vortices. The high correlation of the velocities of neighboring vortices and the accommodation of velocity changes as discontinuities are characteristic features of plastic flow in solids.

The simulations reveal the microscopic origins of some of the plastic flow discontinuities in the velocity. The surface barrier arising from the boundary condition $J_s{\cdot}n = 0$ at the left and right edges has a strong effect on the motion of the vortices. In a sample without a twin boundary, the surface barrier is homogeneous and the critical current required to overcome the barrier can be computed theoretically. Such estimates of this critical current are confirmed by simulations without twin boundaries [58]. The presence of the twin boundary introduces a weak region in the surface barrier where it intersects with the edge of the sample, allowing vortices to enter at lower current and influencing their entry pattern, as noted below.

Examination of the detailed time evolution of the system shows that the motion exhibited in Figure 32 does not occur continuously, but as a series of rearrangements prompted by the entry of vortices from the left. Each entering vortex distorts the vortex arrangement, near its entry point, and long range relaxation occurs according to the pattern indicated in Figure 32. Thus, vortices entering above the twin boundary trigger the motion of the four rows just above the boundary, while those entering just below the boundary initiate the motion below. The boundary itself acts as a gate, providing a region of weak condensation energy at the left edge of the sample where vortices prefer to enter the system This gate effect is most obvious for vortices entering the sample immediately below the boundary. It is further illustrated by comparison with simulations containing no twin boundary, where the number of vortices in the system is smaller and the surface barrier prevents vortex entry in steady state at this current [59]. While the entry of vortices triggers some of the motion in Figure 32, there is additional motion which occurs far from both the twin boundary and the sample edge. Two rows of vortices near the bottom of the frame move parallel to the boundary without any direct connection to entering vortices or to the boundary itself. This motion illustrates the long-range collective nature of the plastic flow response of the system.

Figure 33 shows the vortex trajectories at intermediate current. Here the pattern of motion is quite different from that at weak current. Many of the vortices break through the twin boundary, the Lorentz force being large enough to overcome the pinning forces of some of the pinning sites. The Lorentz force does not dominate all the pinning sites, as shown by the one remaining stationary vortex in the lower left part of the boundary. This rough balance between the pinning and Lorentz forces leads to a qualitatively new behavior. The external guidance, which was dominant at weak current, is missing at intermediate current, although a clear vestige of it can still be seen below the lower left section of the boundary. Elsewhere along the boundary, weak external guidance can be seen, extending no more than one row on either side of the boundary.

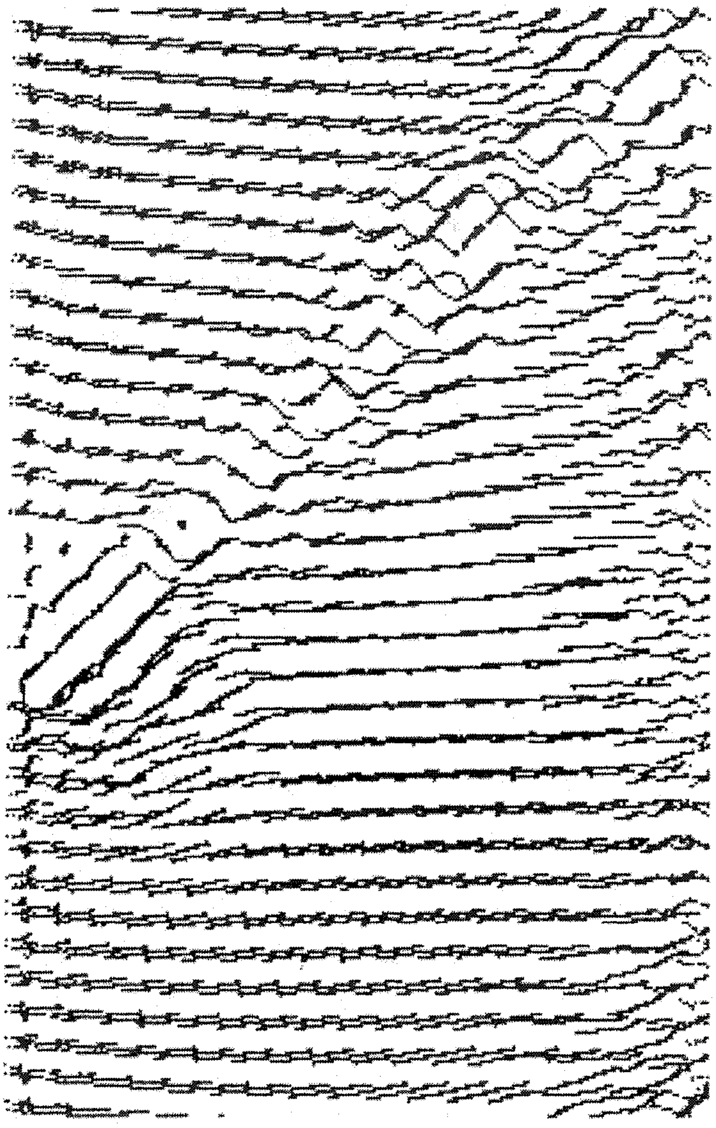

Figure 33. Vortex trajectories at intermediate transport current.

Inside the boundary, there is considerable motion along the boundary in certain regions, especially at the lower left and upper right. This is internal guidance. It differs from the penetration effect suggested by the magneto-optical experiments, in that it occurs in the absence of any bulk pinning outside the twin boundary. Thus, the vortex density inside the boundary is not substantially different from that outside the boundary. In the magneto-optical experiments, the twin boundaries were seen to admit flux when the bulk of the sample was relatively flux free. To study such a penetration effect, the simulation would have to take into account bulk pinning outside the twin boundary. Figure 33 shows that the internal motion is associated with external motion of the neighboring vortices on either side of the boundary. This behavior is consistent with the influence of the shear modulus, which tends to cause neighboring vortices to move at the same velocity. Thus, coupled internal and external motion is a natural consequence of a finite shear modulus.

The internal motion can be understood physically in terms of the random pinning potential and the balance between the Lorentz and pinning forces. The linear array of random pinning wells creates a highly anisotropic pinning environment. A vortex on a particular pinning site sees the full well potential as the barrier to motion in the direction perpendicular to the boundary. In contrast, in the parallel direction the potential barrier to the next well may be greatly reduced, if the neighboring well has approximately the same depth. Thus is may be much easier for the vortices to jump to the neighboring well than to the bulk of the superconductor. This kind of internal motion will stop if the moving vortex encounters a particularly well pinned vortex, as occurs near the lower left of the boundary, or if the well depth becomes shallow enough for the vortex to jump to the bulk. Such escapes to the bulk can be seen in the upper right section of the boundary.

The effect of the boundary on the vortex motion at intermediate current is apparent, but it is not the dominant force as was the case at weak current. This is clearly seen in the parts of the sample away from the boundary, where the vortices move steadily to the right, rather than diagonally as at weak current where the boundary was an effective barrier. The spatial range of influence of the boundary is confined to one vortex spacing. Beyond that, there is at most a small influence on the vortex velocity directions, in contrast to the case at weak current where the barrier was impenetrable. Ultimately, most of the vortices penetrate the boundary after undergoing a perturbation in velocity direction at the boundary itself. Thus the guidance provided by the boundary is local in nature and not a determining feature of the average motion.

Figure 34 shows the vortex trajectories at strong current. Only the trajectories in the first 20% of the steady-state time window are shown, because otherwise the frame becomes too crowded to resolve individually vortex paths. Here the boundary is nearly powerless against the Lorentz force, and many of the vortices stream through with hardly a change in direction. There is a hint of internal guidance at the extreme lower left of the boundary, but otherwise the trajectories do not show coherent vortex motion that can be attributed to the boundary.

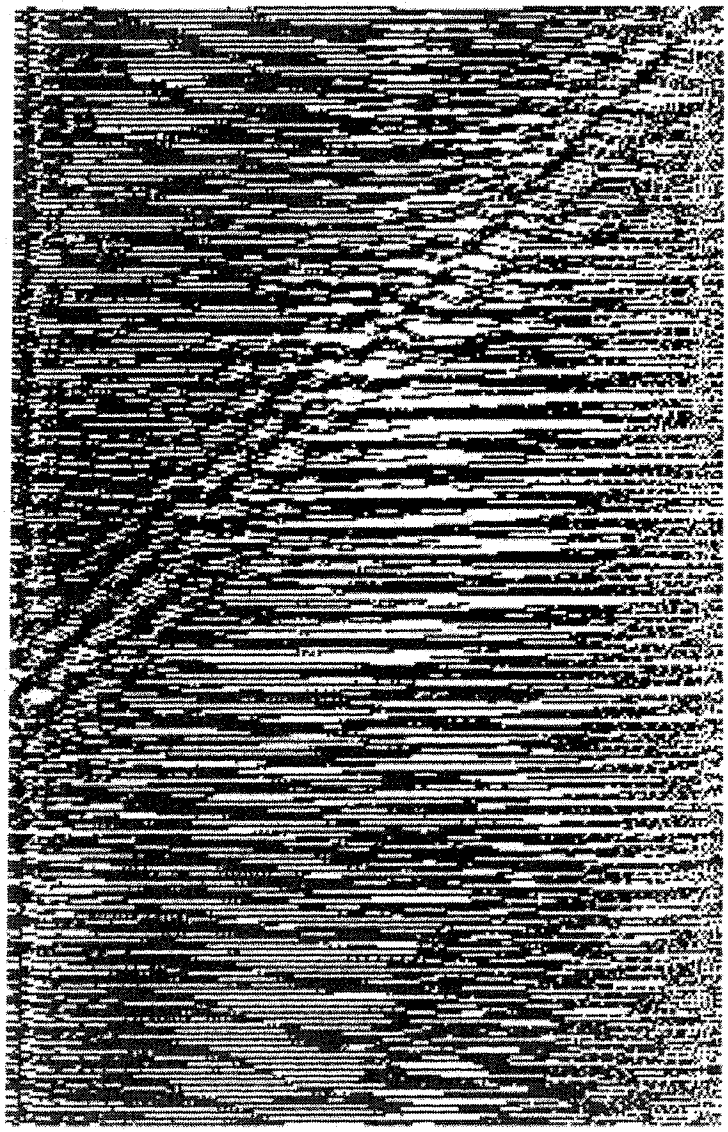

Figure 34. Partial vortex trajectories at strong transport current.

4.2 Point Defects

The TDGL equations enable a close look at vortex motion through arrays of point defects. The numerical simulations in this section show the actual effect of two regular defect arrangements – one with rectangular symmetry, the other with triangular symmetry – on the number of vortices, the vortex trajectories, and the magnetic field in a superconductor.

The simulations lead to a number of observations. The triangular defect arrangement accommodates more vortices (at steady state) than the rectangular defect arrangement and is slightly more effective at vortex pinning, at least at weak driving currents. Vortices travel along well-established tracks, which are formed early in the transient phase. The average vortex spacing increases in the direction of vortex motion and enforces the formation of fault lines in the lattice structure of the moving vortices. When the driving force is weak, the magnetic field is determined primarily by the vortices that are pinned on the defects, and vortex motion in the transverse direction has a smoothing effect on the magnetic field.

The basic configuration used for these simulations is two dimensional: a superconductor measuring $33\lambda \times 48\lambda$, periodic in y. A bulk transport current is generated in the y direction by a field differential between the left and right surface, $B_L = 2H$, $B_R = 0$. H is thus the average applied field, which is variable.

A total of 160 point defects are arranged regularly in the interior in 16 rows and 10 columns. The columns are 3λ apart, so a defect-free zone of 3λ is left adjacent to the left and right surface. A defect covers one computational mesh cell (which is one-half coherence length on each side), so the density of the defects is 0.16%. All defects have the same strength; the condensation energy at each defect is 56% of the bulk value. In the arrangement with rectangular symmetry, the defects are placed in a regular square pattern; in the arrangement with triangular symmetry, every other column is shifted vertically over a distance 1.5λ.

We note that it takes considerable time to reach the steady state, especially when the defects are arranged in a triangular pattern and when the bulk transport current is weak.

Figure 35 illustrates the observation that the triangular defect arrangement accommodates more vortices than the rectangular defect arrangement. The number of vortices in the system at steady state (including the 160 vortices that are pinned on the defects at all times) ranges from approximately 413 at *H*=0.9375 to 745 at *H*=1.375 and is generally higher for the triangular arrangement. The one exception, at the weakest current, indicates that the steady state was probably never reached in this case. The difference is small but measurable (approximately 5%), and becomes smaller as the driving force increases. At the strongest current considered here, the difference has disappeared altogether.

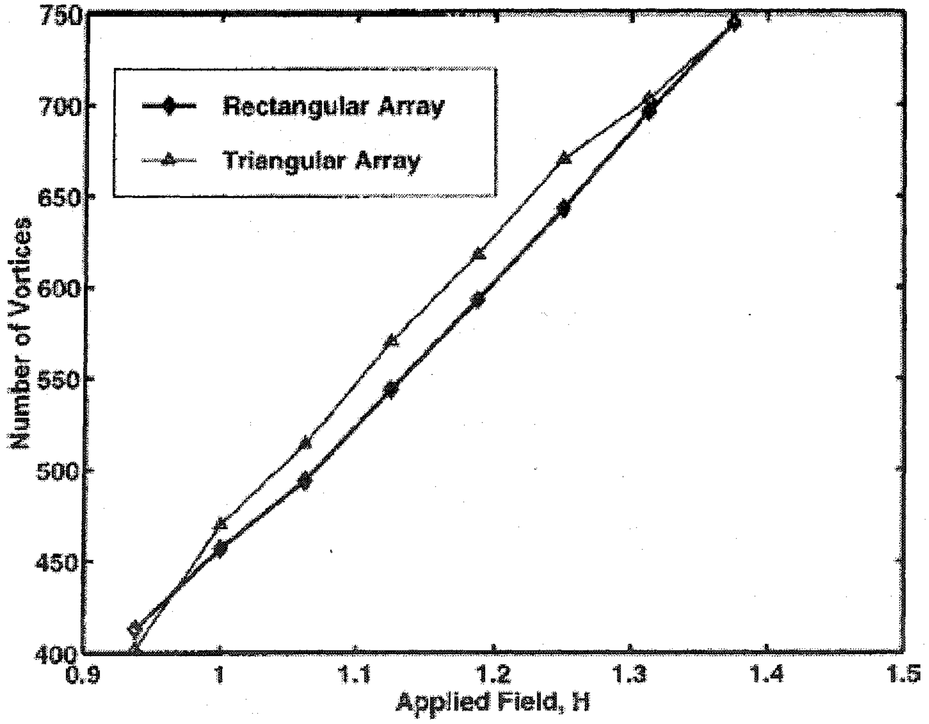

Figure 35. Number of vortices at steady state as a function of the applied field.

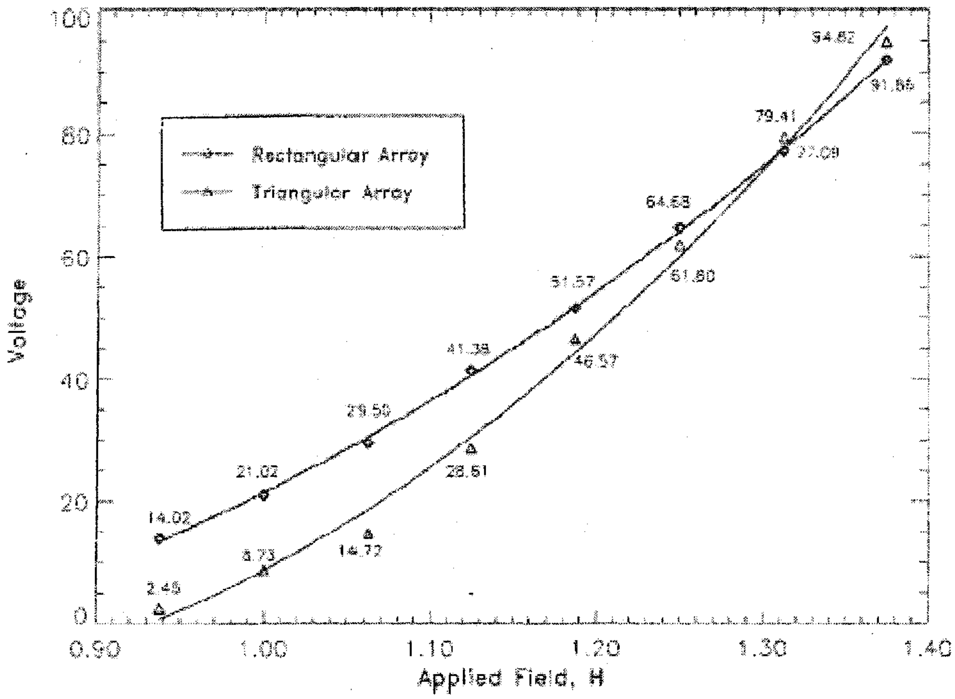

Figure 36. Current ($I = 2H$) vs. voltage.

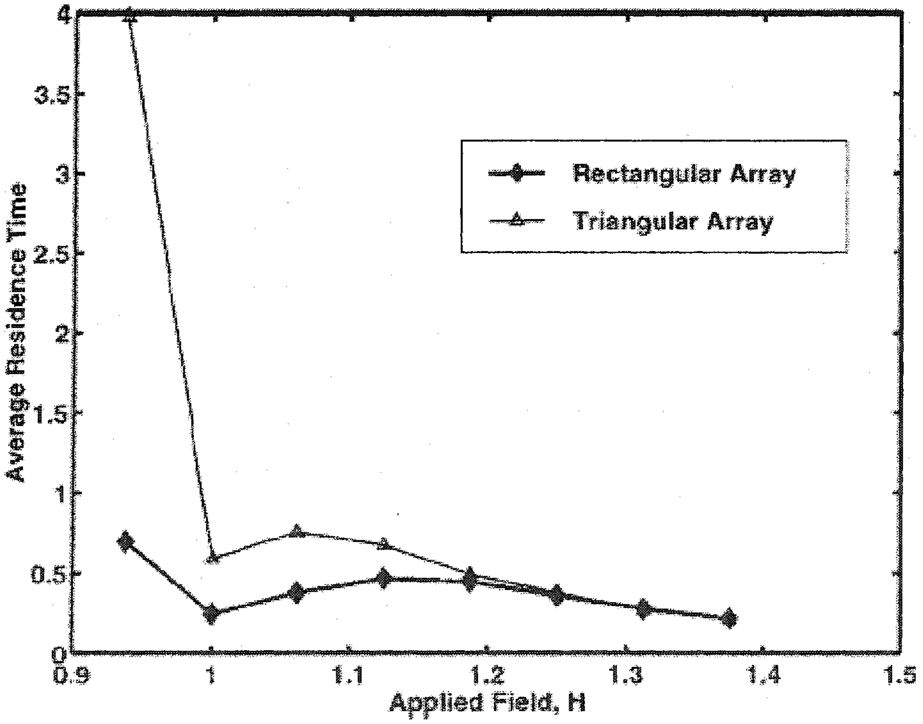

Figure 37. Vortex residence time at steady state as a function of the applied field.

Figure 36 and Figure 37 support the observation that the triangular defect array may be more effective at vortex pinning, at least at weak driving currents. Figure 36 shows the *I-V* curves deduced from the simulations ($I = 2H$). The rectangular defect arrangement yields a higher voltage at low currents and a lower voltage at high currents; the crossover occurs around $H = 1.3$, a little below the strongest driving force used in these simulations.

Figure 37 shows the residence times, a measure of the average time spent by a vortex in the system as it moves across the sample (not counting vortices that are pinned). The triangular defect arrangement forces the vortices to spend more time in the system, certainly at weak currents. The difference becomes less pronounced as the driving force increases, and beyond some point the arrays appear equally effective.

The vortex trajectories are shown in Figure 38 (rectangular defect arrangement) and Figure 39 (triangular defect arrangement). Both cases show that the vortices tend to travel along well-established tracks – a phenomenon shown most graphically by Harada et al. [60]. The track patterns are established during the transient phase and maintained in a very stable manner during the steady state.

4.2.1 Rectangular lattice

When the driving current is weakest, the tracks are straight and run midway between the defects. Deviations from this pattern occur near the left surface; for example, some vortices are being trapped at an interstitial site, while others that had been trapped earlier at an interstitial site manage to escape and travel down the nearest available straight-line track. The vortex pattern is highly regular; a triangulation of the moving vortex lattice shows that it is virtually free of defects.

As the average field (and, hence, also the driving current) increases, more vortices need to be accommodated, and multiple tracks develop between adjacent defects near the left surface, where the vortices enter. The straight-track pattern observed at weak current still exists but is pushed further into the interior. In the left zone, vortices are squeezed between vertically adjacent defects along two tracks in an alternating pattern, their passage being facilitated by a slight up-and-down motion of the vortices that are pinned at the interstitial sites. Gradually, as the vortices are driven to the right and accelerate, the tracks straighten out and merge to form the straight-line track pattern observed at the weakest current. Since the number of vortices flowing across the sample per unit time is constant, the increase in vortex velocity is accompanied by a corresponding decrease in vortex density. In fact, the density seems to change rather abruptly where the tracks merge. This rather abrupt change in the vortex density is associated with a fault line in the structure of the vortex lattice. Fault lines provide a mechanism to accommodate strains resulting from an increase in the intervortex spacing. [61]

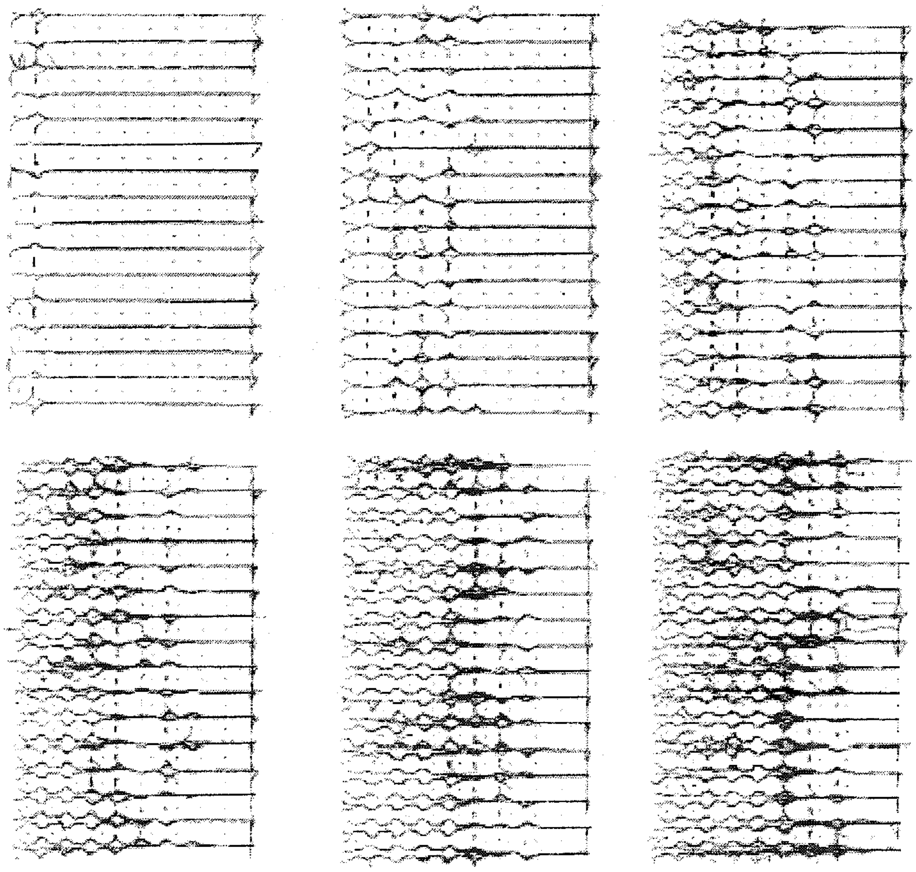

Figure 38. Vortex trajectories through a rectangular array of point defects; top row, from left to right: $H = 0.9375, 1.0625, 1.1875$; bottom row, from left to right: $H = 1.250, 1.3125, 1.375$.

The up-and-down motion of the vortices that are pinned at the interstitial sites (mentioned in the preceding paragraph) can be observed directly. But there is also indirect evidence. Figure 40 shows the temporal evolution of the voltage drop between two leads placed, respectively, at 2.5λ from the left surface, at the center of the sample, and at 2.5λ from the right surface ($H = 1.375$). During an initial transient, which starts successively at the left-most, center, and right-most position, the voltage rises to some nonzero average value. Once the steady state is reached, each voltage keeps oscillating, and the oscillations are clearly modulated. The oscillations mark the passage of individual vortices across the line joining the leads. They are stronger near the surfaces, and their average frequency is determined by the vortex velocity and density. The modulations are manifestations of the up-and-down motion of the vortices that are pinned at the interstitial sites; as they move, they exert an accelerating or decelerating influence on the velocity of each passing vortex.

4.2.2 Triangular lattice

Especially at the weakest current, many vortices are again pinned at interstitial sites in the bulk. They force approaching vortices into a northeastern or southeastern direction and create the open loops in the hexagonal track pattern. A triangulation of the positions of the moving vortices shows a lattice structure with a fair number of defects, but no discernible patterns. As the average field increases and more vortices need to be accommodated, the hexagonal pattern near the left surface is replaced by a quadrilateral (diamond) pattern. The hexagonal pattern still persists, but further into the interior. The transition occurs in one or at most two column widths. This transition zone separates a high-density region on the left from a low-density region on the right. Again, a decrease in density is accompanied by a corresponding increase in velocity, so the flux remains constant. As more vortices must be accommodated, vertical motion of the vortices becomes more difficult near the left surface. The diamonds open up, and the tracks become more clearly separated.

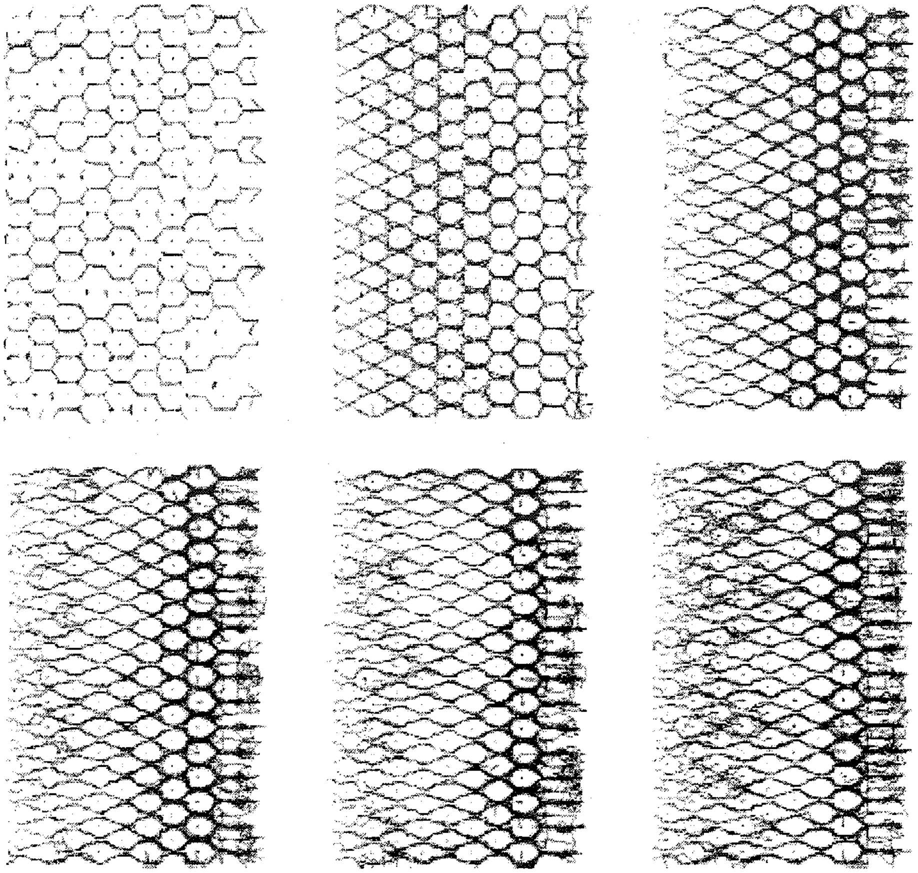

Figure 39. Vortex trajectories through a triangular array of point defects; top row, from left to right: $H = 0.9375$, 1.0625, 1.1875; bottom row, from left to right: $H = 1.250$, 1.3125, 1.375.

Figure 41 shows the magnetic field B, across the superconductor for various values of H. The thick curves correspond to the rectangular defect arrangement, the thin curves to the triangular defect arrangement. When the driving force is weak (bottom curves), the magnetic field is determined primarily by the vortices that are pinned on the defects, and the maxima coincide with the x positions of the defects. The maxima are less pronounced when the defects are arranged in a triangular pattern than when they are arranged in a rectangular pattern. The smoothing is a result of vortex motion in the transverse (y) direction; in the rectangular arrangement such motion is virtually absent, while it is relatively significant in the triangular arrangement (see Figure 38 and Figure 39).

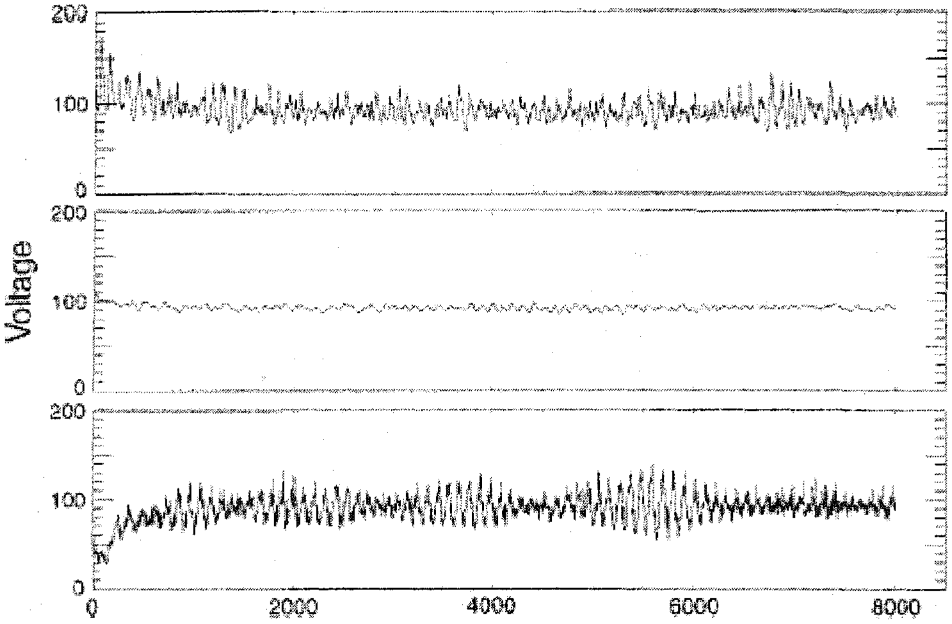

Figure 40. Temporal evolution of the voltage drop along a vertical line at 2.5λ from the left surface (top), in the center of the sample (middle), and at 2.5λ from the right surface (bottom). The width of the superconductor is 33λ. ($H = 1.375$)

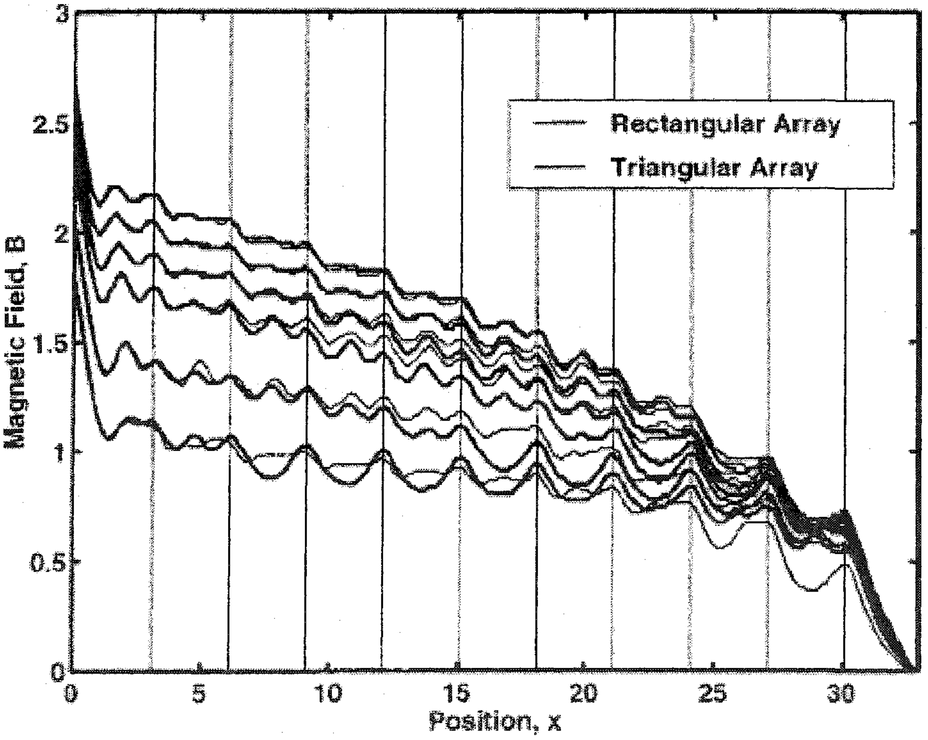

Figure 41. Magnetic field across the sample (averaged over y). From bottom to top: H = 0.9375, 1.0625, 1.1875, 1.250, 1.3125, 1.375. Vertical lines mark the positions of the defects.

As the driving force increases (middle curves), motion in the *y* direction becomes more significant, both with the rectangular and the triangular defect arrangement. The field still shows some oscillatory behavior, but the oscillations are less pronounced. The field appears to be slightly stronger in the triangular case. At the strongest driving force (top curves), the difference between the two arrangements has virtually disappeared. The field is determined by the moving vortices, and in both cases there is enough motion in the *y* direction that the field profile is almost flat between adjacent defect columns.

Several of the findings outlined above have been confirmed in other simulations. For example, we observe channel motion in a large superconductor ($120\lambda \times 48\lambda$) with randomly placed point defects. While some vortices are pinned on the defects, others move through meandering tracks passing between the point defects. The channels form during the transient phase and remain remarkably stable. Their shape is irregular because of the random placement of the defects. After introducing thermal noise, we still observe channel motion, but the phenomenon is considerably obscured by the fluctuations in the vortex trajectories. Also, the motion evolves on a different time scale and is more akin to creep motion.

4.3 Finite-size Defects

New technologies provide the means for the preparation of controlled structures of size comparable to the important length scales which control the physical properties of materials. Artificial structures can be made with sizes of the order of the relevant length scales such as the coherence length ξ and the penetration depth λ. This has produces a renewed experimental and theoretical interest in pinning effects by ordered arrays of defects in type-II superconductors.

Some possibilities that have been explored include regular lattices of holes in superconducting films, submicrometric magnetic dots, and spacially modulated e-beam irradiation damage in YbaCuO. These artificial structures exhibit interesting and unusual effects. Several phase transitions in the vortex lattice of high-temperature superconductors are inferred from neutron scattering or transport measurements. These transitions, which occur in a glassy vortex lattice phase, have been interpreted in terms of a balance between the pinning and elastic energy of the vortex matter. The flux flow magnetoresistance presents minima at regular field intervals when the vortex lattice geometrically matches the array of finite-size defects.

In this chapter, we study the pinning effects of rectangular and triangular arrays of longitudinal finite-size defects in a superconducting film in parallel magnetic field, at different transport currents.

The configuration studied is a sample of thickness of 160ξ in x-direction, periodic in y-direction with the same 160ξ period, divided into a 400x400 grid. An array of 110 dots (11 columns in x by 10 rows in y) of diameter 8ξ of "strength" $\gamma = 1$ represented an artificial defect structure. Superconductor had the Ginzburg-Landau parameter $\kappa = 4$. The TDGL equations were integrated to time $t = 5000$ in 0.1 steps.

4.3.1 Rectangular lattice of dots

Rectangular defect lattice used in this simulation is shown in Figure 42. It consists of a rectangular array of 110 dots (11 columns in x by 10 rows in y (periodic)) of diameter 8ξ of "strength" $\gamma = 1$.

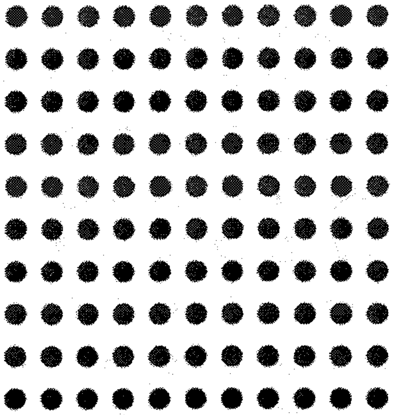

Figure 42. Rectangular lattice of round defects.

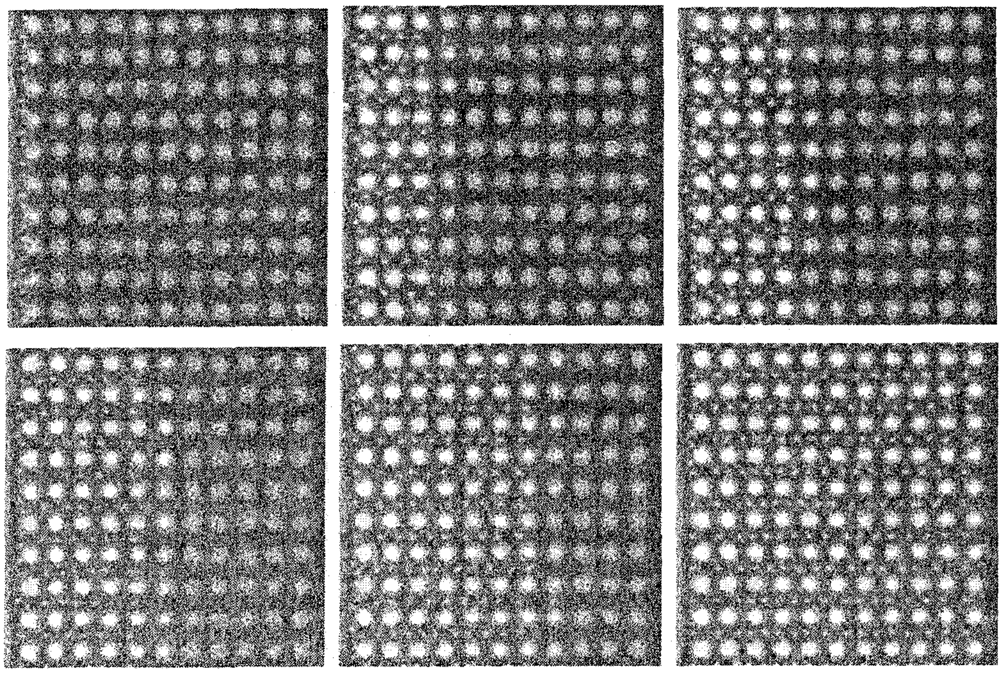

Figure 43. Vortex flow at (left to right, top to bottom) $t = 10, 50, 100, 200, 400, 1000$ in a rectangular lattice of defects for $H = 0.5$ and $I = 1$.

Figure 43 shows the establishment of a steady vortex flow in the applied magnetic field $H = 0.5$ and transport current in y-direction $I = 1$. As can be seen, each defect is capable of pinning several flux quanta. As vortices fill the defects, they penetrate further in the bulk of the sample. The "full" defects serve as repulsion centers, while "empty" defects serve as attraction centers. These forces, combined with the Lorenz force, determine the dynamics of vortex motion at this stage. Once all the defects are "full", no more vortices can enter them, so the vortices move in the "channels" between the defects, creating steady "rivers" of flux motion.

Figure 44 shows the steady vortex flow at different applied magnetic fields and transport currents: $H = 0.5$, $I = 1$; $H = 1$, $I = 0.5$; $H = 1$, $I = 2$; $H = 2$, $I = 2$. As Lorentz force increases and distance between vortices decreases, moving vortices are able to overcome the potential barrier of the flux trapped in the defects and "swap" with the trapped vortices. This allows vortices move more uniformly across the lattice so that the "river" effect is less and less pronounced. At fields close to critical, the lattice of defects causes virtually no influence on vortex motion; rather, it averages the collective pinning, effectively creating a uniform viscous resistance to vortex motion.

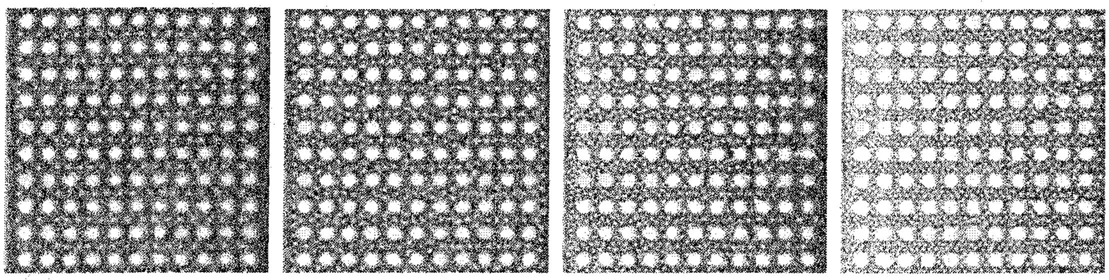

Figure 44. Steady vortex flow for rectangular lattice of defects at (left to right) $H = 0.5, I = 1$; $H = 1, I = 0.5$; $H = 1, I = 2$; $H = 2, I = 2$.

4.3.2 Triangular lattice of dots

Triangular defect lattice used in this simulation is shown in Figure 45. It consists of a triangular array of 110 dots (11 columns in x by 10 rows in y (periodic)) of diameter 8ξ of "strength" $\gamma = 1$.

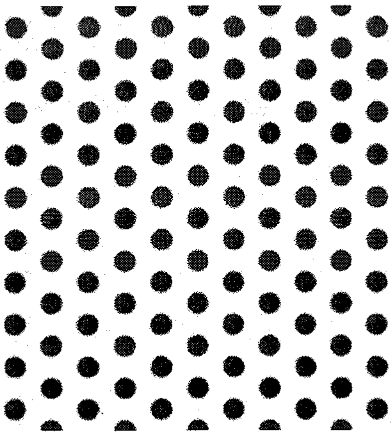

Figure 45. Triangular lattice of round defects.

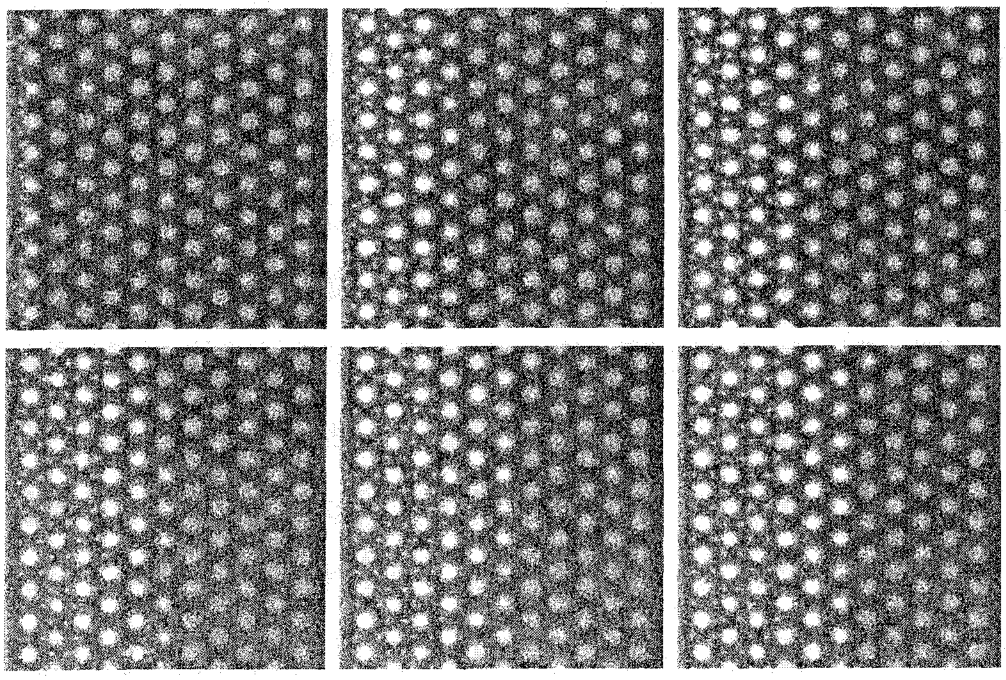

Figure 46. Vortex flow at (left to right, top to bottom) $t = 10, 50, 100, 200, 400, 1000$ in a triangular lattice of defects for $H = 0.5$ and $I = 1$.

In a striking contrast to the rectangular configuration, triangular lattice stops the vortex motion completely in weak magnetic field $H = 0.5$ and transport current $I = 1$ (Figure 46). Trapped vortices (multiple flux quanta per defect) create an unpenetrable barrier to vortex entry. As can be seen from the figure, the right half of the sample is remains completely vortex-free.

Stronger applied field and current overcome the potential barrier of the traps (Figure 47). However, there is no clearly pronounced "river" effect as in rectangular lattice. New vortices enter the traps as old ones leave them.

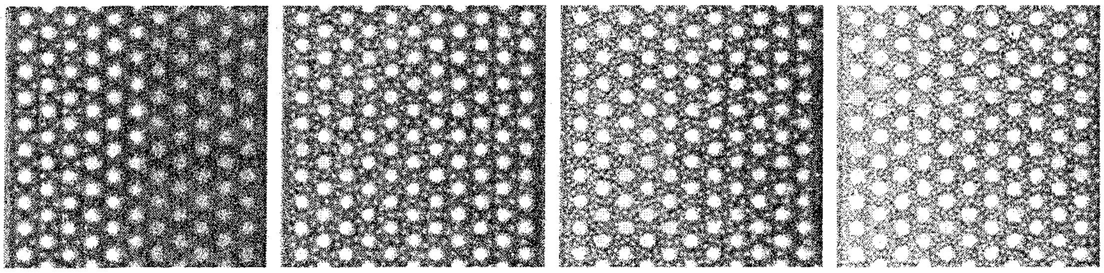

Figure 47. Steady vortex flow for triangular lattice of defects at (left to right) $H = 0.5, I = 1$; $H = 1, I = 0.5$; $H = 1, I = 2$; $H = 2, I = 2$.

As can be seen from the table below, at small fields and currents the triangular lattice creates greater resistance, while at large fields the arrangement of defects does not matter and it is the percentage of the area covered by defects that only matters.

Applied Field H	**Current I**	**Avg Voltage V**	**Resistance R**	**Avg Induction B**	**Magnetization M**
		Rectangular Lattice			
0.5	1	0.0054	0.0054	0.49	0.01
1	0.5	0.028	0.056	0.86	0.14
1	2	0.81	0.40	1.19	-0.19
2	2	1.48	0.74	2.05	-0.051
		Triangular Lattice			
0.5	1	0.0	0.0	0.30	0.20
1	0.5	0.041	0.082	0.83	0.17
1	2	0.77	0.39	1.19	-0.19
2	2	1.47	0.73	2.05	-0.048

Epilogue

The research presented in this thesis resulted in developing highly efficient numerical methods for simulation of the dynamic behavior of the type-II superconductors under various conditions, both without and with the defects. The simulations carried out allowed us to study phenomena which oftentimes are not possible to observe in an experiment (e.g. transitional dynamics of vortex entrance, vortex annihilation, symmetry breaking, and interaction of vortices and defects).

The numerical model and code developed in this thesis allow one to run simulations on a personal computer and obtain results within a matter of hours. These results can be compared to experimental data and important material parameters of the superconductor can be deduced. Furthermore, the simulations can be used to construct efficient artificial pinning structures which result in desired material characteristics – an experimentation which would be otherwise very expensive and time-consuming to do with real samples.

Novel results of this thesis include the design of a single-vortex “generator”, which can be used to produce one flux quantum at a time (a feature potentially useful for the future generation of quantum computers); an explanation of the dimensional phase transition first observed experimentally in thin films in a parallel applied magnetic field; and the dynamics of vortex-defect interaction in artificial lattices of finite-size defects.

Finally, this thesis presents a solid foundation for further research on more complex and resource-demanding three-dimensional time-dependent Ginzburg-Landau equations, which can be used to simulate even broader range of the experimental data and phenomena.

Appendix A Derivation of the Ginzburg-Landau Equations

We start by writing the GL free-energy as

$$L\left[\psi,\psi^*,A\right]=L_n+\frac{1}{V}\int d^3r\left[\begin{array}{c}\frac{1}{2m_s}\left(-i\hbar\nabla+\frac{e_s}{c}A\right)\psi^*\cdot\left(i\hbar\nabla+\frac{e_s}{c}A\right)\psi+\\+\frac{1}{8\pi}H^2(\boldsymbol{r})+a\tau\psi^*\psi+\frac{1}{2}b\psi^*\psi\psi^*\psi\end{array}\right] \tag{A.1}$$

Since the volume V is fixed, the usual Euler equations apply (along with suitable boundary conditions on ψ and A). Furthermore, we will be making a variation with respect to a vector quantity, $\boldsymbol{A}$, and so we will make use of the chain rule of differentiation to write

$$\frac{\partial}{\partial A}=\frac{\partial A_x}{\partial A}\frac{\partial}{\partial A_x}+\frac{\partial A_y}{\partial A}\frac{\partial}{\partial A_y}+\frac{\partial A_z}{\partial A}\frac{\partial}{\partial A_z}$$

The nth component of any vector is simply $A_n=\hat{\boldsymbol{n}}\cdot\boldsymbol{A}$, where $\boldsymbol{n}$ is the unit vector along the nth coordinate axis. Thus

$$\frac{\partial}{\partial A}=\hat{\boldsymbol{x}}\frac{\partial}{\partial A_x}+\hat{\boldsymbol{y}}\frac{\partial}{\partial A_y}+\hat{\boldsymbol{z}}\frac{\partial}{\partial A_z}=\sum_i\hat{\boldsymbol{x}}_i\frac{\partial}{\partial A_i}$$

The Euler equations for this problem are

$$\frac{\partial L}{\partial\psi^*}-\sum_i\frac{\partial}{\partial x_i}\left(\frac{\partial L}{\partial\left(\partial\psi^*/\partial x_i\right)}\right)=0$$

and

$$\sum_i \hat{x}_i \left[\frac{\partial L}{\partial A_i} - \sum_j \frac{\partial}{\partial x_j} \left(\frac{\partial L}{\partial \left(\partial A_i / \partial x_j \right)} \right) \right] = 0$$

where L is the integrand of Eq. (A.1), i.e. the free-energy density.

For the first GL equation we expand the integrand of Eq. (A.1) and then use straight forward differentiation to find

$$L = \frac{1}{2m_s} \left[\hbar^2 \nabla \psi^* \cdot \nabla \psi + \frac{e_s^2}{c^2} A^2 \psi^* \psi + \frac{i\hbar e_s}{c} A \cdot \left(\psi^* \nabla \psi - \psi \nabla \psi^* \right) \right] + \\ + \frac{1}{8\pi} (\nabla \times A) \cdot (\nabla \times A) + a\tau \psi^* \psi + \tfrac{1}{2} b \psi^* \psi \psi^* \psi$$

$$\frac{\partial L}{\partial \psi^*} = \frac{1}{2m_s} \left[\frac{e_s^2}{c^2} A^2 \psi + \frac{i\hbar e_s}{c} A \cdot \nabla \psi \right] + a\tau\psi + b\psi^2 \psi^* \tag{A.2}$$

$$\frac{\partial L}{\partial \left(\partial \psi^* / \partial x_j \right)} = \frac{1}{2m_s} \left(\hbar^2 \frac{\partial \psi}{\partial x_j} - \frac{i\hbar e_s}{c} \psi A_j \right)$$

$$\sum_j \frac{\partial}{\partial x_j} \left(\frac{\partial L}{\partial \left(\partial \psi^* / \partial x_j \right)} \right) = \frac{1}{2m_s} \sum_j \left[\hbar^2 \frac{\partial^2 \psi}{\partial x_j^2} - \frac{i\hbar e_s}{c} \frac{\partial \psi}{\partial x_j} A_j - \frac{i\hbar e_s}{c} \psi \frac{\partial A_j}{\partial x_j} \right] =$$

$$= \frac{1}{2m_s} \left[\begin{array}{r} \hbar^2 \left(\frac{\partial^2 \psi}{\partial x^2} + \frac{\partial^2 \psi}{\partial y^2} + \frac{\partial^2 \psi}{\partial z^2} \right) - \frac{i\hbar e_s}{c} \left(A_x \frac{\partial \psi}{\partial x} + A_y \frac{\partial \psi}{\partial y} + A_z \frac{\partial \psi}{\partial z} \right) - \\ - \frac{i\hbar e_s}{c} \psi \left(\frac{\partial A_x}{\partial x} + \frac{\partial A_y}{\partial y} + \frac{\partial A_z}{\partial z} \right) \end{array} \right] = \tag{A.3}$$

$$= \frac{1}{2m_s} \left[\hbar^2 \nabla^2 \psi - \frac{i\hbar e_s}{c} (A \cdot \nabla \psi) - \frac{i\hbar e_s}{c} \psi (\nabla \cdot A) \right]$$

Subtracting the expression (A.3) from (A.2) yields the first GL equation,

$$\frac{1}{2m_s} \left[\frac{e_s^2}{c^2} A^2 \psi + \frac{2i\hbar e_s}{c} A \cdot \nabla \psi - \hbar^2 \nabla^2 \psi \right] + a\tau\psi + b|\psi|^2 \psi = 0 , \tag{A.4}$$

where the choice of gauge ($\nabla \cdot A$) eliminates the last term of (A.3). This may also be expressed as

$$\frac{1}{2m_s}\left(i\hbar\nabla+\frac{e_s}{c}A\right)+a\tau\psi+b|\psi|^2\psi=0\,. \tag{A.5}$$

The derivatives of the second Euler equation are straightforward but first we need to expand the H^2 term. In terms of the curl operator we have

$$(\nabla\times A)\cdot(\nabla\times A)=\left(\sum_{i,j,k}\varepsilon_{ijk}\hat{x}_i\frac{\partial A_k}{\partial x_j}\right)\cdot\left(\sum_{n,l,m}\varepsilon_{nlm}\hat{x}_n\frac{\partial A_m}{\partial x_l}\right)=\sum_{i,j,k,l,m}\varepsilon_{ijk}\varepsilon_{ilm}\frac{\partial A_k}{\partial x_j}\frac{\partial A_m}{\partial x_l},$$

where the indices $i,j,k,l,m=\{1,2,3\}$ and ε_{ijk} is the Levi-Cevita symbol from vector analysis. Using the identity $\varepsilon_{ijk}\varepsilon_{ilm}=\delta_{jl}\delta_{km}-\delta_{ml}\delta_{kl}$ this becomes

$$(\nabla\times A)\cdot(\nabla\times A)=\sum_{l,m}\left[\left(\frac{\partial A_m}{\partial x_l}\right)^2-\frac{\partial A_m}{\partial x_l}\frac{\partial A_l}{\partial x_m}\right].$$

As before, we proceed to evaluate the derivatives in the Euler equation:

$$\frac{\partial}{\partial\left(\partial A_i/\partial x_j\right)}(\nabla\times A)^2=\sum_{l,m}\left[2\frac{\partial A_m}{\partial x_l}\delta_{im}\delta_{jl}-\frac{\partial A_l}{\partial x_m}\delta_{im}\delta_{jl}-\frac{\partial A_m}{\partial x_l}\delta_{il}\delta_{jm}\right],$$

$$\frac{\partial}{\partial x_j}\left(\frac{\partial}{\partial\left(\partial A_i/\partial x_j\right)}\right)(\nabla\times A)^2=\sum_{l,m}\left[2\frac{\partial^2 A_m}{\partial x_l^2}\delta_{im}\delta_{jl}-\frac{\partial^2 A_l}{\partial x_l\partial x_m}\delta_{im}\delta_{jl}-\frac{\partial^2 A_m}{\partial x_m\partial x_l}\delta_{il}\delta_{jm}\right],$$

$$\begin{aligned}\sum_{i,j}\hat{x}_i\frac{\partial}{\partial x_j}\left(\frac{\partial}{\partial\left(\partial A_i/\partial x_j\right)}\right)(\nabla\times A)^2&=2\sum_{i,j}\hat{x}_i\left[\frac{\partial^2 A_i}{\partial x_j^2}-\frac{\partial^2 A_j}{\partial x_i\partial x_j}\right]=\\&=2\sum_j\frac{\partial^2}{\partial x_j^2}\sum_i\hat{x}_iA_i-2\sum_i\hat{x}_i\frac{\partial}{\partial x_i}\sum_j\frac{\partial A_j}{\partial x_j}=2\left[\nabla^2A-\nabla(\nabla\cdot A)\right]=-2\nabla\times(\nabla\times A)\end{aligned} \tag{A.6}$$

We also have

$$\frac{\partial L}{\partial A_i}=\frac{1}{2m_s}\left[\frac{2e_s^2}{c^2}|\psi|^2A_i+\frac{i\hbar e_s}{c}\left(\psi^*\frac{\partial\psi}{\partial x_i}-\psi\frac{\partial\psi^*}{\partial x_i}\right)\right],$$

$$\begin{aligned}\frac{\partial L}{\partial A} &= \frac{1}{2m_s}\left[\frac{2e_s^2}{c^2}|\psi|^2 A + \frac{i\hbar e_s}{c}\left(\psi^*\nabla\psi - \psi\nabla\psi^*\right)\right] = \\ &= \frac{e_s^2}{m_s c^2}|\psi|^2 A + \frac{i\hbar e_s}{2m_s c}\left(\psi^*\nabla\psi - \psi\nabla\psi^*\right)\end{aligned} \tag{A.7}$$

We combine (A.7) with (A.6) to obtain the second GL equation,

$$\frac{c}{4\pi}\nabla\times\left(\nabla\times \boldsymbol{A}\right) + \frac{e_s^2}{m_s c^2}|\psi|^2 A + \frac{i\hbar e_s}{2m_s c}\left(\psi^*\nabla\psi - \psi\nabla\psi^*\right) = 0. \tag{A.8}$$

From Ampere's law,

$$\nabla\times\left(\nabla\times \boldsymbol{A}\right) = \nabla\times\boldsymbol{B} = \frac{4\pi}{c}\boldsymbol{J},$$

we can write equation (A.8) as

$$\boldsymbol{J} = -\frac{e_s^2}{m_s}|\psi|^2 A - \frac{i\hbar e_s}{2m_s}\left(\psi^*\nabla\psi - \psi\nabla\psi^*\right).$$

Again, using the London gauge ($\nabla\cdot\boldsymbol{A} = 0$) we can write the second GL equation as

$$-\frac{c}{4\pi}\nabla^2\boldsymbol{A}^2 + \frac{e_s^2}{m_s}|\psi|^2 A + \frac{i\hbar e_s}{2m_s}\left(\psi^*\nabla\psi - \psi\nabla\psi^*\right) = 0,$$

where the first term follows from the line preceding (A.8)

Appendix B Nonlinear term approximation in fully implicit method

The approximation

$$N\left(\psi^{n+1}\right)=\tau\psi^{n+1}-\left|\psi^{n+1}\right|^{2}\psi^{n+1}\approx\frac{1}{\Delta t}\left(S\left(\psi^{n}\right)-\psi^{n}\right), \tag{B.1}$$

where S is a nonlinear map,

$$S(\psi)=\frac{\tau^{1/2}\psi}{\left[|\psi|^{2}+\left(\tau-|\psi|^{2}\right)\exp\left(-2\tau\,\Delta t\right)\right]^{1/2}} \tag{B.2}$$

is suggested by semigroup theory. Symbolically,

$$N(\psi)=\lim_{\Delta t\to 0}\frac{S(\psi)-\psi}{\Delta t}. \tag{B.3}$$

To find the expression for the "semigroup" S, we start from the continuous TDGL equations (zero-electric potential gauge, $\Phi=0$), using the polar representation $\psi=|\psi|\,e^{i\phi}$,

$$\partial_t|\psi|=\Delta|\psi|-|\psi|\left|\nabla\psi-\kappa^{-1}\mathbf{A}\right|^{2}+\tau|\psi|-|\psi|^{3}, \tag{B.4}$$

$$|\psi|\partial_t\phi=2\left(\nabla|\psi|\right)\cdot\left(\nabla\phi-\kappa^{-1}\mathbf{A}\right)+|\psi|\nabla\cdot\left(\nabla\phi-\kappa^{-1}\mathbf{A}\right), \tag{B.5}$$

$$\sigma\partial_t\mathbf{A}=-\nabla\times\nabla\times\mathbf{A}+\kappa^{-1}|\psi|^{2}\left(\nabla\phi-\kappa^{-1}\mathbf{A}\right). \tag{B.6}$$

At this point, we are interested in the effect of the nonlinear term $|\psi|^3$ on the dynamics. To highlight this effect, we concentrate on the time evolution of the scalar $u = |\psi|$ and the vector $v = \nabla\phi - \kappa^{-1}\mathbf{A}$. (In physical terms, u^2 is the density of superconducting charge carriers, while $u^2 v$ is κ times the supercurrent density.) Ignoring their spatial variations, we have a dynamic system,

$$u' = -u|v|^2 + \tau u - u^3, \tag{B.7}$$

$$v' = -\varepsilon u^2 v, \tag{B.8}$$

where $'$ denotes differentiation with respect to t, and $\varepsilon = (\kappa^2\sigma)^{-1}$. This system yields a pair of ordinary differential equations for the scalars $x = u^2$ and $y = |v|^2$,

$$x' = 2x(\tau - x - y), \tag{B.9}$$

$$y' = -2\varepsilon xy. \tag{B.10}$$

If κ is large, ε is small, and the dynamics are readily analyzed. To leading order, y is constant; $y = 0$ is the only meaningful choice. (Recall that $xy^{1/2}$ is κ times the magnitude of the supercurrent density.) Then the dynamics of x are given by

$$x' = 2x(\tau - x). \tag{B.11}$$

We integrate this equation from $t = t_n$ to t,

$$x(t) = \frac{\tau x(t_n)}{x(t_n) + (\tau - x(t_n))\exp(-2\tau(t - t_n))}. \tag{B.12}$$

In particular,

$$x(t_{n+1}) = \frac{\tau x(t_n)}{x(t_n) + (\tau - x(t_n))\exp(-2\tau\Delta t)}, \tag{B.13}$$

where $\Delta t = t_{n+1} - t_n$. Since $x(t_n) = |\psi_n|^{1/2}$ and $x(t_{n+1}) = |\psi_{n+1}|^{1/2}$, it follows that

$$\left|\psi_{n+1}\right| = \frac{\tau^{1/2}\left|\psi_n\right|}{\left[\left|\psi_n\right|^2 + \left(\tau - \left|\psi_n\right|^2\right)\exp\left(-2\tau\Delta t\right)\right]^{1/2}}. \tag{B.14}$$

The phase ϕ of ψ is constant in time. If we multiply both sides by $e^{i\phi}$, we obtain the expression for the "semigroup" S:

$$S(\psi) = \frac{\tau^{1/2}\psi}{\left[\left|\psi\right|^2 + \left(\tau - \left|\psi\right|^2\right)\exp\left(-2\tau\,\Delta t\right)\right]^{1/2}}. \tag{B.15}$$

Appendix C Complete Algorithm of Numerical Solution of the TDGL Equations in 2D

Below is the complete algorithm of numerical solution of the time-dependent Ginzburg-Landau equations using fully implicit method written in C++ programming language.

```
//////////////////////////////////////////////////////////////////////////////////////////
//
//   TDGL2D.cpp - Solves TDGL equations in 2D
//
//   (c)2000-2004 Yuri Artemov
//
//////////////////////////////////////////////////////////////////////////////////////////

#include <math.h>

#define ARRAY2(Pointer, i1, i2, N1)         *((Pointer) + (i1) + (i2)*(N1))
#define ARRAY3(Pointer, i1, i2, i3, N1, N2) *((Pointer) + (i1) + ((i2) + (i3)*(N2))*(N1))

typedef struct {
   double Re;
   double Im;
} COMPLEXD, *PCOMPLEXD;


// parameters
int Nx = 100, Ny = 100, Nt = 20;
bool bPeriodicY = true;
double Lx = 50.0, Ly = 50.0, Lt = 20.0;
double k = 10.0, H = 3.0, I = 0.0, dt = 0.1;
int ixs = 0, ixy = 0;


// main function; called with sequentially increasing it from 0 to Nt-1; matrices Psi, Ax, Ay, B,
// Jx, Jy, Ex, Ey (all Nx by Ny) and scalars V, R, Ba, M, L, Lc, Lk, Lm are the output

void DoTDGLStep(int it) {

   int ix, iy;

   int i, j, Ndt;
   Ndt = max(1, (int)ceil(Lt/Nt/dt/2.0)); // factor 2 because we integrate dt twice
   dt = Lt/Nt/Ndt/2.0; // adjust dt
   double Hl, Hr;
   double hx = Lx/Nx, hy = Ly/Ny;
   static double sigma = 1.0/k/k,
      coeffUx = hx/k, coeffUy = hy/k,
      coeffJx = 1.0/k/hx, coeffJy = 1.0/k/hy,
      betaxPsi = dt/hx/hx, betayPsi = dt/hy/hy,
      alphaxPsi = 1.0 + 2.0*betaxPsi, alphayPsi = 1.0 + 2.0*betayPsi,
      betaxA = dt/hx/hx, betayA = dt/hy/hy,
      betaxyA = dt/hx/hy,
      alphaxA = sigma + 2.0*betaxA, alphayA = sigma + 2.0*betayA;
   static double n, V = 0.0, R = 0.0, Ba = 0.0, M = 0.0, L = 0.0, Lc = 0.0, Lk = 0.0, Lm = 0.0;
   int idt, idir;
```

```
static COMPLEXD *uc, *ac, *bc, *cc, *dc, *Cc, *Dc;
static double   *ud, *ad, *bd, *cd, *dd, *Cd, *Dd;
static COMPLEXD *Psi, *Ux, *Uy;
static double   *Ax, *Ay, *Ax0, *B, *Jx, *Jy, *Ex, *Ey, *tau;
const COMPLEXD  cfZero = {0.0, 0.0}, cfOne = {1.0, 0.0};
COMPLEXD cf1, cf2, cf3, cf4, cf5, cf6, cf7, cf8, *pcf1, *pcf2;
bool b1, b2;
int i1, i2, i3, i4;
double f1;

/////////////////////////////////////////////////////////////////////////////////////////
// Initialization
/////////////////////////////////////////////////////////////////////////////////////////

if (it == 0) {
    uc  = new COMPLEXD [max(Nx, Ny)];
    ac  = new COMPLEXD [max(Nx, Ny)];
    bc  = new COMPLEXD [max(Nx, Ny)];
    cc  = new COMPLEXD [max(Nx, Ny)];
    dc  = new COMPLEXD [max(Nx, Ny)];
    Cc  = new COMPLEXD [max(Nx, Ny)];
    Dc  = new COMPLEXD [max(Nx, Ny)];
    ud  = new double [max(Nx, Ny)];
    ad  = new double [max(Nx, Ny)];
    bd  = new double [max(Nx, Ny)];
    cd  = new double [max(Nx, Ny)];
    dd  = new double [max(Nx, Ny)];
    Cd  = new double [max(Nx, Ny)];
    Dd  = new double [max(Nx, Ny)];
    Psi = new COMPLEXD [Nx*Ny];
    Ux  = new COMPLEXD [Nx*Ny];
    Uy  = new COMPLEXD [Nx*Ny];
    Ax  = new double [Nx*Ny];
    Ay  = new double [Nx*Ny];
    Ax0 = new double [Nx*Ny]; // Ax at previous half-timestep
    B   = new double [Nx*Ny];
    Jx  = new double [Nx*Ny];
    Jy  = new double [Nx*Ny];
    Ex  = new double [Nx*Ny];
    Ey  = new double [Nx*Ny];
    tau = new double [Nx*Ny];

    for (iy = 0; iy < Ny; iy++) {
        for (ix = 0; ix < Nx; ix++) {
            *PA2(Psi, ix, iy, Nx) = cfOne;
            *PA2(Ax, ix, iy, Nx) = 0.0;
            *PA2(Ay, ix, iy, Nx) = 0.0;
            *PA2(B, ix, iy, Nx) = 0.0;
            *PA2(Jx, ix, iy, Nx) = 0.0;
            *PA2(Jy, ix, iy, Nx) = 0.0;
            *PA2(Ex, ix, iy, Nx) = 0.0;
            *PA2(Ey, ix, iy, Nx) = 0.0;
            *PA2(tau, ix, iy, Nx) = 1.0;
        }
    }

    for (iy = 0; iy < Ny; iy++) {
        for (ix = 0; ix < ixs; ix++) {
            *PA2(Psi, ix, iy, Nx) = cfZero;
            *PA2(tau, ix, iy, Nx) = 0.0;
        }
        for (ix = Nx-ixs; ix < Nx; ix++) {
            *PA2(Psi, ix, iy, Nx) = cfZero;
            *PA2(tau, ix, iy, Nx) = 0.0;
        }
    }

    if (!bPeriodicY) {
        for (ix = 0; ix < Nx; ix++) {
            for (iy = 0; iy < iys; iy++) {
                *PA2(Psi, ix, iy, Nx) = cfZero;
                *PA2(tau, ix, iy, Nx) = 0.0;
            }
            for (iy = Ny-iys; iy < Ny; iy++) {
                *PA2(Psi, ix, iy, Nx) = cfZero;
                *PA2(tau, ix, iy, Nx) = 0.0;
            }
        }
    }
} //Initialization

/////////////////////////////////////////////////////////////////////////////////////////
// Timesteps
/////////////////////////////////////////////////////////////////////////////////////////

for (idt = 0; idt < Ndt; idt++) {
    H1 = H + I/2.0;
```

```
Hr = H - I/2.0;

for (idir = 1; idir <= 2; idir++) { // Two steps in ADI
    //////////////////////////////////////////////////////////////////////////////////
    // Ux
    //////////////////////////////////////////////////////////////////////////////////

    for (iy = 0; iy < Ny; iy++) {
        for (ix = 0; ix < Nx; ix++) {
            pcf1 = PA2(Ux, ix, iy, Nx);
            f1 = coeffUx*A2(Ax, ix, iy, Nx);
            pcf1->Re =  cos(f1);
            pcf1->Im = -sin(f1);
        }
    }

    //////////////////////////////////////////////////////////////////////////////////
    // Uy
    //////////////////////////////////////////////////////////////////////////////////

    for (iy = 0; iy < Ny; iy++) {
        for (ix = 0; ix < Nx; ix++) {
            pcf1 = PA2(Uy, ix, iy, Nx);
            f1 = coeffUy*A2(Ay, ix, iy, Nx);
            pcf1->Re =  cos(f1);
            pcf1->Im = -sin(f1);
        }
    }

    //////////////////////////////////////////////////////////////////////////////////
    // Jx
    //////////////////////////////////////////////////////////////////////////////////

    for (iy = (bPeriodicY? 0 : iys); iy < (bPeriodicY? Ny : Ny-iys); iy++) {
        for (ix = ixs+1; ix < Nx-ixs-2; ix++) {
            cf1 = A2(Ux, ix, iy, Nx);
            cf2 = A2(Psi, ix, iy, Nx);
            cf3 = A2(Psi, ix+1, iy, Nx);
            *PA2(Jx, ix, iy, Nx) = coeffJx*((cf1.Im*cf2.Re - cf1.Re*cf2.Im)*cf3.Re +
                (cf1.Re*cf2.Re + cf1.Im*cf2.Im)*cf3.Im);
        }
    }

    //////////////////////////////////////////////////////////////////////////////////
    // Jy
    //////////////////////////////////////////////////////////////////////////////////

    for (iy = (bPeriodicY? 0 : iys+1); iy < (bPeriodicY? Ny : Ny-iys-2); iy++) {
        b1 = (iy == Ny-1)? TRUE : FALSE;
        for (ix = ixs; ix < Nx-ixs; ix++) {
            cf1 = A2(Uy, ix, iy, Nx);
            cf2 = A2(Psi, ix, iy, Nx);
            cf3 = A2(Psi, ix, b1? 0 : iy+1, Nx);
            *PA2(Jy, ix, iy, Nx) = coeffJy*((cf1.Im*cf2.Re - cf1.Re*cf2.Im)*cf3.Re +
                (cf1.Re*cf2.Re + cf1.Im*cf2.Im)*cf3.Im);
        }
    }


    //////////////////////////////////////////////////////////////////////////////////
    // 1st half timestep
    //////////////////////////////////////////////////////////////////////////////////

    if (idir == 1) {
        i1 = Nx - 2*ixs - 1;
        i2 = i1 + 1;
        i3 = Ny - 1;

        //////////////////////////////////////////////////////////////////////////////
        // Psi: X-step
        //////////////////////////////////////////////////////////////////////////////

        for (iy = (bPeriodicY? 0 : iys+1); iy < (bPeriodicY? Ny : Ny-iys-1); iy++) {
            // Coefficients
            i4 = iy - 1;
            b1 = (iy==i3)? TRUE : FALSE;
            b2 = (iy==0)? TRUE : FALSE;
            cf1 = A2(Ux, ixs, iy, Nx);
            ac[0] = cfZero; // index 0 corresponds to ix=ixs
            bc[0] = cfOne;
            cc[0].Re = -cf1.Re;
            cc[0].Im = -cf1.Im;
            dc[0] = cfZero;
            for (ix = ixs+1; ix < Nx-ixs-1; ix++) {
                i = ix-ixs;
                cf1 = A2(Ux, ix-1, iy, Nx);
```

```
            cf2 = A2(Psi, ix, iy, Nx);
            cf3 = A2(Ux, ix, iy, Nx);
            cf4 = A2(Uy, ix, iy, Nx);
            cf5 = A2(Psi, ix, b1? 0 : iy+1, Nx);
            cf6 = A2(Uy, ix, b2? i3 : i4, Nx);
            cf7 = A2(Psi, ix, b2? i3 : i4, Nx);
            ac[i].Re = -betaxPsi*cf1.Re;
            ac[i].Im =  betaxPsi*cf1.Im;
            bc[i].Re = alphaxPsi - (sqrt(A2(tau, ix, iy, Nx) /
                (Abs2(cf2) + (A2(tau, ix, iy, Nx) - Abs2(cf2))*
                exp(-2*dt*A2(tau, ix, iy, Nx)))) - 1.0);
            bc[i].Im = 0.0;
            cc[i].Re = -betaxPsi*cf3.Re;
            cc[i].Im = -betaxPsi*cf3.Im;
            dc[i].Re = cf2.Re + betayPsi*(cf4.Re*cf5.Re - cf4.Im*cf5.Im -
                2.0*cf2.Re + cf6.Re*cf7.Re + cf6.Im*cf7.Im);
            dc[i].Im = cf2.Im + betayPsi*(cf4.Re*cf5.Im + cf4.Im*cf5.Re -
                2.0*cf2.Im + cf6.Re*cf7.Im - cf6.Im*cf7.Re);
        }
        cf1 = A2(Ux, Nx-ixs-2, iy, Nx);
        ac[i1].Re = -cf1.Re; // Nx-2*ixs-1 corresponds to ix=Nx-ixs-1
        ac[i1].Im =  cf1.Im;
        bc[i1] = cfOne;
        cc[i1] = cfZero;
        dc[i1] = cfZero;

        // Solve 3-band matrix
        Solve3Diag(uc, ac, bc, cc, dc, Cc, Dc, i2);
        for (ix = ixs; ix < Nx-ixs; ix++) {
            *PA2(Psi, ix, iy, Nx) = uc[ix-ixs];
        }
    }

    if (!bPeriodicY) { // Bottom and top SC boundaries
        for (ix = ixs; ix < Nx-ixs; ix++) {
            pcf1 = PA2(Psi, ix, iys, Nx);
            pcf2 = PA2(Psi, ix, Ny-iys-1, Nx);
            cf1 = A2(Uy, ix, iys, Nx);
            cf2 = A2(Psi, ix, iys+1, Nx);
            cf3 = A2(Uy, ix, Ny-iys-2, Nx);
            cf4 = A2(Psi, ix, Ny-iys-2, Nx);
            pcf1->Re = cf1.Re*cf2.Re - cf1.Im*cf2.Im;
            pcf1->Im = cf1.Re*cf2.Im + cf1.Im*cf2.Re;
            pcf2->Re = cf3.Re*cf4.Re + cf3.Im*cf4.Im;
            pcf2->Im = cf3.Re*cf4.Im - cf3.Im*cf4.Re;
        }
    }
} // 1st half timestep

///////////////////////////////////////////////////////////////////////////////////
// 2nd half timestep
///////////////////////////////////////////////////////////////////////////////////

if (idir == 2) {
    i1 = Ny - 2*iys - 1;
    i2 = i1 + 1;
    i3 = Nx - 1;

    ///////////////////////////////////////////////////////////////////////////////
    // Psi: Y-step
    ///////////////////////////////////////////////////////////////////////////////

    for (ix = ixs+1; ix < Nx-ixs-1; ix++) { // SC bulk
        // Coefficients
        i4 = ix - 1;
        if (bPeriodicY) { // Periodic boundary in Y direction
            cf1 = A2(Psi, ix, 0, Nx);
            cf2 = A2(Uy, ix, 0, Nx);
            cf3 = A2(Ux, ix, 0, Nx);
            cf4 = A2(Psi, ix+1, 0, Nx);
            cf5 = A2(Ux, i4, 0, Nx);
            cf6 = A2(Psi, i4, 0, Nx);
            cf7 = A2(Uy, ix, Ny-1, Nx);
            cf8 = A2(Psi, ix, Ny-1, Nx);
            ac[0] = cfZero; // index 0 corresponds to iy=0
            bc[0].Re = alphayPsi - (sqrt(A2(tau, ix, 0, Nx) /
                (Abs2(cf1) + (A2(tau, ix, 0, Nx) - Abs2(cf1))*
                exp(-2*dt*A2(tau, ix, 0, Nx)))) - 1.0);
            bc[0].Im = 0.0;
            cc[0].Re = -betayPsi*cf2.Re;
            cc[0].Im = -betayPsi*cf2.Im;
            dc[0].Re = cf1.Re + betaxPsi*(cf3.Re*cf4.Re - cf3.Im*cf4.Im -
                2.0*cf1.Re + cf5.Re*cf6.Re + cf5.Im*cf6.Im) +
                betayPsi*(cf7.Re*cf8.Re + cf7.Im*cf8.Im); // instead of iy=-1
            dc[0].Im = cf1.Im + betaxPsi*(cf3.Re*cf4.Im + cf3.Im*cf4.Re -
                2.0*cf1.Im + cf5.Re*cf6.Im - cf5.Im*cf6.Re) +
```

```
            betayPsi*(cf7.Re*cf8.Im - cf7.Im*cf8.Re);
    }
    else { // Non-periodic boundaries
        cf1 = A2(Uy, ix, iys, Nx);
        ac[0] = cfZero; // index 0 corresponds to iy=iys
        bc[0] = cfOne;
        cc[0].Re = -cf1.Re;
        cc[0].Im = -cf1.Im;
        dc[0] = cfZero;
    }
    for (iy=(bPeriodicY? 1:iys+1); iy<(bPeriodicY? Ny-1:Ny-iys-1); iy++) {
        i = bPeriodicY? iy : iy-iys;
        cf1 = A2(Uy, ix, iy-1, Nx);
        cf2 = A2(Psi, ix, iy, Nx);
        cf3 = A2(Uy, ix, iy, Nx);
        cf4 = A2(Ux, ix, iy, Nx);
        cf5 = A2(Psi, ix+1, iy, Nx);
        cf6 = A2(Ux, i4, iy, Nx);
        cf7 = A2(Psi, i4, iy, Nx);
        ac[i].Re = -betayPsi*cf1.Re;
        ac[i].Im =  betayPsi*cf1.Im;
        bc[i].Re = alphayPsi - (sqrt(A2(tau, ix, iy, Nx) /
            (Abs2(cf2) + (A2(tau, ix, iy, Nx) - Abs2(cf2))*
            exp(-2*dt*A2(tau, ix, iy, Nx)))) - 1.0);
        bc[i].Im = 0.0;
        cc[i].Re = -betayPsi*cf3.Re;
        cc[i].Im = -betayPsi*cf3.Im;
        dc[i].Re = cf2.Re + betaxPsi*(cf4.Re*cf5.Re - cf4.Im*cf5.Im -
            2.0*cf2.Re + cf6.Re*cf7.Re + cf6.Im*cf7.Im);
        dc[i].Im = cf2.Im + betaxPsi*(cf4.Re*cf5.Im + cf4.Im*cf5.Re -
            2.0*cf2.Im + cf6.Re*cf7.Im - cf6.Im*cf7.Re);
    }
    if (bPeriodicY) { // Periodic boundary in Y direction
        i = Ny - 1;
        cf1 = A2(Uy, ix, i-1, Nx);
        cf2 = A2(Psi, ix, i, Nx);
        cf3 = A2(Ux, ix, i, Nx);
        cf4 = A2(Psi, ix+1, i, Nx);
        cf5 = A2(Ux, ix-1, i, Nx);
        cf6 = A2(Psi, ix-1, i, Nx);
        cf7 = A2(Uy, ix, i, Nx);
        cf8 = A2(Psi, ix, 0, Nx);
        ac[i].Re = -betayPsi*cf1.Re; // iy=Ny-1
        ac[i].Im =  betayPsi*cf1.Im;
        bc[i].Re = alphayPsi - (sqrt(A2(tau, ix, i, Nx) /
            (Abs2(cf2) + (A2(tau, ix, i, Nx) - Abs2(cf2))*
            exp(-2*dt*A2(tau, ix, i, Nx)))) - 1.0);
        bc[i].Im = 0.0;
        cc[i] = cfZero;
        dc[i].Re = cf2.Re + betaxPsi*(cf3.Re*cf4.Re - cf3.Im*cf4.Im -
            2.0*cf2.Re + cf5.Re*cf6.Re + cf5.Im*cf6.Im) +
            betayPsi*(cf7.Re*cf8.Re - cf7.Im*cf8.Im); // instead of iy=Ny
        dc[i].Im = cf2.Im + betaxPsi*(cf3.Re*cf4.Im + cf3.Im*cf4.Re -
            2.0*cf2.Im + cf5.Re*cf6.Im - cf5.Im*cf6.Re) +
            betayPsi*(cf7.Re*cf8.Im + cf7.Im*cf8.Re);
    }
    else {
        cf1 = A2(Uy, ix, Ny-iys-2, Nx);
        ac[i1].Re = -cf1.Re; // Ny-2*iys-1 corresponds to iy=Ny-iys-1
        ac[i1].Im =  cf1.Im;
        bc[i1] = cfOne;
        cc[i1] = cfZero;
        dc[i1] = cfZero;
    }

    // Solve 3-band matrix
    if (bPeriodicY) {
        Solve3Diag(uc, ac, bc, cc, dc, Cc, Dc, Ny);
        for (iy = 0; iy < Ny; iy++)
            *PA2(Psi, ix, iy, Nx) = uc[iy];
    }
    else {
        Solve3Diag(uc, ac, bc, cc, dc, Cc, Dc, i2);
        for (iy = iys; iy < Ny-iys; iy++)
            *PA2(Psi, ix, iy, Nx) = uc[iy-iys];
    }
}

// Left and right SC boundaries
for (iy = (bPeriodicY? 0 : iys); iy < (bPeriodicY? Ny : Ny-iys); iy++) {
    pcf1 = PA2(Psi, ixs, iy, Nx);
    pcf2 = PA2(Psi, Nx-ixs-1, iy, Nx);
    cf1 = A2(Ux, ixs, iy, Nx);
    cf2 = A2(Psi, ixs+1, iy, Nx);
    cf3 = A2(Ux, Nx-ixs-2, iy, Nx);
    cf4 = A2(Psi, Nx-ixs-2, iy, Nx);
    pcf1->Re = cf1.Re*cf2.Re - cf1.Im*cf2.Im;
```

```
        pcf1->Im = cf1.Re*cf2.Im + cf1.Im*cf2.Re;
        pcf2->Re = cf3.Re*cf4.Re + cf3.Im*cf4.Im;
        pcf2->Im = cf3.Re*cf4.Im - cf3.Im*cf4.Re;
    }
} // 2nd half timestep

// copy Ax to Ax0 - we need old Ax for Ay, for uniformity in nonperiodic case
memcpy(Ax0, Ax, Nx*Ny*sizeof(double));

///////////////////////////////////////////////////////////////////////////////////
// Ax: Y-step
///////////////////////////////////////////////////////////////////////////////////

i1 = Ny - 1;
for (ix = 0; ix < Nx-1; ix++) { // The whole region (SC+N)
    // Coefficients
    if (bPeriodicY) { // Periodic boundary in Y direction
        ad[0] = 0.0; // index 0 corresponds to iy=0
        bd[0] = alphayA;
        cd[0] = -betayA;
        dd[0] = sigma*A2(Ax, ix, 0, Nx) + dt*A2(Jx, ix, 0, Nx) +
            betaxyA*(A2(Ay, ix, 0, Nx) - A2(Ay, ix+1, 0, Nx) -
            A2(Ay, ix, i1, Nx) + A2(Ay, ix+1, i1, Nx)) + betayA*A2(Ax, ix, i1, Nx);
    }
    else {
        ad[0] = 0.0; // index 0 corresponds to iy=0
        bd[0] = 1.0;
        cd[0] = -1.0;
        dd[0] = (ix == 0 || ix == Nx-2? hy*H/2.0 : hy*H);
    }
    for (iy = 1; iy < i1; iy++) {
        ad[iy] = -betayA;
        bd[iy] = alphayA;
        cd[iy] = ad[iy];
        dd[iy] = sigma*A2(Ax, ix, iy, Nx) + dt*A2(Jx, ix, iy, Nx) +
            betaxyA*(A2(Ay, ix, iy, Nx) - A2(Ay, ix+1, iy, Nx) -
            A2(Ay, ix, iy-1, Nx) + A2(Ay, ix+1, iy-1, Nx));
    }
    if (bPeriodicY) {
        ad[i1] = -betayA; // index Ny-1 corresponds to iy=Ny-1
        bd[i1] = alphayA;
        cd[i1] = 0.0;
        dd[i1] = sigma*A2(Ax, ix, i1, Nx) + dt*A2(Jx, ix, i1, Nx) +
            betaxyA*(A2(Ay, ix, i1, Nx) - A2(Ay, ix+1, i1, Nx) -
            A2(Ay, ix, i1-1, Nx) + A2(Ay, ix+1, i1-1, Nx)) +
            betayA*A2(Ax, ix, 0, Nx);
    }
    else {
        ad[i1] = -1.0;
        bd[i1] = 1.0;
        cd[i1] = 0.0;
        dd[i1] = (ix == 0 || ix == Nx-2? -hy*H/2.0 : -hy*H);
    }

    // Solve 3-band matrix
    Solve3Diag(ud, ad, bd, cd, dd, Cd, Dd, Ny);
    for (iy = 0; iy < Ny; iy++) {
        *PA2(Ax, ix, iy, Nx) = ud[iy];
    }
}

///////////////////////////////////////////////////////////////////////////////////
// Ay: X-step
///////////////////////////////////////////////////////////////////////////////////

i1 = Nx - 1;
for (iy = 0; iy < (bPeriodicY? Ny : Ny-1); iy++) { // The whole region (SC+N)
    // Coefficients
    b1 = (iy==Ny-1)? TRUE : FALSE;
    if (bPeriodicY) { // Periodic boundary in Y direction
        ad[0] = 0.0; // index 0 corresponds to ix=0
        bd[0] = 1.0;
        cd[0] = -1.0;
        dd[0] = -hx*H1;
    }
    else { // Non-periodic boundaries
        ad[0] = 0.0; // index 0 corresponds to ix=0
        bd[0] = 1.0;
        cd[0] = -1.0;
        dd[0] = (iy == 0 || iy == Ny-2? -hx*H/2.0 : -hx*H);
    }
    for (ix = 1; ix < i1; ix++) {
        ad[ix] = -betaxA;
        bd[ix] = alphaxA;
        cd[ix] = ad[ix];
        dd[ix] = sigma*A2(Ay, ix, iy, Nx) + dt*A2(Jy, ix, iy, Nx) + betaxyA*
            (bPeriodicY?
```

```
                    (A2(Ax, ix, iy, Nx) - A2(Ax, ix, b1? 0 : iy+1, Nx) -
                    A2(Ax, ix-1, iy, Nx) + A2(Ax, ix-1, b1? 0 : iy+1, Nx))
                    :
                    (A2(Ax0, ix, iy, Nx) - A2(Ax0, ix, iy+1, Nx) -
                    A2(Ax0, ix-1, iy, Nx) + A2(Ax0, ix-1, iy+1, Nx)));
            }
            if (bPeriodicY) {
                ad[i1] = -1.0;
                bd[i1] = 1.0;
                cd[i1] = 0.0;
                dd[i1] = hx*Hr;
            }
            else {
                ad[i1] = -1.0;
                bd[i1] = 1.0;
                cd[i1] = 0.0;
                dd[i1] = (iy == 0 || iy == Ny-2? hx*H/2.0 : hx*H);
            }

            // Solve 3-band matrix
            Solve3Diag(ud, ad, bd, cd, dd, Cd, Dd, Nx);
            for (ix = 0; ix < Nx; ix++) {
                *PA2(Ay, ix, iy, Nx) = ud[ix];
            }
        }
    } // Two steps in ADI
} // Timesteps

//////////////////////////////////////////////////////////////////////////////////////////////////////
// B
//////////////////////////////////////////////////////////////////////////////////////////////////////

for (iy = 0; iy < (bPeriodicY? Ny : Ny-1); iy++) {
    b1 = (iy==Ny-1)? TRUE : FALSE;
    for (ix = 0; ix < Nx-1; ix++) {
        *PA2(B, ix, iy, Nx) =
            (A2(Ay, ix+1, iy, Nx) - A2(Ay, ix, iy, Nx))/hx -
            (A2(Ax, ix, b1? 0 : iy+1, Nx) - A2(Ax, ix, iy, Nx))/hy;
    }
    *PA2(B, Nx-1, iy, Nx) = Hr; // undetermined right boundary
    if (!bPeriodicY) {
        for (ix = 0; ix < Nx; ix++) {
            *PA2(B, ix, Ny-1, Nx) = H; // undetermined upper boundary
        }
    }
}

//////////////////////////////////////////////////////////////////////////////////////////////////////
// Ex
//////////////////////////////////////////////////////////////////////////////////////////////////////

for (iy = 0; iy < Ny; iy++) {
    for (ix = 0; ix < Nx; ix++) {
        *PA2(Ex, ix, iy, Nx) = -1.0/sigma*(A2(Jx, ix, iy, Nx) - (A2(B, ix, iy, Nx) -
            (iy==0? (bPeriodicY? A2(B, ix, Ny-1, Nx) : H) : A2(B, ix, iy-1, Nx)))/hy);
    }
}

//////////////////////////////////////////////////////////////////////////////////////////////////////
// Ey
//////////////////////////////////////////////////////////////////////////////////////////////////////

for (iy = 0; iy < Ny; iy++) {
    for (ix = 0; ix < Nx; ix++) {
        *PA2(Ey, ix, iy, Nx) = -1.0/sigma*(A2(Jy, ix, iy, Nx) + (A2(B, ix, iy, Nx) -
            (ix==0? Hl : A2(B, ix-1, iy, Nx)))/hx);
    }
}

//////////////////////////////////////////////////////////////////////////////////////////////////////
// V - Voltage (for periodic only)
//////////////////////////////////////////////////////////////////////////////////////////////////////

if (bPeriodicY) {
    for (ix = ixs; ix < Nx-ixs; ix++) {
        for (iy = 0; iy < Ny; iy++) {
            V += A2(Ey, ix, iy, Nx);
        }
    }
    V *= hy/(Nx-2*ixs); // average over x
}

//////////////////////////////////////////////////////////////////////////////////////////////////////
// R - Resistance (for periodic only)
//////////////////////////////////////////////////////////////////////////////////////////////////////
```

```
    if (bPeriodicY) {
        if (I != 0.0)
            R = V/I;
    }

    /////////////////////////////////////////////////////////////////////////////////////////////
    // M - Magnetization (more exactly, -4*pi*M = H - <B>)
    /////////////////////////////////////////////////////////////////////////////////////////////

    for (iy = 0; iy < (bPeriodicY? Ny : Ny-1); iy++) {
        for (ix = 0; ix < Nx-1; ix++) {
            Ba += A2(B, ix, iy, Nx);
        }
    }
    Ba /= (Nx-1)*(bPeriodicY? Ny : Ny-1); // <B>
    M = H - Ba; // we're interested in flux expulsion, -4*pi*M = H - <B>

    /////////////////////////////////////////////////////////////////////////////////////////////
    // L, Lc, Lk, Lm - Energy and its parts
    // Note: we integrate the whole SC region for Lc and Lk, since in N psi=0 anyway
    /////////////////////////////////////////////////////////////////////////////////////////////

    for (iy = 0; iy < (bPeriodicY? Ny : Ny-1); iy++) {
        b1 = (iy == Ny-1)? TRUE : FALSE;
        for (ix = 0; ix < Nx-1; ix++) {
            // Condensation energy
            n = Abs2(A2(Psi, ix, iy, Nx));
            Lc += -n*A2(tau, ix, iy, Nx) + n*n/2.0;
            // Kinetic energy
            cf1.Re = A2(Ux, ix, iy, Nx).Re*A2(Psi, ix+1, iy, Nx).Re -
                A2(Ux, ix, iy, Nx).Im*A2(Psi, ix+1, iy, Nx).Im - A2(Psi, ix, iy, Nx).Re;
            cf1.Im = A2(Ux, ix, iy, Nx).Re*A2(Psi, ix+1, iy, Nx).Im +
                A2(Ux, ix, iy, Nx).Im*A2(Psi, ix+1, iy, Nx).Re - A2(Psi, ix, iy, Nx).Im;
            cf2.Re = A2(Uy, ix, iy, Nx).Re*A2(Psi, ix, b1? 0 : iy+1, Nx).Re -
                A2(Uy, ix, iy, Nx).Im*A2(Psi, ix, b1? 0:iy+1, Nx).Im - A2(Psi, ix, iy, Nx).Re;
            cf2.Im = A2(Uy, ix, iy, Nx).Re*A2(Psi, ix, b1? 0 : iy+1, Nx).Im +
                A2(Uy, ix, iy, Nx).Im*A2(Psi, ix, b1? 0:iy+1, Nx).Re - A2(Psi, ix, iy, Nx).Im;
            Lk += Abs2(cf1)/hx/hx + Abs2(cf2)/hy/hy;
            // Magnetic field energy
            Lm += A2(B, ix, iy, Nx)*A2(B, ix, iy, Nx);
        }
    }
    // Normalization
    Lc *= hx*hy;
    Lk *= hx*hy;
    Lm *= hx*hy;
    // Total energy
    L = Lc + Lk + Lm;

    /////////////////////////////////////////////////////////////////////////////////////////////
    // Cleanup
    /////////////////////////////////////////////////////////////////////////////////////////////

    if (it == Nt - 1) {
        delete [] uc;
        delete [] ac;
        delete [] bc;
        delete [] cc;
        delete [] dc;
        delete [] Cc;
        delete [] Dc;
        delete [] ud;
        delete [] ad;
        delete [] bd;
        delete [] cd;
        delete [] dd;
        delete [] Cd;
        delete [] Dd;
        delete [] Psi;
        delete [] Ax;
        delete [] Ay;
        delete [] Ax0;
        delete [] Ux;
        delete [] Uy;
        delete [] B;
        delete [] Jx;
        delete [] Jy;
        delete [] Ex;
        delete [] Ey;
        delete [] tau;
    }
}

inline double A2(double *Pointer, int i1, int i2, int N1) {
    return *(Pointer + i1 + i2*N1);
}
```

```
inline double *PA2(double *Pointer, int i1, int i2, int N1) {
   return (Pointer + i1 + i2*N1);
}

inline COMPLEXD A2(COMPLEXD *Pointer, int i1, int i2, int N1) {
   return *(Pointer + i1 + i2*N1);
}

inline COMPLEXD *PA2(COMPLEXD *Pointer, int i1, int i2, int N1) {
   return (Pointer + i1 + i2*N1);
}

double Abs2(COMPLEXD c) {
   return c.Re*c.Re + c.Im*c.Im;
}

void Solve3Diag(double *u, double *a, double *b, double *c, double *d, double *C, double *D,
                int N) {
   double *u0 = u, *a0 = a, t;

   C[0] = c[0]/b[0];
   D[0] = d[0]/b[0];
   for (int i = 1; i < N; i++) {
      t = b[i] - a[i]*C[i-1];
      C[i] = c[i]/t;
      D[i] = (d[i] - a[i]*D[i-1])/t;
   }

   u[N-1] = D[N-1];
   for (i = N-2; i > -1; i--)
      u[i] = D[i] - C[i]*u[i+1];
}

void Solve3Diag(COMPLEXD *u, COMPLEXD *a, COMPLEXD *b, COMPLEXD *c, COMPLEXD *d,
                COMPLEXD *C, COMPLEXD *D, int N) {
   double d1, d2, d3, d4, d5, d6, d7, d8, d9, d10, d11, d12, d13;

   d1 = b[0].Re;
   d2 = b[0].Im;
   d3 = c[0].Re;
   d4 = c[0].Im;
   d5 = d[0].Re;
   d6 = d[0].Im;
   d7 = d1*d1 + d2*d2;
   C[0].Re = (d3*d1 + d4*d2)/d7;
   C[0].Im = (d4*d1 - d3*d2)/d7;
   D[0].Re = (d5*d1 + d6*d2)/d7;
   D[0].Im = (d6*d1 - d5*d2)/d7;
   for (int i = 1; i < N; i++) {
      d1 = a[i].Re;
      d2 = a[i].Im;
      d3 = C[i-1].Re;
      d4 = C[i-1].Im;
      d5 = b[i].Re - (d1*d3 - d2*d4);
      d6 = b[i].Im - (d1*d4 + d2*d3);
      d7 = c[i].Re;
      d8 = c[i].Im;
      d9  = D[i-1].Re;
      d10 = D[i-1].Im;
      d11 = d[i].Re - (d1*d9  - d2*d10);
      d12 = d[i].Im - (d1*d10 + d2*d9);
      d13 = d5*d5 + d6*d6;
      C[i].Re = (d7*d5 + d8*d6)/d13;
      C[i].Im = (d8*d5 - d7*d6)/d13;
      D[i].Re = (d11*d5 + d12*d6)/d13;
      D[i].Im = (d12*d5 - d11*d6)/d13;
   }

   u[N-1] = D[N-1];
   for (i = N-2; i > -1; i--) {
      d1 = C[i].Re;
      d2 = C[i].Im;
      d3 = u[i+1].Re;
      d4 = u[i+1].Im;
      u[i].Re = D[i].Re - (d1*d3 - d2*d4);
      u[i].Im = D[i].Im - (d1*d4 + d2*d3);
   }
}
```

Glossary

COHERENCE LENGTH (ξ)

A temperature dependent length that represents the minimum distance over which the Ginzburg-Landau order parameter can change significantly.

GINZBURG-LANDAU PARAMETER (κ)

The ratio of the magnetic penetration length to the coherence length which determines whether a superconductor is of type-I or type-II. Since λ and ξ share the same temperature dependence, κ is essentially independent of temperature for a wide range of experimental conditions.

LINK VARIABLE

An integrating factor which is introduced into the time-dependent Ginzburg-Landau equation for the order parameter, which preserves gauge invariance in the discrete form of the equation.

MAGNETIC PENETRATION LENGTH (λ)

A temperature dependent length that determines the extent to which a magnetic field will penetrate into a superconductor.

MEISSNER EFFECT

The exclusion of magnetic flux from the interior of a superconductor.

TWIN BOUNDARY

Dislocation planes commonly found in the high-temperature superconductor YBCO. They form during a cooling stage of the crystal growth process and represent a re-alignment of the a and b crystal axes. The planes lie parallel to the c-axis and divide the crystal into separate domains with a thickness of 500–1500 Å.

VORTEX

A single flux quantum in the mixed state of a type-II superconductor. Named for the similarity with fluid vortices in superfluid ^{3}He; there is a non-vanishing curl associated with the supercurrent density surrounding the vortex.

Bibliography

[1] G. Blatter, M.V. Feigelman, V.B. Geshkenbein, A.I. Larkin, and V.M. Vinokur. Vortices in high temperature superconductors. *Rev. Mod. Phys.*, 66:1125, 1995.

[2] E.H.Brandt. Statics and Dynamics of the Vortex Lattice in High-Tc Superconductors. J. Low Temp. Phys. (2004, in preparation).

[3] V.L. Ginzburg and L.D. Landau. On the theory of superconductivity. *Zh. Eksperim. i Teor. Fiz.*, 20:1064, 1950.

[4] L.P. Gorkov. *Sov. Phys. JETP*, 9:1364, 1959.

[5] A.A. Abrikosov. On the magnetic properties of superconductors of the second group. *Sov. Phys. JETP*, 5:1174, 1957.

[6] Neil Gershenfeld. *The Nature of Mathematical Modeling*. Cambridge University Press, 1999.

[7] A. Schmid. A time dependent Ginzburg-Landau equation and its application to a problem of resistivity in the mixed state. *Phys. Kondens. Materie*, 5:302, 1966.

[8] L.P. Gorkov and G.M. Eliashberg. Generalization of the Ginzburg-Landau equations for nonstationary problems in the case of alloys with paramagnetic impurities. *Sov. Phys. JETP*, 27:328, 1968.

[9] E.H.Brandt. The Vortex Lattice in Superconductors: Phenomenological Theories. Internat. Journal of Modern Physics B, August 2004.

[10] A. Schmid and W. Hauger. On the theory of vortex motion in an inhomogeneous superconducting film. *J. Low Temp. Phys.*, 11:667, 1973.

[11] P. DeGennes. *Superconductivity in Metals and Alloys.* Benjamin, New York, 1966.

[12] M. Tinkham. *Introduction to Superconductivity.* 2nd Ed., McGraw-Hill, New York, 1996.

[13] A.A. Abrikosov. *Fundamentals of the Theory of Metals.* North-Holland, Amsterdam, 1988.

[14] N. Goldenfeld. *Lectures on Phase Transitions and the Renormalization Group.* Addison-Wesley, Reading, MA, 1992.

[15] D.W. Braun, G.W. Crabtree, H.G. Kaper, A.E. Koshelev, G.K. Leaf, D.M. Levine, and V.M. Vinokur. Structure of a moving vortex lattice. *Phys. Rev. Lett.*, 76:831, 1996.

[16] G.W. Crabtree, G.K. Leaf, H.G. Kaper, V.M. Vinokur, A.E. Koshelev, D.W. Braun, D.M. Levine, W.K. Kwok, and J.A. Fendrich. Time-dependent Ginzburg-Landau simulations of vortex guidance by twin boundaries. *Physica C*, 263:401, 1996.

[17] G. W. Crabtree, D. O. Gunter, H. G. Kaper, A. E. Koshelev, G. K. Leaf , and V. M. Vinokur. Numerical simulations of driven vortex systems. Phys. Rev. B 61, 1446-1455, 2000.

[18] Th. Schuster, M.V. Indenbom, H. Kuhn, E.H. Brandt, and M.Konczykowski. *Phys. Rev. Lett.*, 73:1424, 1994.

[19] Th. Schuster, H. Kuhn, and E.H. Brandt. *Phys. Rev. B*, 51:697, 1995.

[20] M.R. Koblischka and R.J. Wijngaarden. *Supercond. Sci. Technol.*, 8:199, 1995.

[21] E.H. Brandt. *Phys. Rev. B*, 50:4034, 1994.

[22] C. Bean. Magnetization of high-field superconductors. *Rev. Mod. Phys.*, 36:31, 1962.

[23] E. H. Brandt. The Vortex Lattice in Superconductors. Zeitschrift fÄur Metallkunde 93, 1043-1051, 2002.

[24] V.K. Vlasko-Vlasov, M.V. Indenbom, V.I. Nikitenko, A.A. Polyanskii, R.L. Prozorov, I.V. Grekhov, L.A. Delimova, I.A. Liniichuk, A.V. Antonov, and M.Yu. Gusev. *Superconductivity*, 5:1582, 1992.

[25] F.F.Preparata and M.L.Shamos, Computational Geometry: An Introduction. Springer-Verlag, New York, 1985.

[26] C.P.Bean, J.D.Livingston. *Phys. Rev. Letters*, 12:14, 1964.

[27] T.Van Duzer, C.W.Turner. Principles of Superconductive Devices and Circuits. Elsevier, New York, 1981, p.319.

[28] V.K.Vlasko-Vlasov, V.I.Nikitenko, A.A.Polyanskii, G.W.Crabtree, U.Welp & B.W.Veal. *Physica C,* 222:361, 1994.

[29] S.Bhattacharya and M.J.Higgins. Phys. Rev. Lett., 70:2617, 1993.

[30] W.K.Kwok et al. Phys. Rev. Lett., 73:2614, 1994.

[31] W.R.White, A.Kapitulnik, and M.R.Beasley. Phys. Rev. B, 50:6303, 1994.

[32] S.N.Coppersmith. Phys. Rev. Lett., 65:1044, 1990.

[33] A.E.Koshelev and V.M.Vinokur. Phys. Rev. Lett., 73:3580, 1994.

[34] A.S.Mel'nikov, I. M. Nefedov, D. A. Ryzhov, I. A. Shereshevskii, V. M. Vinokur, and P.P.Vysheslavtsev. Phys. Rev. B 65, 1503, 2002.

[35] U.Essman and H.Trauble. Phys. Stat. Sol., 32, 337 (1969).

[36] A. T. Fiory, Phys. Rev. Lett., 27, 501 (1971).

[37] J. M. Harris, et al., Phys. Rev. Lett., 74, 3685 (1995).

[38] J.Guimpel, L.Civale, F. de la Cruz, J.M.Murduck, Ivan K. Schuller, Phys.Rev.B 38, 2342 (1988).

[39] Kai Liu, J. Nogues, C. Leighton, H. Masuda, K. Nishio, I. V. Roshchin, and Ivan K. Schuller. Fabrication and Thermal Stability of Arrays of Fe Nanodots. Applied Physics Letters 81, 4434-4436, 2002.

[40] G.Blatter, M.V.Feigel'man, V.B.Geshkenbein, A.I.Larkin, and V.M.Vinokur, Rev. Mod. Phys. 66, 1125 (1994).

[41] L.Ya. Vinnikov, L.A. Gurevich, G.A. Yemelchenko, and Yu.A. Ossipyan, Solid State Commun. 67, 421 (1988); G.J. Dolan, G.V. Chandrashekhar, T.R. Dinger, C. Feild, and F. Holtzberg, Phys. Rev. Lett. 62, 827 (1989).

[42] Igor Aranson, Alex Gurevich, and Valerii Vinokur. Phys. Rev. Lett. 87, 067003, 2001.

[43] E.M. Gyorgy, R.B. van Dover, L.F. Schneemeyer, A.E. White, H.M. O'Bryan, R.J. Felder, J.V. Waszczak, W.W. Rhodes, and F. Hellman, Appl. Phys. Lett. 56, 2465 (1990).

[44] L.J. Swartzendruber, D.L. Kaiser, F.W. Gayle, L.H. Bennett, and A. Roytburd, Appl. Phys. Lett. 58, 1566 (1991); D.L. Kaiser, F.W. Gayle, L.J. Swartzendruber, L.H. Bennett, and R.D. McMichael, J. Appl. Phys. 70, 5739 (1991).

[45] M. Oussena, P.A.J. de Groot, S.J. Porter, R. Gagnon, and L. Taillefer, Phys. Rev. B 51, 1389 (1995).

[46] B.M. Lairson, S.K. Streier, and J.C. Bravman, Phys. Rev. B 42, 10067 (1990).

[47] A.A. Zhukov, H. Kupfer, G. Perkins, L.F. Cohen, A.D. Caplin, S.A. Klestov, H. Claus, V.I. Voronkova, T. Wolf, and H. Wuhl, Phys. Rev. B 51, 12704 (1995); A.A. Zhukov, H. Kupfer, H. Claus, H. Wuhl, M. Klaser, and G. Muller-Vogt, Phys. Rev. B 52, R9871 (1995).

[48] H. Safar, S. Foltyn, H. Kung, M.P. Maley, J.O. Willis, P. Arendt, and X.D. Wu, Appl. Phys. Lett. 68, 1853 (1996).

[49] C.A. Duran, P.L. Gammel, R. Wolfe, V.J. Fratello, D.J. Bishop, J.P. Rice, and D.M. Ginsberg, Nature 357, 474 (1992).

[50] V.K. Vlasko-Vlasov, L.A. Dorosinskii, A.A. Polyanskii, V.I. Nikitenko, U. Welp, 13 B.W. Veal, and G.W. Crabtree, Phys. Rev. Lett. 72, 3246 (1994).

[51] C.A. Duran, P.L. Gammel, D.J. Bishop, J.P. Rice, D.M. Ginsberg, U. Welp, T. Gardiner, D.O. Gunter, B.W. Veal, G.W. Crabtree, V.K. Vlasko-Vlasov, and V.I. Nikitenko, Phys. Rev. Lett. 74, 3712 (1995).

[52] U. Welp, T. Gardiner, D.O. Gunter, B.W. Veal, G.W. Crabtree, V.K. Vlasko-Vlasov, and V.I. Nikitenko, Phys. Rev. Lett. 74, 3713 (1995).

[53] U. Welp, T. Gardiner, D. Gunter, J. Fendrich, G.W. Crabtree, V.K. Vlasko-Vlasov, and I. Nikitenko, Physica 235C, 241 (1994).

[54] R.J. Wijngaarden, R. Griessen, J. Fendrich and W.-K. Kwok, Phys. Rev. B 55, 3268 (1997).

[55] I.N. Khlyustikov and A.I. Buzdin, Adv. Phys. 36, 271 (1987).

[56] D.R. Nelson and V.M. Vinokur, Phys. Rev. B 48, 13060 (1993); M.C. Marchetti and V.M. Vinokur, Phys. Rev. Lett. 72, 3409 (1994).

[57] J. Groth, C. Reichhardt, C.J. Olson, S. Field, and F. Nori, Phys. Rev. Lett. 77, 3625 (1996).

[58] D.W. Braun, G.W. Crabtree, H.G. Kaper, A.E. Koshelev, G.K. Leaf, D.M. Levine, and V.M. Vinokur. Structure of a moving vortex lattice. Phys. Rev. Lett., 76:831–834, 1996.

[59] A. Schmid. A time dependent Ginzburg-Landau equation and its application to a problem of resistivity in the mixed state. Phys. kondens. Materie, 5:302, 1966.

[60] Harada et al., Science 274, 1167 (1996).

[61] W. Braun et al., Phys. Rev. Lett. 76, 831 (1996).

[62] O.M. Stoll, M.I. Montero, J. Guimpel, J.J. Akerman, I.K. Schuller. Hysteresis and Fractional Matching in Thin Nb Films with Rectangular Arrays of Nanoscaled Magnetic Dots. Phys. Rev. B 65, 104518, 2002.